Evaluation of Holes Fabricated Using Plasma Arc Cutting

PUBLICATION NO. FHWA-HRT-20-056

AUGUST 2020

U.S. Department of Transportation
Federal Highway Administration

Research, Development, and Technology
Turner-Fairbank Highway Research Center
6300 Georgetown Pike
McLean, VA 22101-2296

FOREWORD

This report documents fatigue and tensile test results of steel plates with round holes fabricated using plasma arc cutting. Bridge owners, designers, and fabricators have shown interest in using plasma arc cutting as a more economical alternative to traditional hole fabrication methods. However, a lack of experimental data demonstrating the behavior of plasma-cut holes under fatigue and tensile loading has hindered their use in steel bridge design and fabrication. FHWA initiated this study to categorize the fatigue and static tension resistance of plasma-cut holes in steel bridge members. This research establishes the design fatigue resistance and assesses the fracture behavior of steel members with plasma-cut holes. Multiple plasma-cutting processes were evaluated. Results showed that fatigue resistance of plasma-cut holes is lower compared to current hole-making methods. Tensile testing showed that certain plasma-cutting processes could cause brittle failure modes in tension members with plasma-cut holes.

This report will benefit those interested in the design and fabrication of round holes in steel bridge members, including State departments of transportation, bridge design consultants, bridge owners, steel bridge fabricators, and researchers.

Cheryl Allen Richter, Ph.D., P.E.
Director, Office of Infrastructure
Research and Development

TECHNICAL REPORT DOCUMENTATION PAGE

1. Report No. FHWA-HRT-20-056	2. Government Accession No.	3. Recipient's Catalog No.
4. Title and Subtitle Evaluation of Holes Fabricated Using Plasma Arc Cutting		5. Report Date August 2020
		6. Performing Organization Code:
7. Author(s) Christopher Beckett, Ph.D., P.E., and Justin Ocel, Ph.D., P.E. (ORCID 0000-0002-0176-7276)		8. Performing Organization Report No.
9. Performing Organization Name and Address Professional Service Industries, Inc. 13873 Park Center Road, Suite 315 Herndon, VA 20171		10. Work Unit No.
		11. Contract or Grant No. DTFH61-10-D-00017
12. Sponsoring Agency Name and Address Office of Infrastructure Research and Development Federal Highway Administration 6300 Georgetown Pike McLean, VA 22101		13. Type of Report and Period Covered Final Report; June 2012–October 2016
		14. Sponsoring Agency Code HRDI-40

15. Supplementary Notes
The work reported herein was conducted under Federal Highway Administration contract support services for the structures laboratories. Justin Ocel, Ph.D. (HRDI-40), provided technical oversight/assistance as the Task Manager and wrote portions of the report. Fassil Beshah, Ph.D. (HRDI-40), served as the Contracting Officer's Representative of this contract.

16. Abstract
Modern plasma-cutting equipment and techniques can produce high-quality holes more economically than drilling and punching. However, American Association of State Highway and Transportation Officials (AASHTO) design and construction specifications do not permit the use of plasma-cut holes in primary bridge members due to a lack of experimental data demonstrating their fatigue and tensile strength. Additionally, it is uncertain if holes fabricated using plasma arc cutting meet the AASHTO requirements for hole size accuracy. This research shows that round open holes fabricated using plasma arc cutting would be an AASHTO category E fatigue detail. Bearing connections with nonpretensioned bolts installed in plasma-cut holes would be classified as category E′. Both results represent lower fatigue resistance compared to drilled or punched holes. Most tension members produced a tensile strength equal to or exceeding the theoretical nominal tensile strength. However, several tension members did not attain the theoretical nominal strength and a reduction factor was necessary when calculating the tensile resistance of a member with plasma-cut holes. Tension testing at low temperatures revealed that members with conventional plasma-cut holes can fail with brittle fracture and insignificant inelastic deformation. Lastly, the four fabricators used for this study provided a mostly consistent hole diameter over numerous samples. However, variation in diameter was large enough that close quality control was required.

17. Key Words	18. Distribution Statement
Steel bridge, plasma arc cutting, bridge fabrication, hole-making, fatigue	No restrictions. This document is available through the National Technical Information Service, Springfield, VA 22161. http://www.ntis.gov

19. Security Classif. (of this report)	20. Security Classif. (of this page)	21. No. of Pages	22. Price
Unclassified	Unclassified	159	N/A

Form DOT F 1700.7 (8-72) Reproduction of completed page authorized.

SI* (MODERN METRIC) CONVERSION FACTORS

APPROXIMATE CONVERSIONS TO SI UNITS

Symbol	When You Know	Multiply By	To Find	Symbol
		LENGTH		
in	inches	25.4	millimeters	mm
ft	feet	0.305	meters	m
yd	yards	0.914	meters	m
mi	miles	1.61	kilometers	km
		AREA		
in^2	square inches	645.2	square millimeters	mm^2
ft^2	square feet	0.093	square meters	m^2
yd^2	square yard	0.836	square meters	m^2
ac	acres	0.405	hectares	ha
mi^2	square miles	2.59	square kilometers	km^2
		VOLUME		
fl oz	fluid ounces	29.57	milliliters	mL
gal	gallons	3.785	liters	L
ft^3	cubic feet	0.028	cubic meters	m^3
yd^3	cubic yards	0.765	cubic meters	m^3
		NOTE: volumes greater than 1,000 L shall be shown in m^3		
		MASS		
oz	ounces	28.35	grams	g
lb	pounds	0.454	kilograms	kg
T	short tons (2,000 lb)	0.907	megagrams (or "metric ton")	Mg (or "t")
		TEMPERATURE (exact degrees)		
°F	Fahrenheit	5 (F-32)/9 or (F-32)/1.8	Celsius	°C
		ILLUMINATION		
fc	foot-candles	10.76	lux	lx
fl	foot-Lamberts	3.426	$candela/m^2$	cd/m^2
		FORCE and PRESSURE or STRESS		
lbf	poundforce	4.45	newtons	N
lbf/in^2	poundforce per square inch	6.89	kilopascals	kPa

APPROXIMATE CONVERSIONS FROM SI UNITS

Symbol	When You Know	Multiply By	To Find	Symbol
		LENGTH		
mm	millimeters	0.039	inches	in
m	meters	3.28	feet	ft
m	meters	1.09	yards	yd
km	kilometers	0.621	miles	mi
		AREA		
mm^2	square millimeters	0.0016	square inches	in^2
m^2	square meters	10.764	square feet	ft^2
m^2	square meters	1.195	square yards	yd^2
ha	hectares	2.47	acres	ac
km^2	square kilometers	0.386	square miles	mi^2
		VOLUME		
mL	milliliters	0.034	fluid ounces	fl oz
L	liters	0.264	gallons	gal
m^3	cubic meters	35.314	cubic feet	ft^3
m^3	cubic meters	1.307	cubic yards	yd^3
		MASS		
g	grams	0.035	ounces	oz
kg	kilograms	2.202	pounds	lb
Mg (or "t")	megagrams (or "metric ton")	1.103	short tons (2,000 lb)	T
		TEMPERATURE (exact degrees)		
°C	Celsius	1.8C+32	Fahrenheit	°F
		ILLUMINATION		
lx	lux	0.0929	foot-candles	fc
cd/m^2	candela/m2	0.2919	foot-Lamberts	fl
		FORCE and PRESSURE or STRESS		
N	newtons	2.225	poundforce	lbf
kPa	kilopascals	0.145	poundforce per square inch	lbf/in^2

*SI is the symbol for International System of Units. Appropriate rounding should be made to comply with Section 4 of ASTM E380. (Revised March 2003)

TABLE OF CONTENTS

LIST OF FIGURES

LIST OF TABLES

LIST OF ABBREVIATIONS AND SYMBOLS

Abbreviations

AASHTO	American Association of State Highway and Transportation Officials
BCS	*Bridge Construction Specifications*
BDS	*Bridge Design Specifications*
CAFT	constant amplitude fatigue threshold
CNC	computer numerical control
COV	coefficient of variation
CVN	Charpy V-notch
HAZ	heat-affected zone
HD	high definition
HV	Vickers hardness
ID	identification
LRFD	*Load and Resistance Factor Design*
LVDT	linear variable differential transducer
O_2	oxygen
S-N	stress–life

Symbols

α	conical taper angle
C_h	hole circularity
D	hole diameter
$D_{circumscribed}$	Diameter of circumscribed circle for circularity calculation
$D_{inscribed}$	Diameter of inscribed circle for circularity calculation
D_{max}	maximum best-fit diameter of hole in conical taper calculation
D_{min}	minimum best-fit diameter of hole in conical taper calculation
e_h	hole eccentricity
F_{gross}	gross area stress at fracture of plasma-cut specimen
F_{net}	net area stress at fracture of plasma-cut specimen
F_u	measured tensile strength of material coupon
F_y	measured yield strength of material coupon
t_p	plate thickness
L	major axis length of best-fit ellipse in hole eccentricity calculation
R	load ratio
W	minor axis length of best-fit ellipse in hole eccentricity calculation

INTRODUCTION

The fabrication of holes in steel bridge members is governed by the American Association of State Highway and Transportation Officials (AASHTO) *Load and Resistance Factor Design* (LRFD) *Bridge Construction Specifications* (BCS).[1] The AASHTO LRFD BCS specifies that all holes in primary bridge members shall be punched, drilled, or subpunched and reamed. The AASHTO LRFD BCS allows the use of thermally (i.e., plasma, laser, or oxygen-acetylene) cut round and slotted holes in thin, secondary bridge members. One of these thermal-cutting methods, plasma arc cutting, is a potential alternative to traditional hole-making methods for primary bridge members. However, bridge owners, engineers, and steel fabricators are hesitant to use plasma-cut holes because of uncertainty regarding their structural performance.

While not a novel technology, plasma arc cutting has been used in various industries since the 1960s. However, its use for steel bridge fabrication is limited primarily to cutting straight edges. With extensive incorporation of computer numerical control (CNC), advanced motion-control equipment, and optimized cutting parameters (e.g., amperage and cutting speed), conventional plasma arc cutting evolved into high-definition (HD) plasma arc cutting. Over the past decade, increasing numbers of steel fabricators are investing in plasma-cutting systems that produce high-quality round holes.

Several proprietary HD plasma-cutting systems that produce holes of comparable quality to those created by drilling and punching are commercially available. Many steel fabrication shops have cutting tables allowing them to perform multiple fabrication procedures, such as edge cutting and hole-making, within a single process step. This leads to fewer material-handling maneuvers, ultimately reducing fabrication time and potentially making plasma arc cutting a more economical choice compared to drilling and punching operations. Despite the increased productivity offered by newer plasma-cutting technologies, their application for hole-making will remain limited until the fatigue and tensile strengths of plasma-cut holes are known.

The fatigue strength of steel bridge members is governed by the AASHTO LRFD *Bridge Design Specifications* (BDS).[2] All open holes are classified as a category D fatigue detail. The fatigue resistance of holes in pretensioned joints depends on the fabrication method used to produce the holes. Holes in a pretensioned joint that are drilled, subpunched, and then reamed are classified as a category B fatigue detail, while holes punched full-size are classified a category D fatigue detail. The fatigue resistance for each of these conditions is based on the gross area of the bridge member. Holes in nonpretensioned joints are classified as a category D fatigue detail based on the nominal stress over a net section area. There is a lack of experimental data showing whether the fatigue resistance of plasma-cut holes meets these requirements.

There is also a lack of experimental data showing the tensile and fracture behavior of bridge members with plasma-cut holes. The AASHTO LRFD BCS prohibits thermally cut holes in all primary bridge members. A similar exclusion applies to holes punched full-size in fracture-critical bridge members, a stipulation meant to avoid fabrication practices that make a structural bridge member brittle and susceptible to fracture.[3] The same concept may be extended to include plasma-cut holes, which typically present notable surface flaws and

increased hardness within a heat-affected zone (HAZ) that results from the plasma-cutting process.

The AASHTO LRFD BCS places strict fabrication tolerances on round holes in steel bridge members. The diameter (D) of a hole shall be no greater than $^1/_{32}$ inch larger than the specified nominal D. The maximum surface roughness is limited to 1,000 microinches, and any conical taper that extends through the depth of a hole must be within tolerance.[1] The ability of modern plasma-cutting systems to meet these standards for a specified hole D is yet to be investigated.

PLASMA ARC CUTTING BACKGROUND

Plasma arc cutting is a thermal-cutting method, similar to oxygen-acetylene and laser cutting, where heat is used as a cutting tool. The plasma-cutting process works by passing an electrical arc through a highly pressurized gas, or gaseous mixture, to form a high-temperature plasma jet. Portable (i.e., handheld) and machine-mounted plasma-cutting systems are used to cut a variety of metals, including aluminum, stainless steel, and mild steel.

The main components of a plasma-cutting system include a power supply, arc-starting console, gas-supply console, and a plasma torch. The arc-starting console and the power supply are responsible for initiating and maintaining the plasma arc during the cutting process. Most plasma-cutting systems utilize a dual-gas setup where the primary cutting gas (i.e., plasma gas) is protected using a shielding gas. The composition of these gases depends on the type of metal being cut. For structural steels, oxygen (O_2) is preferred because it produces a more desirable cut quality and faster cutting speed compared to other gases.[4]

The plasma torch directs the plasma gas and houses the consumables, which include a shield, retaining cap, nozzle, swirl ring, and electrode. The consumables quickly degrade and deteriorate, requiring frequent replacement. Consequently, the torch is a key factor defining the cut quality of a plasma-cutting system. Features typically used to describe the quality of a plasma-cut hole include the conical taper angle (α), HAZ thickness, presence of dross (i.e., resolidified material), surface roughness, and presence of flaws or defects on the cut surface.

Conventional Plasma Arc Cutting

Conventional plasma-cutting systems are highly mechanized and typically deployed in a gantry-type setup, taking advantage of large cutting tables. Computer-aided design software and CNC technology are integral to modern cutting processes. However, despite a high level of automation, a significant amount of responsibility falls on the operator to ensure all cutting parameters (e.g., the cutting speed, arc voltage, and gas flow) are set and maintained correctly throughout the entire cutting process to ensure the highest quality cut.[5]

While already widely used for cutting straight edges, conventional plasma arc cutting is not well suited for hole-making. Surface flaws, out-of-roundness (i.e., noncircular holes), dross, and conical taper are common in holes fabricated using conventional plasma-cutting systems.[6] Figure 1 shows a hole with a rough surface finish. Figure 2 shows a hole with a much smoother surface finish and an arc-termination notch. These types of surface imperfections were regularly observed on holes fabricated using conventional plasma-cutting systems in this study.

Imperfections on the cut edge act as stress concentrations and can potentially reduce the fatigue and tensile strength of a structural bridge member. Repairing these features requires additional fabrication steps, such as reaming and mechanical grinding, which diminish the key economic benefit (i.e., time savings) of plasma arc cutting versus other hole-fabrication methods.

Source: FHWA.

Figure 1. Photo. Rough surface finish in a hole.

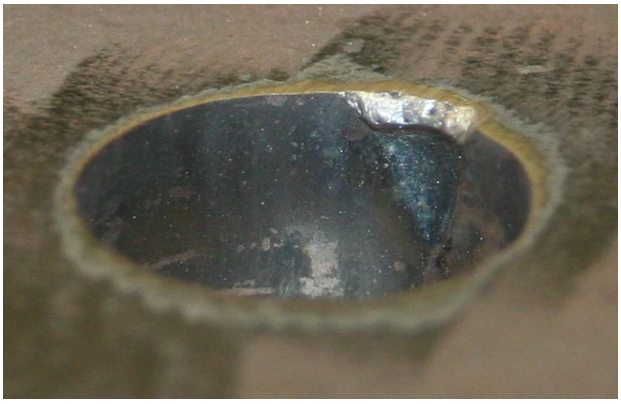

Source: FHWA.

Figure 2. Photo. Smooth surface finish with an arc-termination notch.

HD Plasma Arc Cutting

Compared to conventional plasma arc cutting, HD plasma arc cutting produces high-quality round holes without the need for secondary fabrication procedures. The notable increase in cut quality is achieved primarily through improvements within the plasma torch. The torches used in HD plasma-cutting systems constrict the plasma arc, increasing plasma density and making the arc more stable and uniform. Advanced motion-control equipment and CNC technology are also important components of HD plasma-cutting systems. Improved cut quality is noted by a squarer cut edge, narrower kerf, and reduced dross.[4] With HD plasma-cutting systems, the width of the HAZ is thinner as well—another indicator of cut quality.[7] Similar material thicknesses can be cut at a lower power output with HD plasma-cutting systems compared to conventional plasma arc cutting. At higher power outputs, HD plasma-cutting systems can produce high-quality cuts in workpieces up to 3 inches thick.[6]

Even with HD plasma-cutting systems, some responsibility is still given to the operator to maintain certain parameters during the cutting process. While reduced in severity, the same issues seen in holes fabricated using conventional plasma arc cutting (e.g., surface flaws, out-of-roundness) are present in holes fabricated with HD plasma arc cutting.[5,6]

Enhanced HD Plasma Arc Cutting

Enhancements to HD plasma arc cutting have been introduced over the last few years, predominantly for hole-making applications. These systems, described herein as enhanced HD plasma arc cutting, represent the state-of-the-art in HD plasma-cutting technology and are fully automated, integrating CNC technology throughout the entire cutting process. Cutting parameters are adjusted by a computer in real-time, accounting for all factors that affect cut

quality, completely eliminating the need for operator intervention.[5,6] Nesting software is typically incorporated as well, helping increase efficiency during cutting cycles. The increased automation results in higher productivity and more consistent hole quality.

Several proprietary systems utilizing enhanced HD plasma-cutting technology are commercially available. However, the cost of ownership (e.g., initial investment and consumables) of these enhanced HD plasma-cutting systems can reduce their appeal to steel bridge fabricators, especially since plasma-cut holes are rarely used in steel bridge structures. Bridge owners are expected to avoid approving fabricating holes with plasma arc cutting in lieu of drilling and punching until the fatigue and tensile performance data justify the increased use of this technology.

OBJECTIVE

The objective of this study was to determine the fatigue and tensile resistance of holes fabricated with plasma-cutting technologies. Test results were used to provide AASHTO LRFD BCS and BDS recommendations allowing plasma-cut holes in a wider range of bridge members.[1,2]

METHODOLOGY

Specimens tested included both plates with a single hole and plates with a two-by-two matrix of holes to mimic the testing matrix of Brown for punched holes.[8] The four-hole specimens were tested as bearing-type bolted butt joints. The specimens were sourced from four independent fabricators and contained holes fabricated with a blend of conventional and enhanced plasma-cutting technologies. Conventional plasma arc cutting is recognized as providing lesser-quality holes; however, it is more readily available in most fabrication shops and was tested to establish a performance baseline. One of the two fabricators using conventional plasma was a prominent steel bridge fabricator, while the other was a general steel fabricator servicing numerous industries. One of the two fabricators using enhanced HD plasma owned a commercially available plasma-cutting system to manufacture equipment for use in the mining and quarrying industries, while the other specialized in designing and manufacturing plasma-cutting equipment and conducted its own research to improve plasma-cutting technology. This fabricator developed proprietary plasma-cutting technology specifically designed for hole-making in steel plates.

All four fabricators were tasked with fabricating plasma-cut holes using their current plasma-cutting systems and operating procedures; no particular instructions regarding the cutting process were specified. This ensured the quality of the holes produced for this study were characteristic of each fabricator's typical plasma-cutting capability. Each fabricator was responsible for material procurement depending on the steel grades they were assigned to provide. All steel was furnished to ASTM A709 requirements in ½-inch gauge.[9] Three grades of steel, 36, 50, and 50W, were considered.

Throughout this report, the individual fabricators are referenced by the cutting process they employ—"C" for conventional and "E" for enhanced—and a sequential numerical identifier. A specimen series is defined with an alphanumeric code consisting of the fabricator identification (ID) and the grade of steel. For example, the specimen series "C2-36" refers to grade 36 plate

specimens produced by fabricator C2. Details of the plasma-cutting process used by each fabricator are provided in table 1.

Table 1. Fabricator details.

Fabricator ID	Plasma-Cutting Technology	Plasma Gas	Shielding Gas	Power Output (Amps)	Steel Grades Provided
C1	Conventional	O_2	Air	200	50, 50W[b]
C2	Conventional	O_2	O_2	[a]	36, 50W[b]
E3	Enhanced HD	O_2	Air	150	50W[b]
E4	Enhanced HD	O_2	O_2	130	50W[b]

[a]Power output used by fabricator C2 is unknown.
[b]Furnished to type B chemistry in ASTM A709.[9]
ID = Identification.

EVALUATION OF HOLE QUALITY

Quality and repeatability are two important considerations for plasma-cut holes. This chapter discusses the visual aspects of holes from each of the four fabricators along with the hole accuracy assessed by laser scanning. The measured width and hardness of the HAZ are also discussed.

HOLE AESTHETICS

The aesthetics and surface condition of the plasma-cut holes varied noticeably between the test series. Figure 3 through figure 7 show the top view of a randomly selected hole from each of the test series. The camera was aligned perpendicular to the specimen surface; therefore, if the inside of the hole can be seen, the hole is either not perpendicular to the surface or has a conical taper that extends through the thickness of the plate. Visually, it is evident that none of the five example holes are perfectly round.

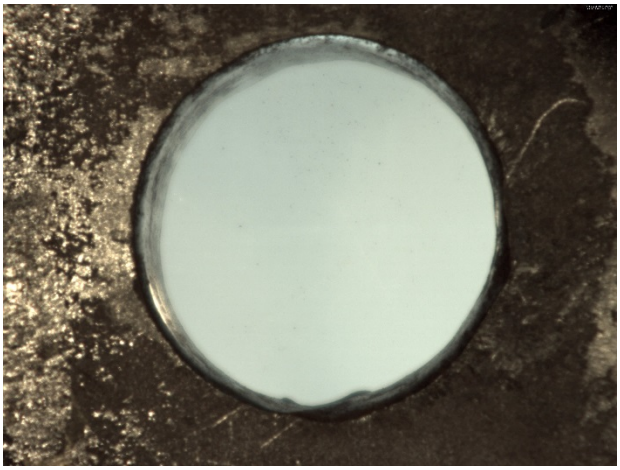

Source: FHWA.

Figure 3. Photo. Roundness of series C1-50.

Source: FHWA.

Figure 4. Photo. Roundness of series C1-50W.

Source: FHWA.

Figure 5. Photo. Roundness of series C2-36.

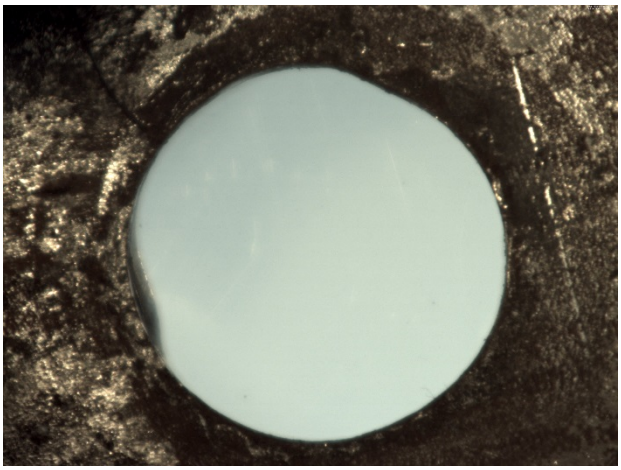

Source: FHWA.

Figure 6. Photo. Roundness of series E3-50W.

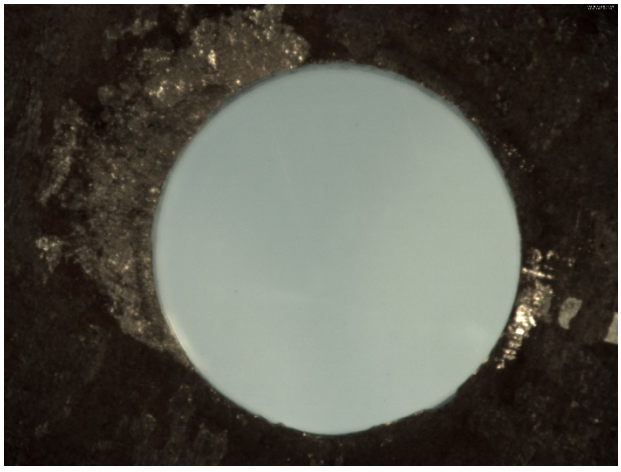

Source: FHWA.

Figure 7. Photo. Roundness of series E4-50W.

A common concern plaguing all plasma-cut holes fabricated for this study was the presence of a surface imperfection on the cut face at the plasma arc termination point. This flaw is a widely reported artifact of the plasma-cutting process, specifically when used to fabricate round holes. Figure 8 through figure 12 show how this surface defect typically looked on the five random holes selected. Holes cut by fabricator C1 showed a deep, distinct surface imperfection. The hole cut by fabricator C2 shows the surface condition is poor over a wide area. The enhanced HD cutting processes used by fabricators E3 and E4 noticeably reduced the size and depth of the flaw.

Source: FHWA.

Figure 8. Photo. Surface finish of series C1-50.

Source: FHWA.

Figure 9. Photo. Surface finish of series C1-50W.

Source: FHWA.

Figure 10. Photo. Surface finish of series C2-36.

Source: FHWA.

Figure 11. Photo. Surface finish of series E3-50W.

Source: FHWA.

Figure 12. Photo. Surface finish of series E4-50W.

DIMENSIONAL MEASUREMENT SETUP AND PROCEDURE

To provide a quantitative assessment of hole quality, a high-accuracy laser-tracking system, displayed in figure 13, was used to measure geometric features of the holes. These features included D, eccentricity (e_h), circularity (C_h), and α, which collectively describe the accuracy and overall roundness of the cut delivered by each fabricator. The laser-tracking system operated by directing a laser beam from the scanner head toward a target prism, which reflected the beam back to its source. Point coordinates in an established coordinate system were generated based on the relative distance between the target prism and the scanner head. A proprietary software package stored the point coordinates and calculated the necessary values needed to quantify the geometric features.

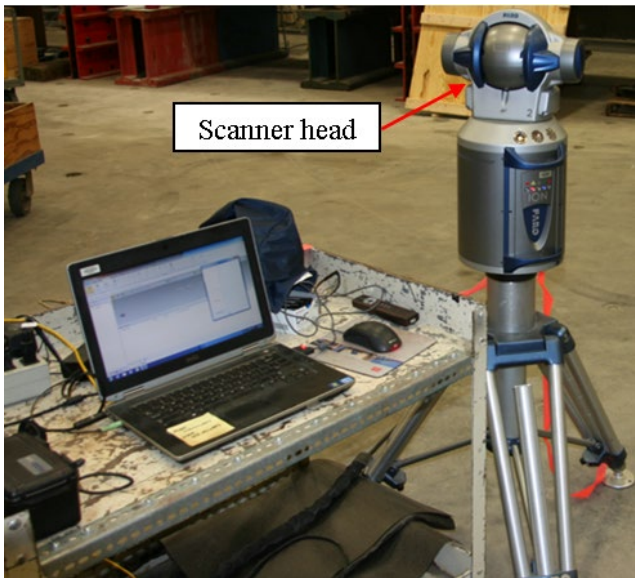

Source: FHWA.

Figure 13. Photo. Laser-tracking system.

To accurately record point coordinates on the perimeter of the hole or the hole edge, a specially designed pin nest was machined and secured to the target prism, as shown in figure 14. The small, 0.125-inch-long pin seen in figure 14 was pressed firmly against the cut face as the target prism was manually guided around the hole. Point coordinates were recorded at 0.005-inch increments, generating several hundred data points around the perimeter of each hole.

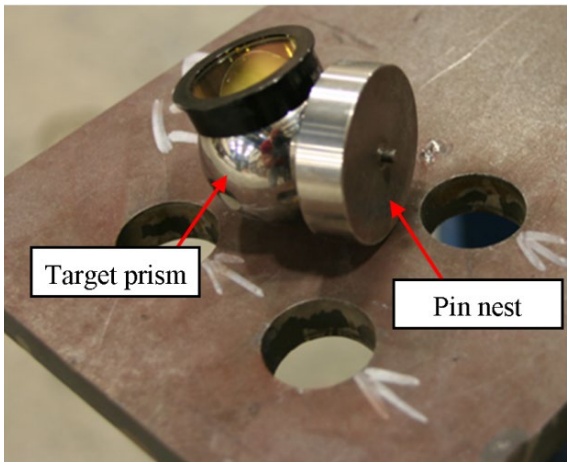

Source: FHWA.

Figure 14. Photo. Target prism and pin nest.

Hole-edge measurements were recorded on each face of the plate to capture any change in hole geometry through the thickness of the plate. The surface flaw and roughened areas proximate to the cut-termination point were avoided, as they overly biased the measurements. Measurements were collected from 200 plasma-cut holes (40 measurements from 5 different specimen series). For comparison, measurements were also collected from 10 drilled holes. Drilled holes were fabricated by the research team using an annular cutter and magnetic drill on extra plates provided by each fabricator.

GEOMETRIC FEATURES

The point-coordinate data collected from each face of the plate of every measured hole were analyzed within the proprietary software, which reported the four metrics used to quantify hole quality. The following subsections describe the four metrics of D, e_h, C_h, and α along with a summary of the data. All plasma-cut holes were specified to have a nominal D of $^{15}/_{16}$ inch, and all plates were nominally ½-inch thick. The drilled holes were made using a bit with a nominal diameter of $^{13}/_{16}$ inch. This smaller diameter was used due to the ready availability of the drill bit in lieu of a $^{15}/_{16}$-inch-diameter drill bit matching the specified plasma-cut hole D.

Comparisons were made between the plasma-cut and drilled holes. Data for each measured hole and metric are provided in appendix A.

Diameter

Hole diameters, D, were determined by the proprietary software using a circle fitted by least square regression through the point-coordinate data. An example of typical point-coordinate data

(round data points) and the best-fit circle (solid line) are illustrated in figure 15. Table 2 summarizes the average and coefficient of variation (COV) for all *D* measurements for each specimen series.

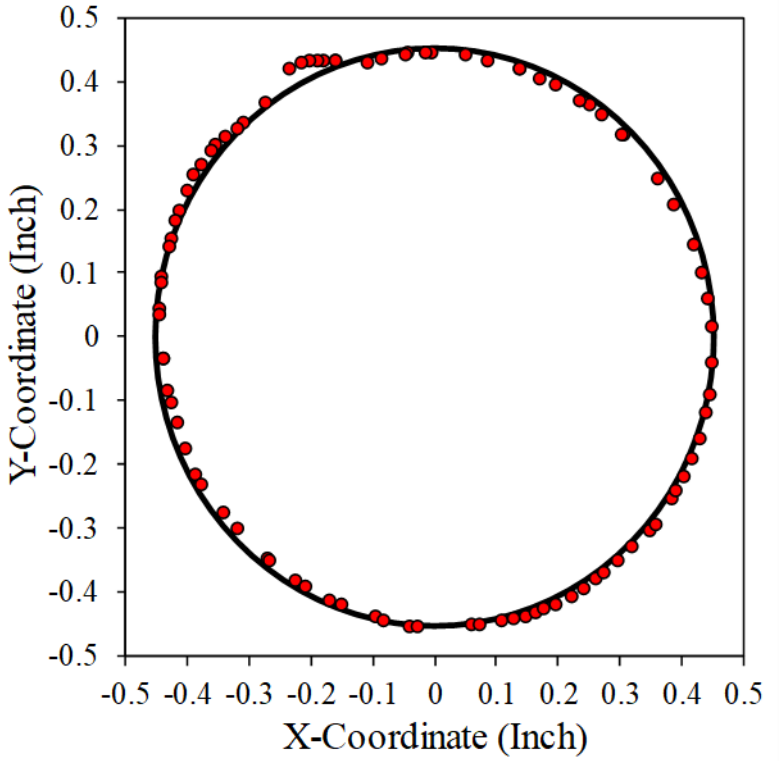

Source: FHWA.

Figure 15. Graph. Best-fit circle representing hole *D*.

Table 2. Best-fit *D* measurements.

Specimen Series	Side 1 Average (Inch)	Plane 1 COV	Side 2 Average (Inch)	Plane 2 COV
C1-50	0.994[a]	0.055	0.956[a]	0.060
C1-50W	0.938[a]	0.004	0.897[a]	0.007
C2-36	0.978[a]	0.008	0.945[a]	0.019
E3-50W	0.977[a]	0.006	0.949[a]	0.005
E4-50W	0.959[a]	0.004	0.958[a]	0.006
Drilled	0.823[b]	0.001	0.834[b]	0.003

[a]Expected value of 0.938 inches.
[b]Expected value of 0.813 inches.

A plus $^{1}/_{32}$-inch tolerance on hole *D* is specified in the AASHTO LRFD BCS.[(1)] Therefore, to meet AASHTO requirements, the plasma-cut hole *D* could vary between $^{15}/_{16}$ inch and $^{31}/_{32}$ inch and be considered acceptable. The acceptability of the holes is better visualized with the

cumulative distributions shown in figure 16 and figure 17, respectively, for the plasma-cut and drilled holes. Each plot shows two vertical dashed lines representing the range of allowable values ($^{15}/_{16}$ to $^{31}/_{32}$ inch for a nominal $^{15}/_{16}$-inch plasma-cut hole and $^{13}/_{16}$ to $^{27}/_{32}$ inch for a nominal $^{13}/_{16}$-inch drilled hole). Specifically, in figure 16, series C1-50, C1-50W, and C2-36 holes had a significant population of holes with *D* outside the acceptable range. Approximately only 25 percent of the hole populations from each of these hole series were within the acceptable range, indicating that conventional plasma will not reliability meet hole *D* requirements. The two enhanced plasma series were better, but not perfect. Nearly all of series E4-50W holes were within the acceptable tolerance range, though only 50 percent of series E3-50W were within the acceptable tolerance range. However, if the acceptable tolerance were increased to plus $^{1}/_{16}$ inch, as is commonly assumed for punched holes, then all of series E3-50W and E4-50W would be acceptable. The cumulative distribution in figure 17 for the drilled holes shows all holes were within the acceptable tolerance range.

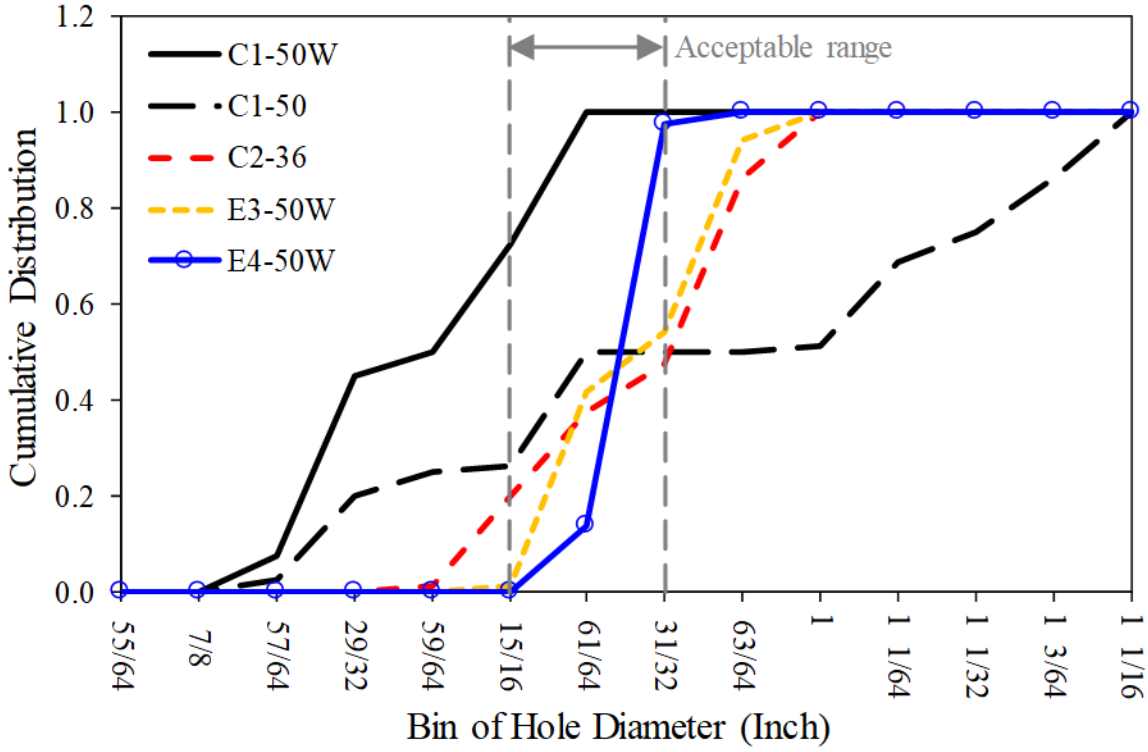

Source: FHWA.

Figure 16. Graph. Cumulative distribution of plasma-cut hole *D*.

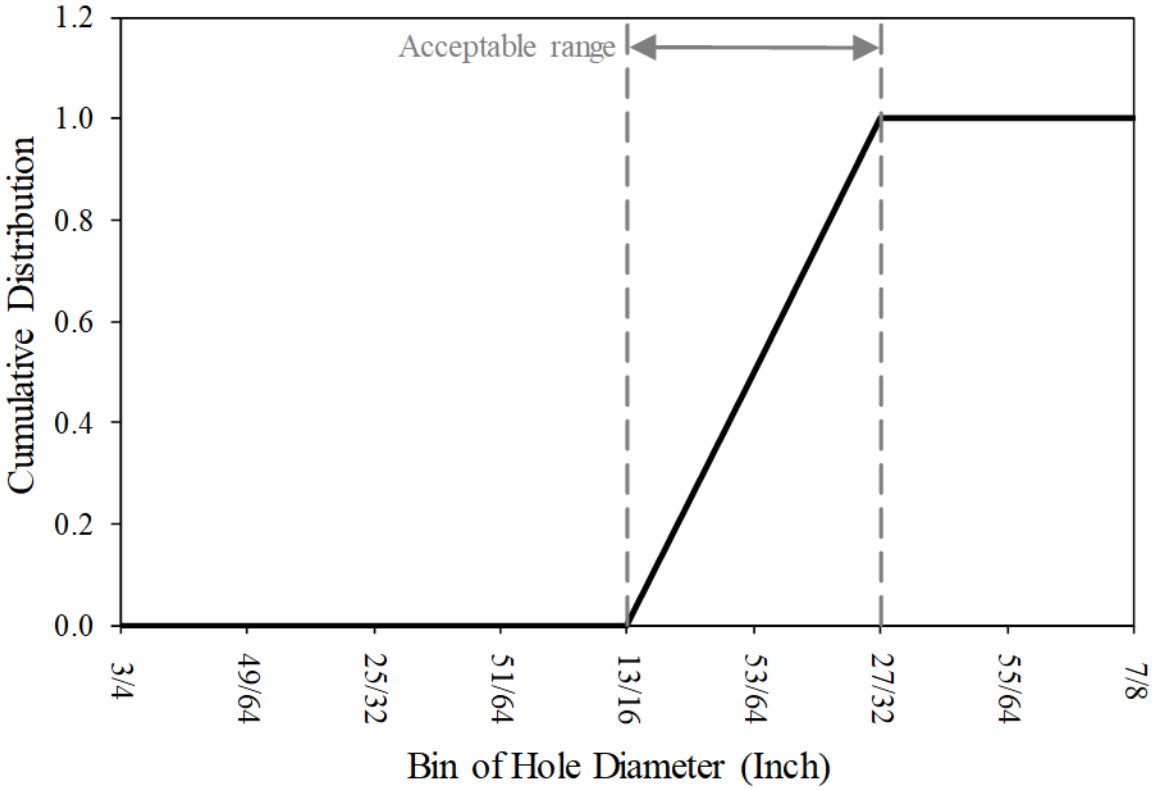

Source: FHWA.

Figure 17. Graph. Cumulative distribution of drilled hole *D*.

Eccentricity

Hole eccentricity, e_h, was calculated considering a best-fit ellipse to the point-coordinate data. This is illustrated in figure 18 for the same point-cloud data in figure 15. The best-fit algorithm allowed the major and minor axes of the ellipse to be rotated with respect to the data-coordinate system (i.e., the graph axes). The major axis length (L) and minor axis length (W) were used to calculate e_h using the equation shown in figure 19. For a perfectly round hole, e_h should be 0. Table 3 summarizes average e_h determined from the measurements on each face of the specimen and for each specimen series. As is evident from table 3, even a drilled hole had a small amount of e_h. However, the e_h of the enhanced HD plasma holes was generally twice that of a drilled hole; for the conventional plasma holes, it was four to six times larger.

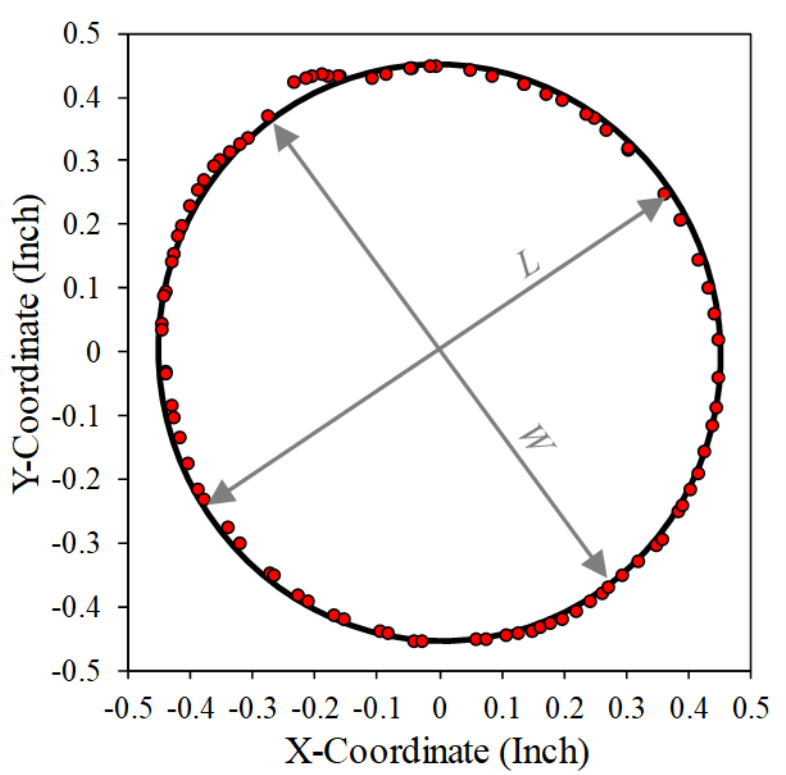

Source: FHWA.

Figure 18. Graph. Best-fit ellipse representing e_h.

$$e_h = \sqrt{1 - \frac{W^2}{L^2}}$$

Figure 19. Equation. e_h.

Table 3. Average e_h measurements.

Specimen Series	Face 1 Average (Inch)[a]	Side 1 COV	Face 2 Average (Inch)[a]	Side 2 COV
C1-50	0.261	0.082	0.358	0.050
C1-50W	0.266	0.128	0.285	0.143
C2-36	0.181	0.258	0.361	0.132
E3-50W	0.100	0.277	0.158	0.258
E4-50W	0.133	0.270	0.162	0.193
Drilled	0.073	0.347	0.064	0.400

[a]Ideal e_h for a round hole is 0.

Circularity

Hole circularity, C_h, is defined by inscribing and circumscribing two circles to either neglect or capture all the point data. Figure 20 shows this with the same point-coordinate data shown in figure 15 and figure 18 where two solid-lined circles illustrate the inscribed and circumscribed circles. C_h is calculated as the difference between the diameters of the circumscribed ($D_{circumscribed}$) and inscribed ($D_{inscribed}$) circles, as shown in the equation of figure 21. The more round the hole is, the more the inscribed and circumscribed D converge toward each other; ideally, C_h becomes 0. Results for C_h are reported in table 4 for each face of the specimens and for each specimen series. Even a drilled hole had a small C_h, as seen in table 4. However, C_h values for the enhanced HD plasma-cut holes were about 2 to 4 times larger than that of a drilled hole; for conventional plasma, C_h values were between 4 and 12 times larger.

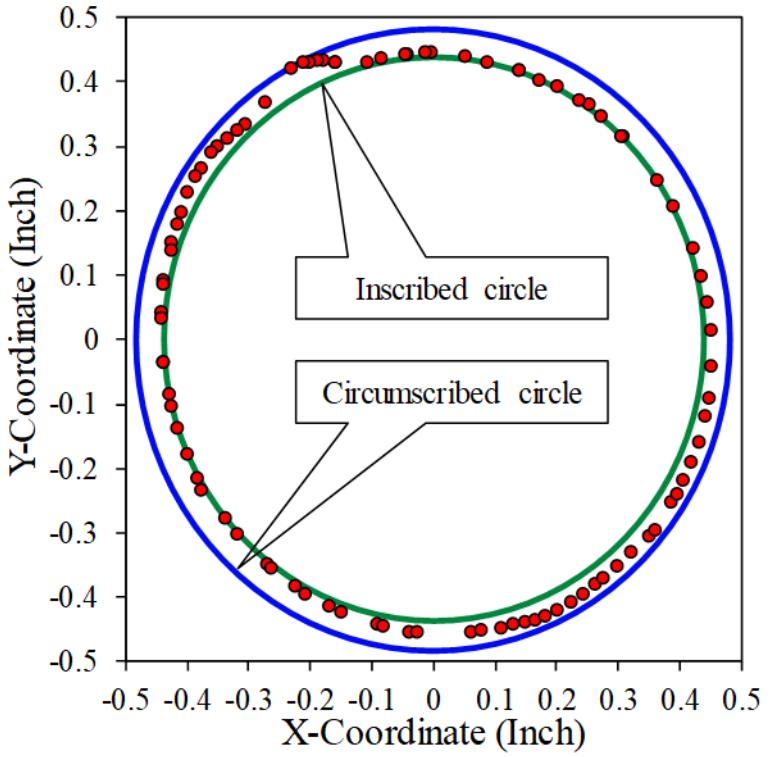

Source: FHWA.

Figure 20. Graph. C_h diagram.

$$C_h = D_{circumscribed} - D_{inscribed}$$

Figure 21. Equation. C_h.

Table 4. C_h measurements.

Specimen Series	Face 1 Average (Inch)[a]	Side 1 COV	Face 2 Average (Inch)[a]	Side 2 COV
C1-50	0.023	0.182	0.042	0.133
C1-50W	0.022	0.247	0.037	0.201
C2-36	0.024	0.197	0.060	0.233
E3-50W	0.012	0.320	0.020	0.333
E4-50W	0.017	0.245	0.021	0.228
Drilled	0.005	0.490	0.005	0.532

[a]Ideal C_h for a round hole is 0.

Conical Taper Angle

Conical taper angle, α, the plane-to-plane variation in D, was visually perceptible in many conventional plasma-cut holes. Illustrated in figure 22, conical taper was calculated using the equation in figure 23, where D_{max} and D_{min} are the maximum and minimum best-fit D on each side of the specimen, respectively, and t_p is the nominal plate thickness, equal to ½ inch. The estimated α is summarized in table 5. Lower α values are desirable; ideally, they would be 0. Although mentioned in terms of punched holes, the AASHTO LRFD BCS states that a slight α in holes is acceptable but does not provide a specific tolerance.(1) Since punching is referenced, table 5 also shows the measured α in punched hole slugs reported by Brown.(8) The data in the table 5 show all the plasma-cut holes have statistics commensurate with punching, though the lower values with the enhanced HD plasma-cutting processes are preferable.

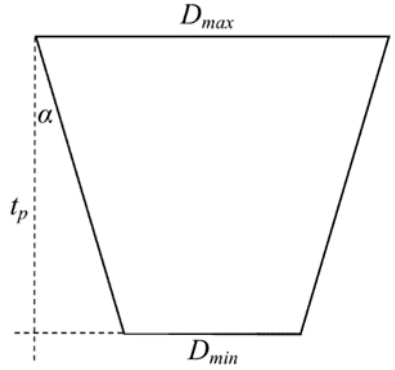

Source: FHWA.

Figure 22. Illustration. α diagram.

$$\alpha = tan^{-1}\left(\frac{D_{max} - D_{min}}{2t_p}\right)$$

Source: FHWA.

Figure 23. Equation. α.

Table 5. α measurement results.

Specimen Series	Average (Degree)[a]	COV
C1-50	2.18	0.193
C1-50W	2.36	0.132
C2-36	1.87	0.520
E3-50W	1.57	0.254
E4-50W	0.33	0.926
Drilled	0.62	0.231
Punched[b]	2.27	0.795

[a]Ideal α is 0 degrees.
[b]Measurements of slugs reported by Brown were used to calculate α.[(8)]

HAZ AND HARDNESS

Width of the HAZ was an additional measurement used to evaluate plasma-cut hole quality. As with all thermal-cutting techniques, a HAZ develops on the cut edge during plasma arc cutting. Within the HAZ, the microstructure of the material is altered, typically resulting in higher hardness relative to the base material. The increased material hardness can be associated with lower impact energy and an increased risk of brittle behavior. Microcracking and residual stresses, while not investigated during this study, typically develop as well.[(4)]

Minimizing the width of the HAZ limits potential risks associated with microcracking and brittle behavior as mentioned above. The extent of the HAZ that forms during the plasma-cutting process is dependent on the amount of heat a cut edge is exposed to. This exposure can be limited by reducing energy density of the plasma arc (i.e., system current) and/or by increasing cutting speeds. Prior work has demonstrated that cutting current is the most influential parameter affecting the width and characteristics of the HAZ; cutting speed is also influential.[(10,11)]

To investigate the HAZ on plasma-cut holes, a circular core shown in figure 24 was extracted around one hole produced for each series since each used a particular combination of cutting current and speed. Each sample was macroetched according to ASTM E340 using a 2-percent nital solution and examined under a microscope at ×10 magnification.[(12)] The width of the HAZ was measured at four equally spaced locations around the hole perimeter using image-analysis software, as depicted in figure 24. Note that location 1 coincided with the arc-termination notch. The HAZ was assumed to terminate where the microstructure of the base material appeared unchanged, as seen in figure 25.

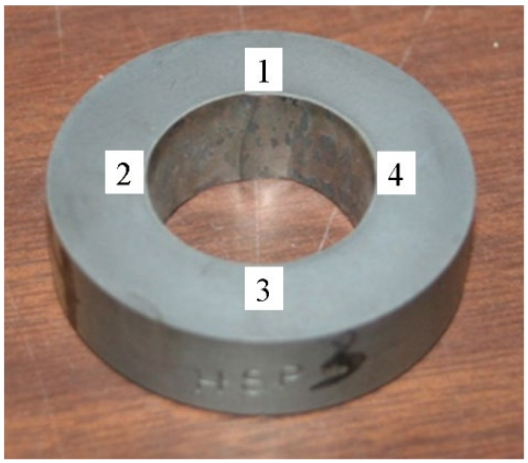

Source: FHWA.

Figure 24. Photo. Sample used for HAZ characterization.

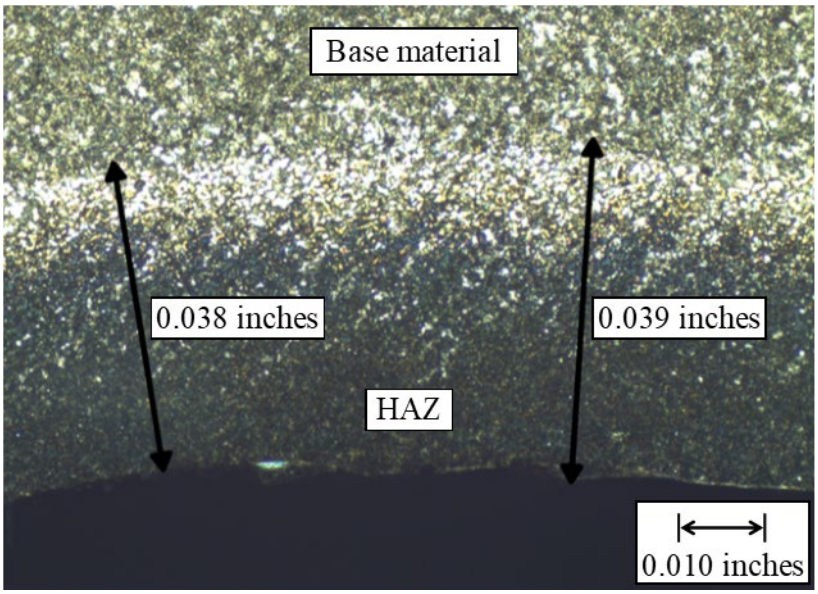

Source: FHWA.
Note: Distances are illustrative and not meant to match any values in table 6.

Figure 25. Photo. HAZ of a series C1-50W hole as seen under a microscope at ×10 magnification.

Table 6 summarizes the HAZ width measurements. The plasma-cut hole in series C1-50 displayed the smallest average HAZ thickness at 0.012 inches. The plasma-cut hole in series C2-50W steel showed the largest average HAZ thickness at 0.034 inches. Maximum HAZ thickness coincided with the location of the arc-termination notch only on series C1-50 and C1-50W.

Table 6. HAZ width.

Specimen Series	Location 1[a,b]	Location 2[b]	Location 3[b]	Location 4[b]	Average
C1-50	0.015	0.011	0.011	0.010	0.012
C1-50W	0.038	0.028	0.026	0.024	0.029
C2-36	0.019	0.036	0.028	0.025	0.027
C2-50W	0.033	0.034	0.037	0.030	0.034
E3-50W	0.020	0.029	0.030	0.030	0.027
E4-50W	0.033	0.041	0.026	0.026	0.032

[a]Coincides with arc-termination notch.
[b]See figure 24 for reference to locations 1 through 4 around the hole perimeter.

Material hardness was characterized using the Vickers hardness (HV) scale, following ASTM E384.[(13)] Microindentations were applied at the four specified locations around the perimeter of the hole. The measurement locations are identified in table 7 with reference to the cut edge, where the edge distances are tentatively in the radial direction of the core. The first indentation was placed within the HAZ. Additional indentations were placed within the base material. The location of the first two indentations made in a typical sample is illustrated in figure 26. Table 7 provides the data for all 72 hardness measurements collected. The increased hardness in the HAZ relative to the base material is clear. However, hardness trends are not further discussed because the total hardness was a function of the heat input by each fabricator and the hardenability of each steel used, so the numbers were only considered informational.

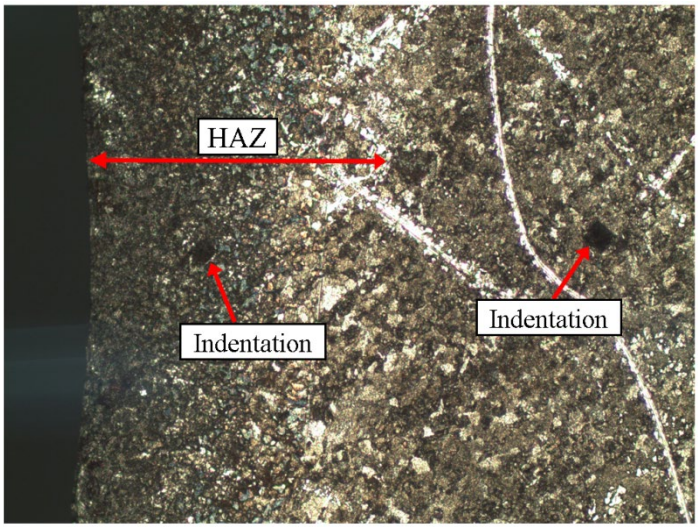

Source: FHWA.

Figure 26. Photo. Location of hardness indentations.

Table 7. HV around plasma-cut holes.

Specimen Series	Edge Distance (Inch)	Location 1[b,c,d]	Location 2[c,d]	Location 3[c,d]	Location 4[c,d]	Average[c,d]
C1-50	0.007[a]	329	355	299	343	332
	0.039	167	175	182	191	179
	0.137	181	188	162	214	186
C1-50W	0.008[a]	339	388	364	262	338
	0.039	200	194	181	189	191
	0.137	199	183	184	183	187
C2-36	0.012[a]	417	419	431	415	421
	0.040	199	205	201	223	207
	0.240	167	167	171	166	168
C2-50W	0.012[a]	390	388	416	433	407
	0.040	272	208	239	193	228
	0.250	185	187	204	180	189
E3	0.009[a]	539	402	409	406	439
	0.043	207	211	212	227	214
	0.157	208	196	187	216	202
E4	0.008[a]	341	382	374	388	371
	0.039	193	291	188	206	220
	0.137	176	187	185	200	187

[a]Measurement taken within the HAZ.
[b]Coincides with arc-termination notch.
[c]See figure 24 for reference to locations 1 through 4 around the hole perimeter.
[d]Measurements provided in units of HV related to HV(500 g). ASTM E384 is only written in metric; 500-g force is equal to 1.102 lb.[13]

FATIGUE TESTING

Stress–life (S-N) curves for plasma-cut holes were constructed from constant-amplitude tensile-fatigue tests of 279 specimens. The following sections discuss the specifics of the specimen design, test matrix, fatigue loading, and analysis of the results.

FATIGUE TEST MATRIX

Two different specimen geometries were tested for all series: steel plates with a single open plasma-cut hole, referred to as plate-fatigue specimens, and bolted steel plates with a group of plasma-cut holes, referred to as connection-fatigue specimens. All specimens were 6-inch-wide, ½-inch-thick plates. The plate-fatigue specimens had a single $^{15}/_{16}$-inch-diameter hole in the middle of the plate, while the connection-fatigue specimens had a two-by-two pattern of $^{15}/_{16}$-inch-diameter holes at one end. Illustrations of each specimen type are shown in figure 27 and figure 28. The different edge distances for C- and E-series connection-fatigue specimens were a mistake in ordering—they were not intended to be variables. The connection-fatigue specimens were always tested in pairs as a bolted butt splice, as detailed in figure 29. The splice plates were 6-inch-wide, ½-inch-thick plates with eight drilled $^{15}/_{16}$-inch-diameter holes matching the hole pattern in the connection-fatigue plate specimens. The holes were filled with nonpretensioned $^{7}/_{8}$-inch-diameter ASTM A325 bolts.[14] The resulting bearing connection ensured an accurate lower bound for fatigue resistance of the plasma-cut holes without beneficial clamping forces.

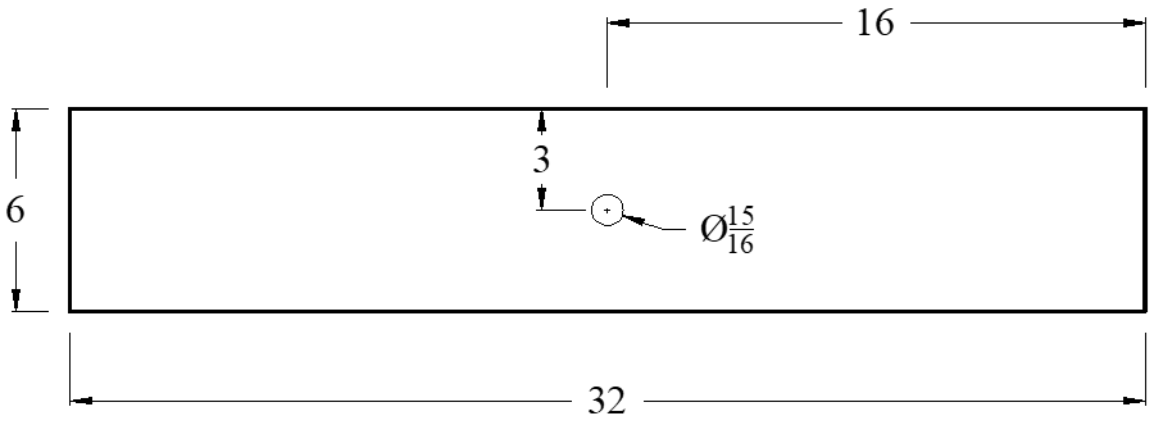

Source: FHWA.
⌀ = hole diameter.
Note: Units are in inches.

Figure 27. Schematic. Plate fatigue specimen geometry.

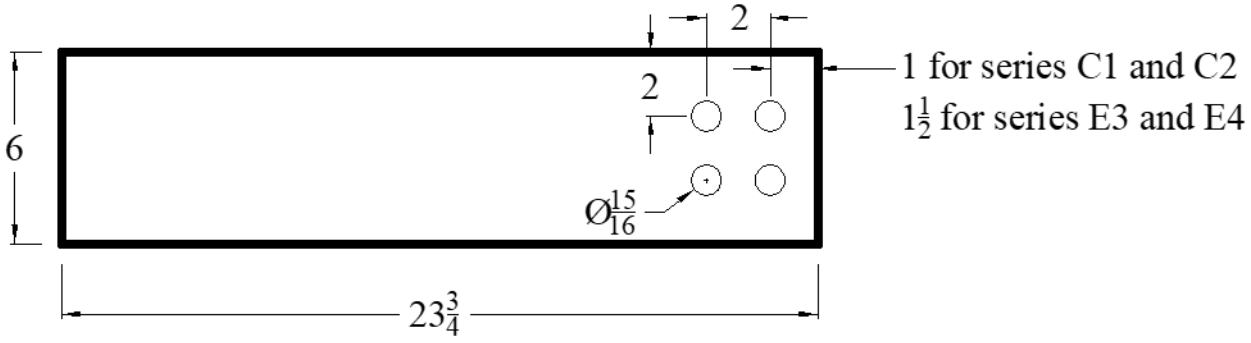

Source: FHWA.
⌀ = hole diameter.
Note: Units are in inches.

Figure 28. Schematic. Connection fatigue specimen geometry.

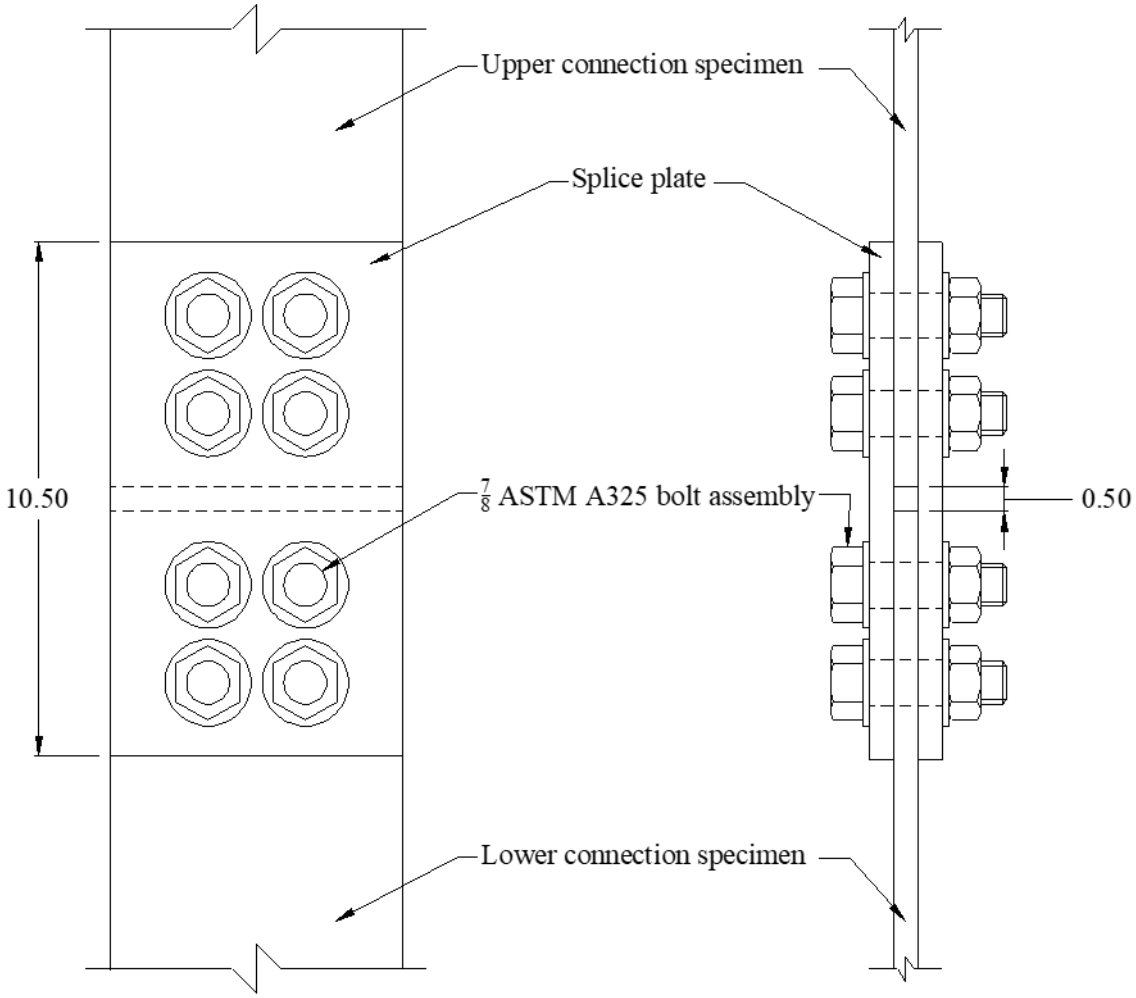

Source: FHWA.
Note: Units are in inches.

Figure 29. Illustration. Butt joint detailing of connection specimen assembly.

Fatigue resistance is significantly influenced by the presence of stress concentrations. Plasma-cut holes typically have a notch on the cut surface from the termination of the arc, and this was thought to be influential to their fatigue resistance. Therefore, location of the notch was specified to the fabricators providing the specimens. Figure 30 details how the arc-termination notch position was defined. The position identifications are symmetric with respect to the loading axis. It was anticipated that fatigue resistance would be maximized with the notch location at 90 degrees and minimized at 0 degrees.

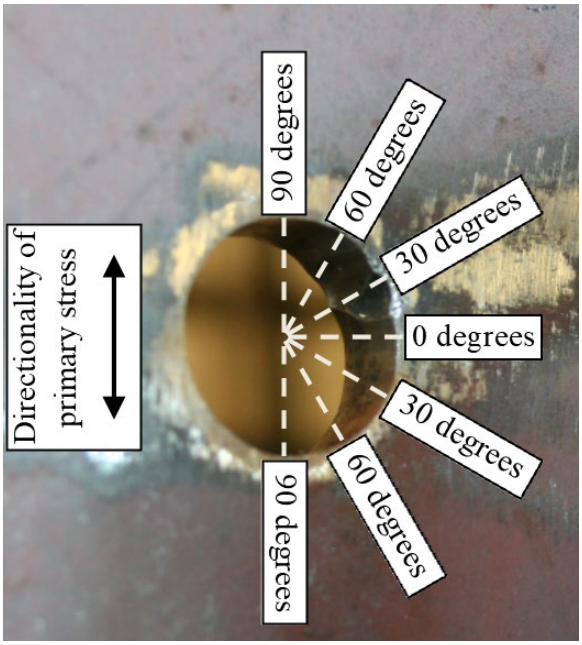

Source: FHWA.

Figure 30. Illustration. Arc-termination notch positioning.

The test matrices for the plate- and connection-fatigue specimen tests are provided in table 8 and table 9, respectively. The only variable included in these matrices is the approximate position of the surface discontinuity observed at the arc-termination notch point. Other factors, including steel grade and plasma shielding gas, are presented in table 1. Irrespective of the specified locations, the arc-termination notch position varied in specimens provided by fabricators C1 and C2. Series C1-50, C2-36, and C2-50 specimens had the arc-termination notch between 0 and 30 degrees. For the series C1-50W, the arc-termination notch point was at approximately 40 degrees. The position of the arc-termination notch was more strictly controlled on the specimens in series E3-50W and E4-50W at 0, 45, and 90 degrees.

Table 8. Plate fatigue test matrix.

Specimen Series	Arc-Termination Notch (Degree)	Number of Specimens
C1-50	0–30	15
C1-50W	31–60	25
C2-50W	0–30	15
C2-36	0–30	10
E3-50W	0	10
E3-50W	45	10
E3-50W	90	6
E4-50W	0	10
E4-50W	45	10
E4-50W	90	6

Table 9. Connection fatigue test matrix.

Specimen Series	Arc-Termination Notch (Degree)	Number of Specimens
C1-50	0–30	30
C1-50W	31–60	30
C2-36	0–30	30
E3-50W	0	14
E3-50W	45	14
E3-50W	90	8
E4-50W	0	14
E4-50W	45	14
E4-50W	90	8

FATIGUE TEST SETUP AND PROCEDURE

All fatigue tests were conducted under force-controlled constant-amplitude tensile loading at a cyclic rate of 5 Hz. The actual minimum and maximum cyclic loads for each specimen are reported in appendix B, although the minimum stress was constant for all specimens at 2.5 ksi. The test stress ranges varied between all the specimens between 12 and 24 ksi, resulting in a load ratio (R) variation between 0.10 and 0.21. Stress range calculations were based on the as-specified (nominal) net area (i.e., perfectly circular $^{15}/_{16}$-inch-diameter holes) unless noted otherwise.

Round-the-clock testing prohibited visual monitoring of the fatigue crack initiation for all fatigue tests. The test machines were set to shut off if the actuator displacement increased by 0.06 inches relative to the test initiation. This typically resulted in a fatigue crack extending from one side of the hole to the edge in plate-fatigue specimens and from the edge of the plate through two holes for the connection-fatigue specimens. This became the failure definition for the fatigue specimens. For connection-fatigue specimens, cracks always originated from holes and grew to the edge of the plate. Since the crack path was masked with coverplates connecting two specimens together, visual inspection was not possible. However, monitoring actuator piston displacements indicated a crack was growing and the test was stopped once a free edge crack was visually observed.

Three separate setups were operated simultaneously to carry out the fatigue tests. Each test setup consisted of a uniaxial load frame with a computer-controlled hydraulic actuator. Load values were measured using a load cell mounted in each load frame. Actuator displacement was measured using an internal linear variable differential transducer (LVDT) located within the test frame. Tensile load, actuator displacement, and cycle count were monitored and recorded using proprietary commercial software packages specific to the particular load frames.

Frame 1

Frame 1 was a 100-kip load frame and was used exclusively to conduct plate-fatigue tests. It was equipped with hydraulic grips with wedges that were 4 inches wide. Griping a 6-inch-wide plate with a 4-inch-wide wedge could lead to premature fatigue failures in the grip, so to mitigate that possibility, a custom grip adapter was machined that provided a gradual transition from the specimen to the wedges. The design of the adapter is shown in figure 31. Figure 32 and figure 33 show the main components of the frame and a closeup of the grip adapter, respectively. The adapter was bolted to the specimen with six ¾-inch ASTM A325 pretensioned bolts.[14] The hydraulic wedges then clamped directly onto the adapter.

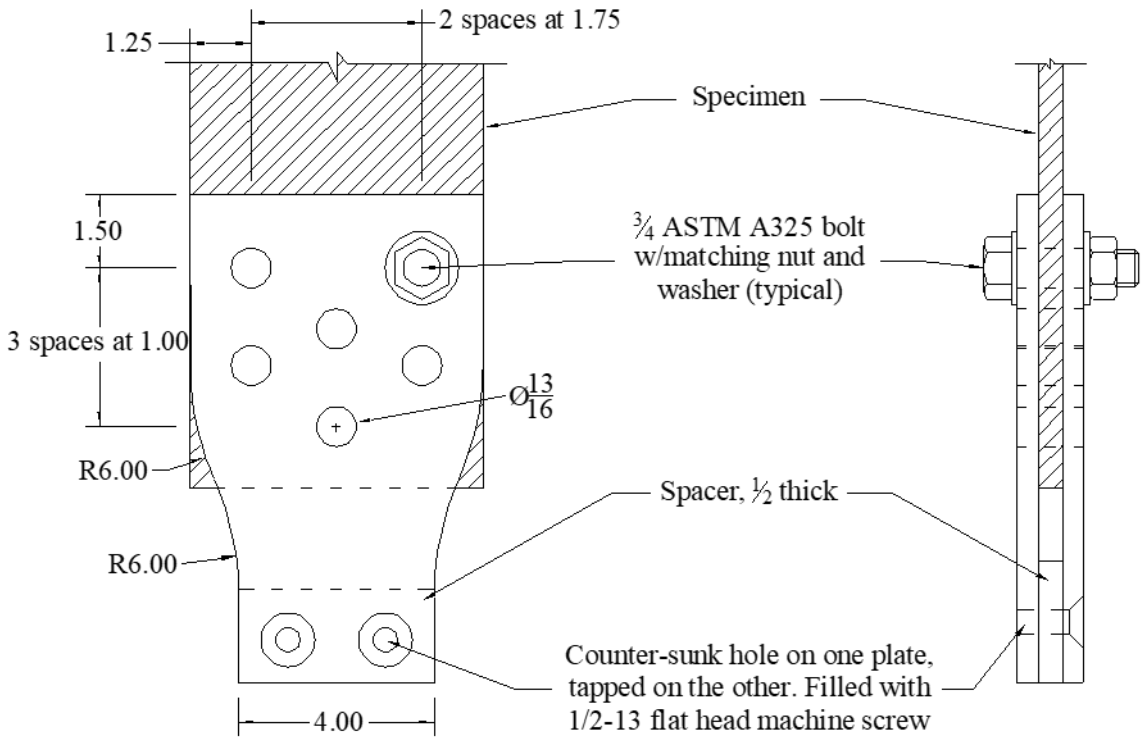

Source: FHWA.
⌀ = hole diameter.
Note: Units are in inches.

Figure 31. Illustration. Frame 1 grip adapter design.

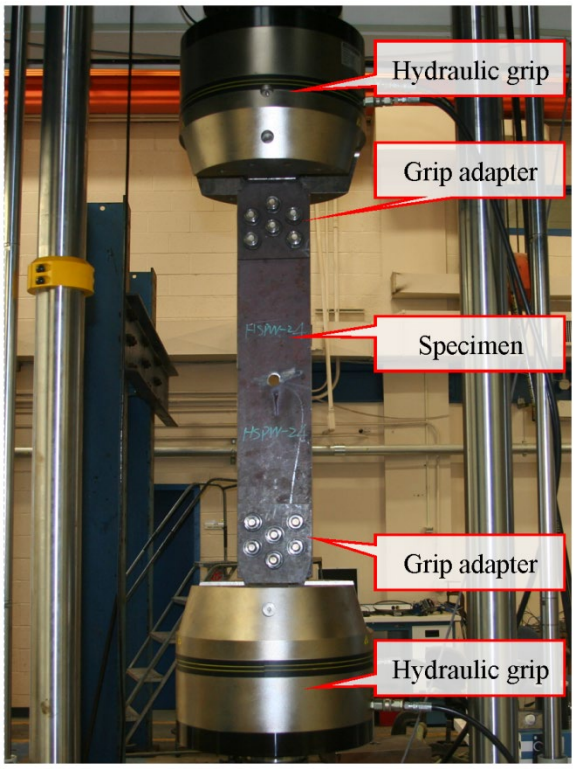

Source: FHWA.

Figure 32. Photo. Frame 1 with specimen installed.

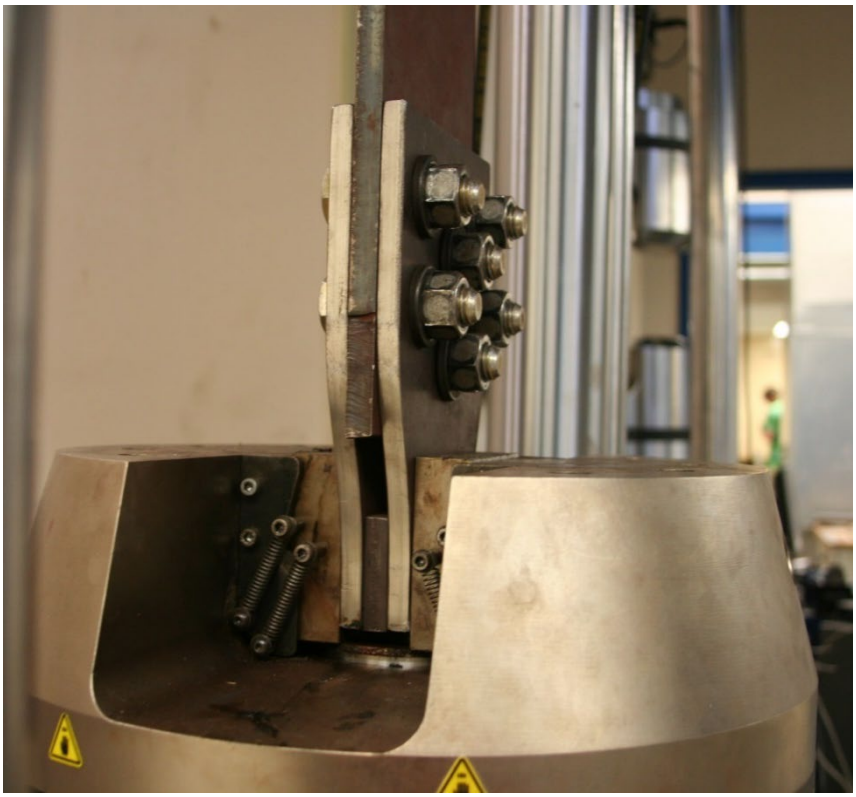

Source: FHWA.

Figure 33. Photo. Frame 1 lower grip with specimen and grip adapter installed.

Frame 2

Frame 2 was a 110-kip load frame used to test both plate- and connection-fatigue specimens. It did not have hydraulic grips and required fabrication of custom grips that directly attach to the testing frame and clamp the specimen. A specimen installed in frame 2 along with the custom grips is shown in figure 34. Each custom grip was constructed from three plates; two referred to as the sides and one referred to as the base. The detailing for the side and base plates of the grip is shown in figure 35 and figure 36, respectively. The grip was conceptualized as follows:

1. The base plate was tensioned to the load cell (at the top) and the piston (at the bottom) of the load frame with a 2-inch-diameter threaded rod.
2. The side plates were tensioned to the base plate with eight high-strength threaded rods.
3. The specimen was clamped between the side plates with six ¾-inch ASTM A325 bolts.[(14)]

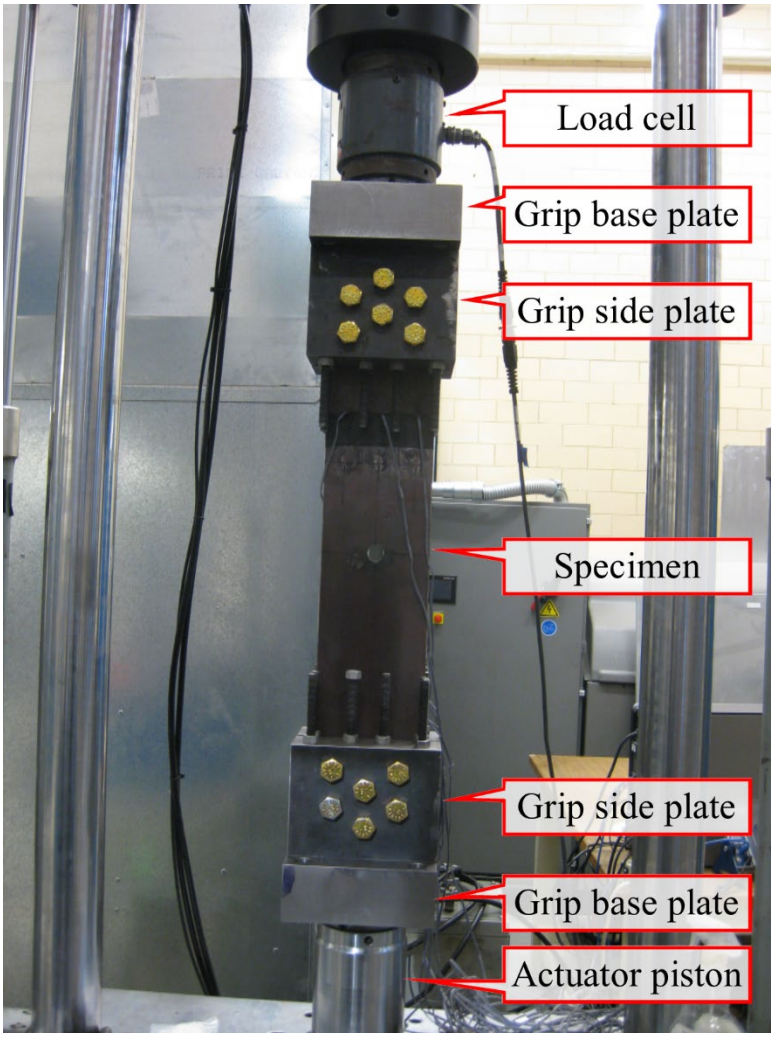

Source: FHWA.

Figure 34. Photo. Frame 2 with specimen installed.

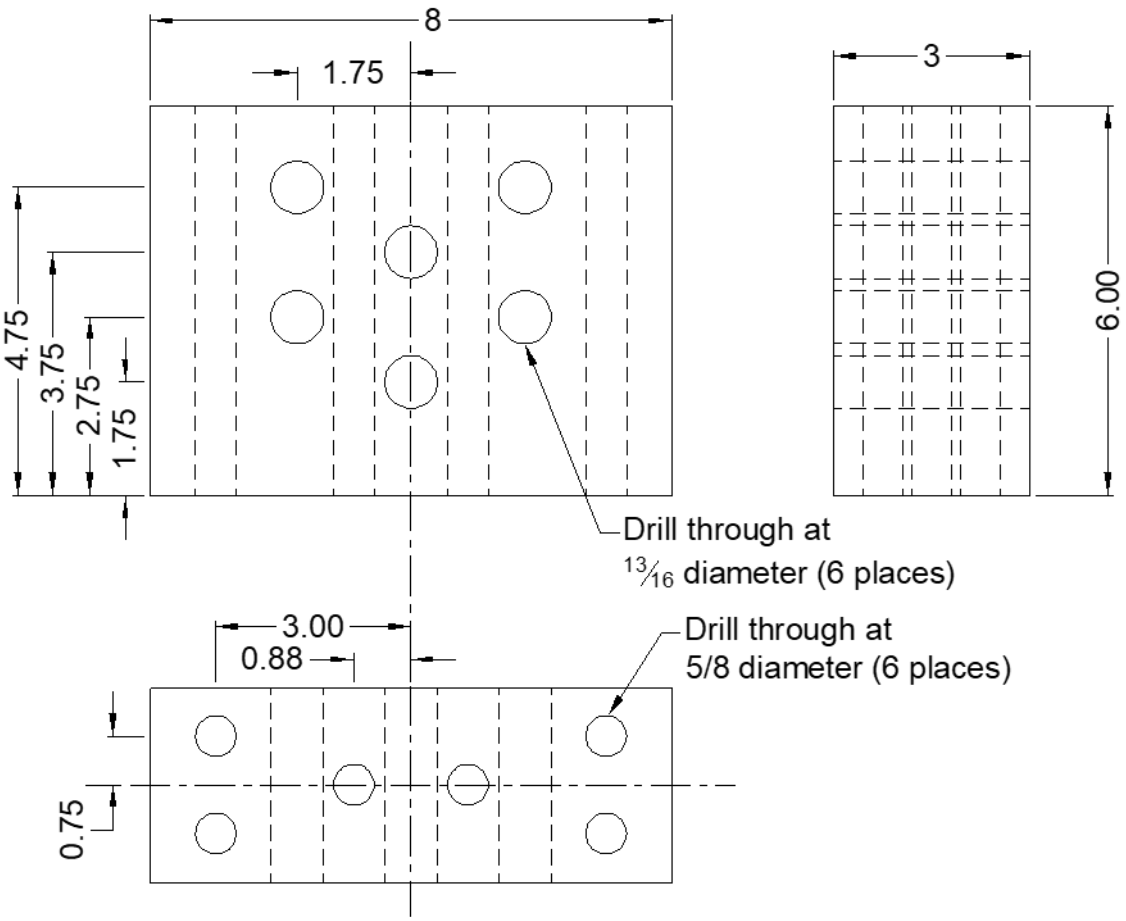

Source: FHWA.
Note: Units are in inches.

Figure 35. Illustration. Frame 2 side plate of custom grip design.

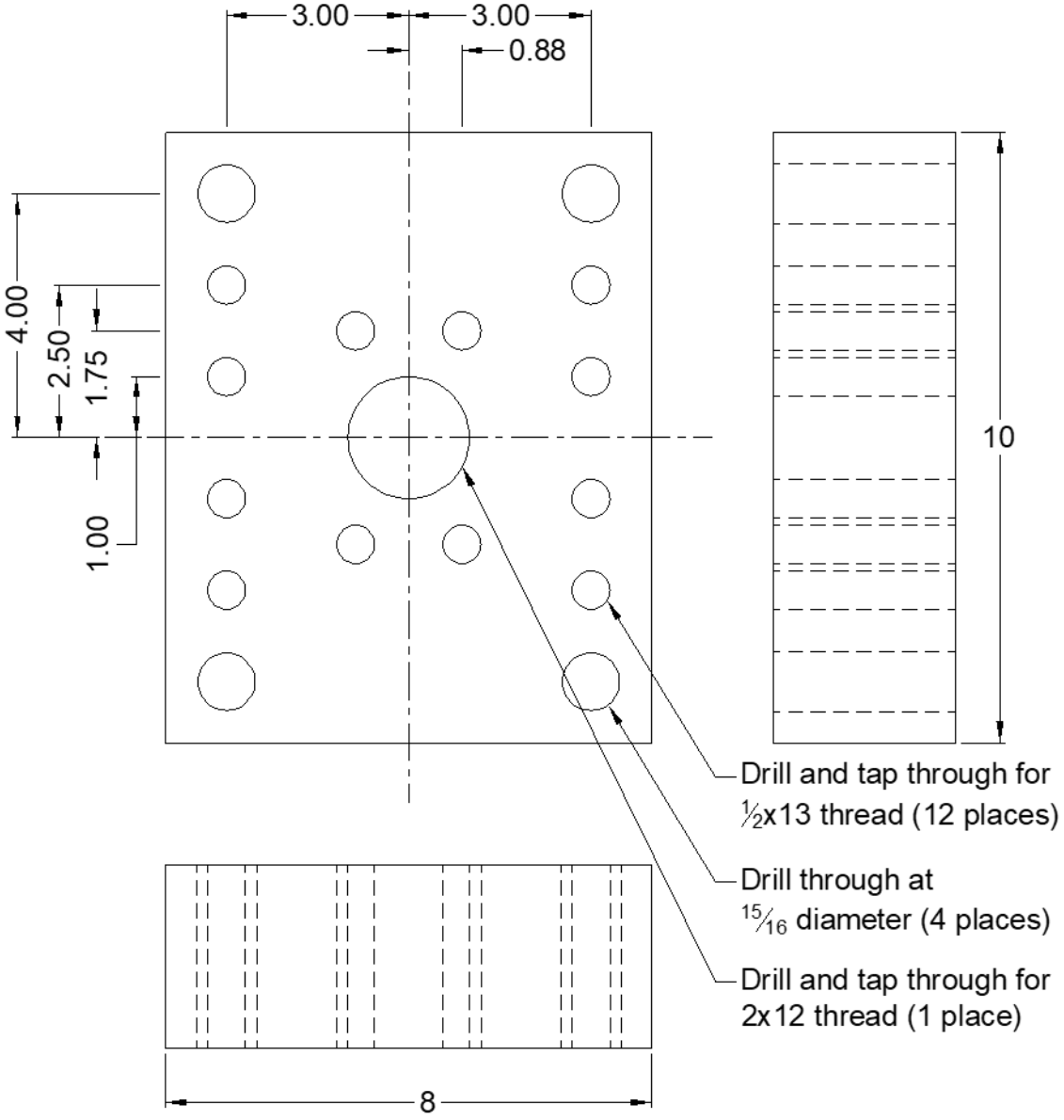

Source: FHWA.
Note: Units are in inches.

Figure 36. Illustration. Frame 2 base plate of custom grip design.

Frame 3

Frame 3 was a 220-kip load frame used to test both plate and connection specimens. It was equipped with hydraulic grips with wedges that were 5 inches wide. Since the width of the specimen and the wedges were close, all specimens were directly gripped without any adapters. A picture of frame 3 with a connection specimen installed is shown in figure 37.

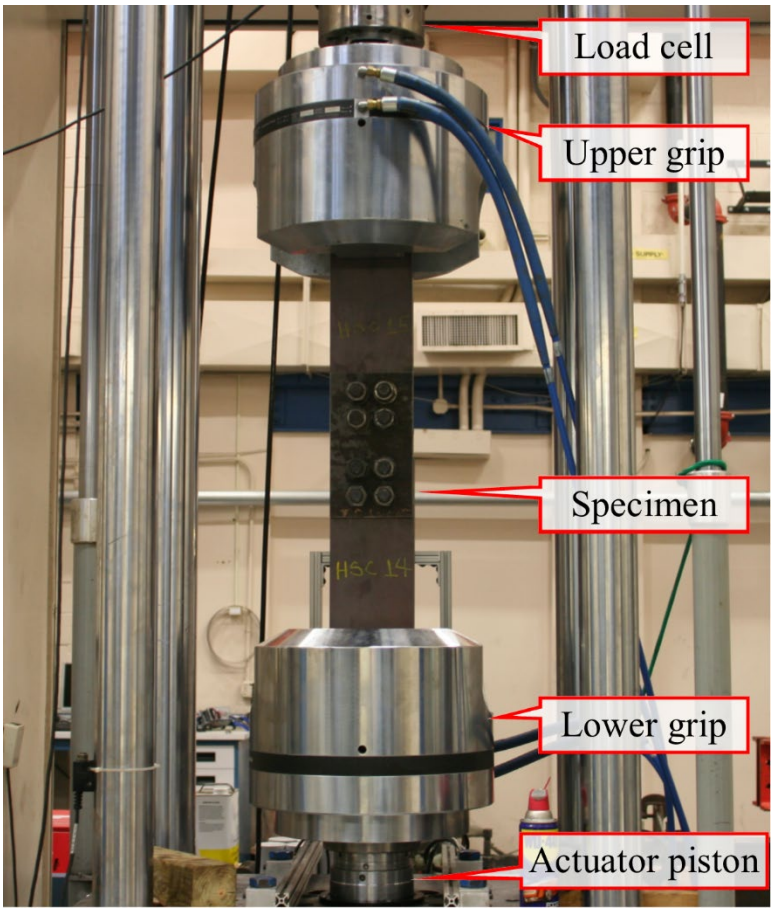

Source: FHWA.

Figure 37. Photo. Test setup in frame 3.

PLATE-FATIGUE TEST RESULTS

Raw data from all 117 plate-fatigue tests are reported in appendix B. All plate-fatigue test data are presented using S-N plots in log–log scale. The lower bound curve for each dataset, along with the fatigue design curves for the AASHTO LRFD BDS fatigue detail categories (i.e., A, B, C, D, and E), is provided.[(2)] The lower bound curves represent the mean minus two standard deviations of the sample, representing approximately a 2.5 percent survival rate, as it varies based on the sample size. The data were fit to a fixed slope of −3 for consistency with the AASHTO LRFD BDS. The S-N data points are displayed using various symbols. The lower bound curves corresponding to each dataset are represented by thick solid or thick dashed lines and labeled according to the dataset. Thin black lines show the AASHTO LRFD BDS fatigue design curves.

The final dataset contained significant scatter, which is notable on the S-N plots throughout this report. An initial analysis of the plate-fatigue data showed that a few test results had an excessive impact on the lower bound for certain groups of specimens. Specifically, specimens with a relatively high cycle life resulted in lower bound curves that did not appropriately reflect the fatigue strength of the dataset. To reduce the influence of these data points, any data point more than 3.5 standard deviations from the mean was labeled a potential outlier.[(15)] Next, these

potential outliers were subjectively examined by comparing cycle counts across all plate-fatigue tests. Data points deemed outliers and runout specimens were not considered in the determination of lower bound fatigue strength but are shown in the S-N curves. Overall, 102 tests provided usable data necessary to perform the regression analysis to determine lower bound fatigue resistances.

For comparison, the AASHTO LRFD BDS currently classifies open holes in steel bridge members as category D fatigue details, irrespective of whether they are drilled, punched full-size, or subpunched and reamed. It was not expected that plasma-cut holes could achieve a design resistance greater than category D.[(2)]

The fatigue performance of the plasma-cut holes is discussed in the following sections with respect to the influence of the experiment design variables, such as steel grade, fabricator, location of the arc-termination notch, and plasma-cutting process.

Steel Grade

The S-N plot in figure 38 presents all plate-fatigue test data with lower bounds calculated according to steel grade. The lower bound curve for holes in grade 50W is just above the category D design curve, whereas those for grade 36 and grade 50 are below category D and are nearly the same.

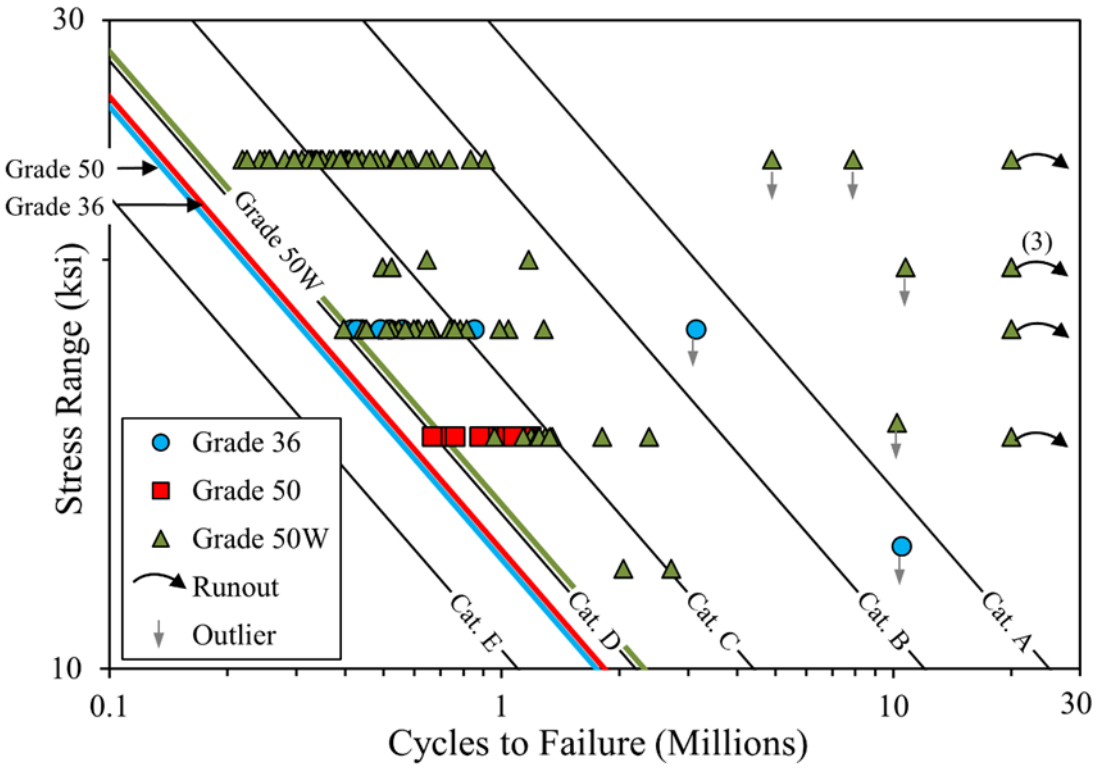

Source: FHWA.
(3) = three coincident points.
Cat. = category.

Figure 38. Graph. S-N plot for plate-fatigue tests grouped according to steel grade.

Fabricator

The S-N plot in figure 39 presents the data in terms of series. Effectively, this shows the same regression lines presented in figure 38 for grades 36 and 50 steel, so only grade 50W is split into additional datasets. Most of the lower bound data are around category D, with series C2-36, C1-50, C2-50W, and E3-50W falling just below category D and series C1-50W just above category D. The most notable is series E4-50W, which has a lower bound resistance halfway between categories D and C.

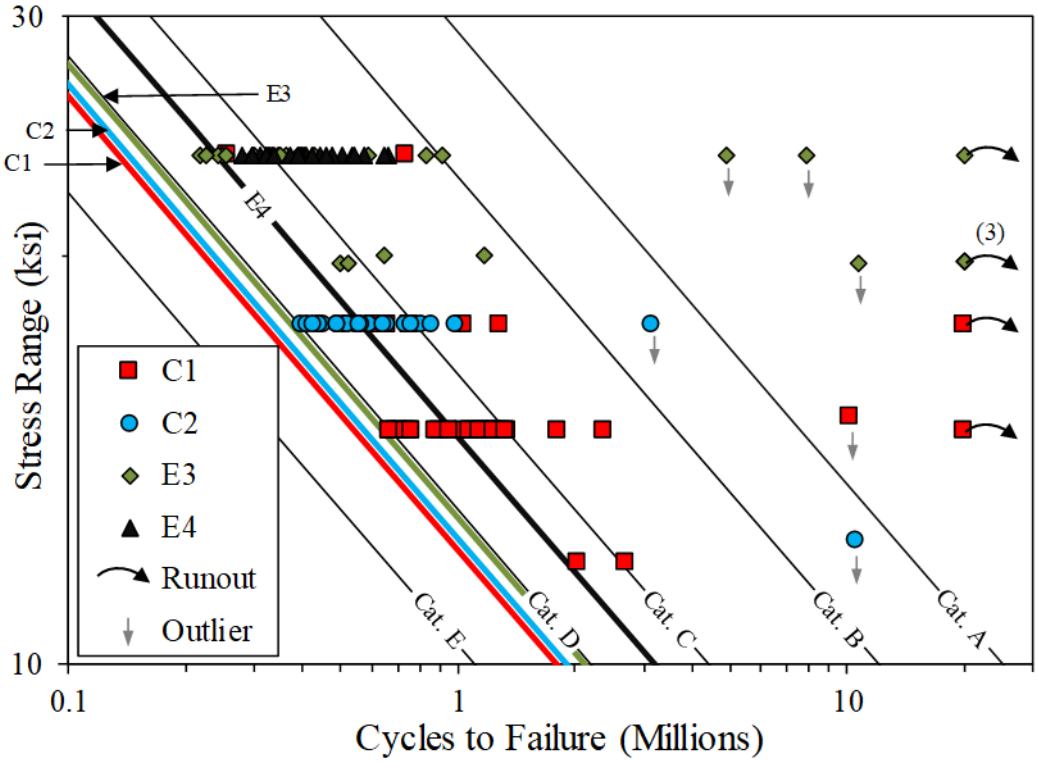

Source: FHWA.
(3) = three coincident points.
Cat. = category.

Figure 39. Graph. S-N plot for plate-fatigue tests grouped according to fabricator.

Arc-Termination Notch Location

The presence of the arc-termination notch was expected to significantly influence the fatigue strength of plasma-cut holes depending on its orientation with respect to the nominal stress. The notches were most pronounced on the specimens with conventional plasma-cut holes (i.e., C-series specimens). These notches were practically nonexistent on specimens with enhanced plasma-cut holes (i.e., E-series specimens). Figure 40 shows a typical series C1-50W plate specimen with the arc-termination notch on the hole at approximately 40 degrees with a fatigue crack initiating from this location. This happened in all but two of the C-series specimens. Figure 41 shows an E-series specimen with the arc-termination notch on the hole at 45 degrees; however, a fatigue crack initiated at 0 degrees—the point of maximum stress. None of the E-series specimens developed fatigue cracks at 45 or 90 degrees on the hole.

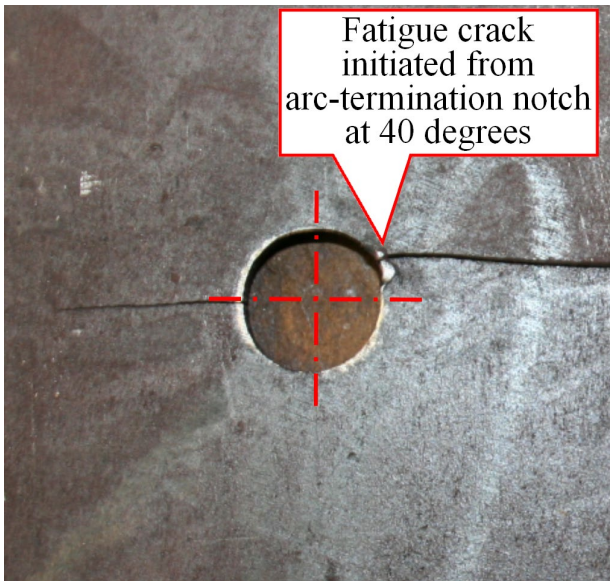

Source: FHWA.

Figure 40. Photo. Series C1-50W with a crack initiating from the arc-termination notch.

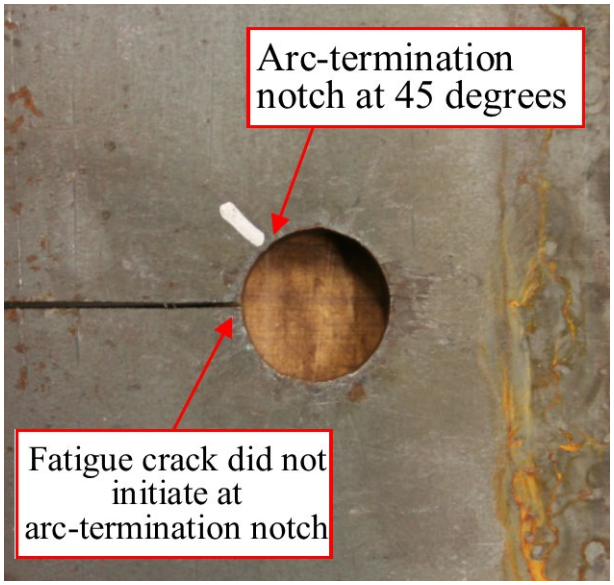

Source: FHWA.

Figure 41. Photo. Series E4-50W with a crack initiating at point of maximum stress.

Figure 42 shows the S-N plot of the C-series specimen data grouped by the position of the arc-termination notch on the hole. In addition to the data already eliminated from the regression (i.e., runouts and outliers) discussed earlier, the data corresponding to the cracks that did not initiate at the arc-termination notch were also eliminated for this plot. The location of the arc-termination notch on the hole is reported in appendix B for each specimen, but for the purpose of presenting the data, the locations are grouped by two zones: between 0 and 30 degrees and between 30 and 60 degrees. Only one series, C1-50W, had notches located on the hole between 30 and 60 degrees, and the lower bound resistance for this data group was slightly above category D. The other three series all had arc-termination notches on the hole between

0 and 30 degrees and exhibited lower bound resistances slightly less than category D. This is evidence that the location of the arc-termination notch can influence fatigue resistance, though the effect is minor. The data for the E-series specimens are presented in figure 43. Both fabricators for this series delivered specimens with distinct arc-termination notch locations on the holes, and all data are presented irrespective of whether the crack initiated at the arc-termination notch. In both E3 and E4 series specimens, no cracks initiated from the arc-termination notches on the hole at 45 or 90 degrees. For both E-series specimens, the lower bound resistance of the holes with arc-termination notches at 90 degrees was less than that of the holes with arc-termination notches at 0 and 45 degrees. This is contrary to the hypothesis that the arc-termination notch effect coupled with the hole stress concentration effect at 0 degrees would be worse than that at 90 degrees. This is better explained in table 10, which shows the AASHTO LRFD BDS A constant (i.e., the stress axis intercept constant) for the mean of the data and the standard error estimate for these E-series specimens. The A constant is minimized at 0 degrees, and the standard error increases when the arc-termination notch is at 45 degrees and even more when the arc-termination notch is at 90 degrees. Therefore, the notion that the lower bound resistance is lower for arc-termination notches at 90 degrees than arc-termination notches at 0 degrees is controlled by the standard error in the typical mean minus two standard deviation fatigue regression (i.e., this effect is a statistical aberration). The mean of the data provides proof that arc-termination notches at 0 degrees produce slightly lower fatigue resistance. More evident in the graph of figure 43 is the marked separation between the E3 and E4 series, with the fatigue resistance of E4 holes exceeding category D and E3 holes being less than category D.

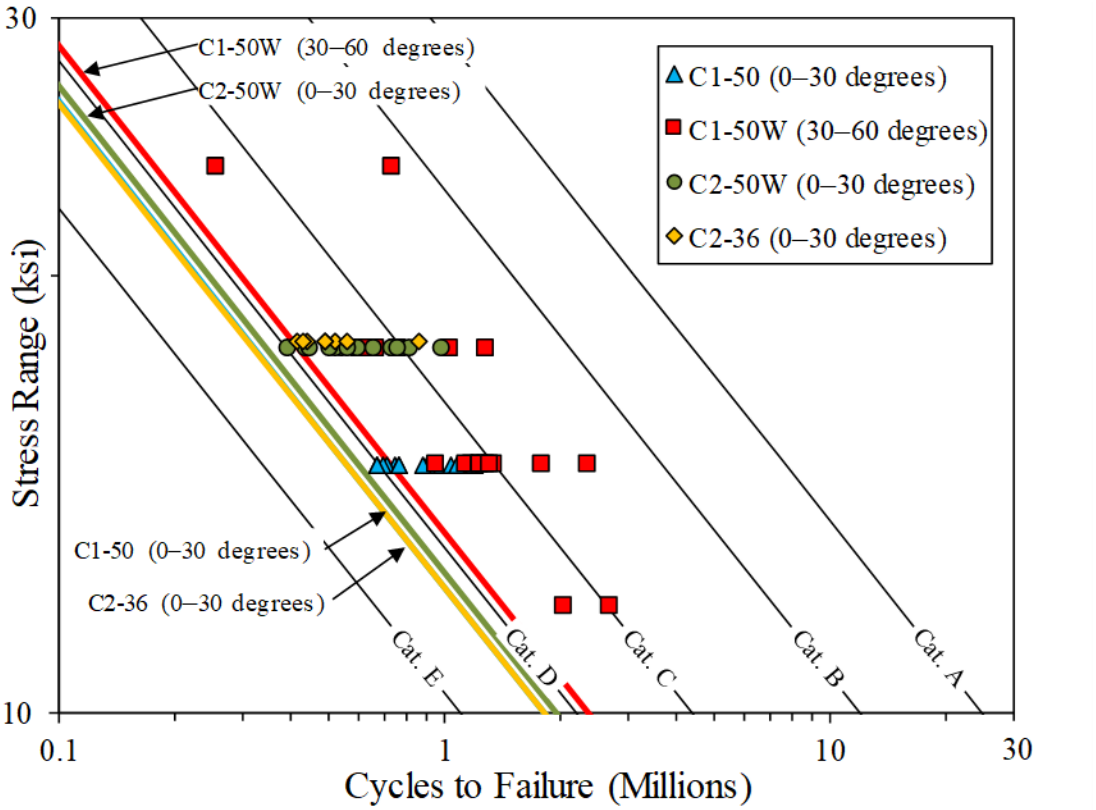

Source: FHWA.
Cat. = category.
Note: Runouts, outliers, and cracks not originating at the notch are not shown.

Figure 42. Graph. S-N plot for plate-fatigue tests by position of the arc-termination notch for conventional plasma-cut holes.

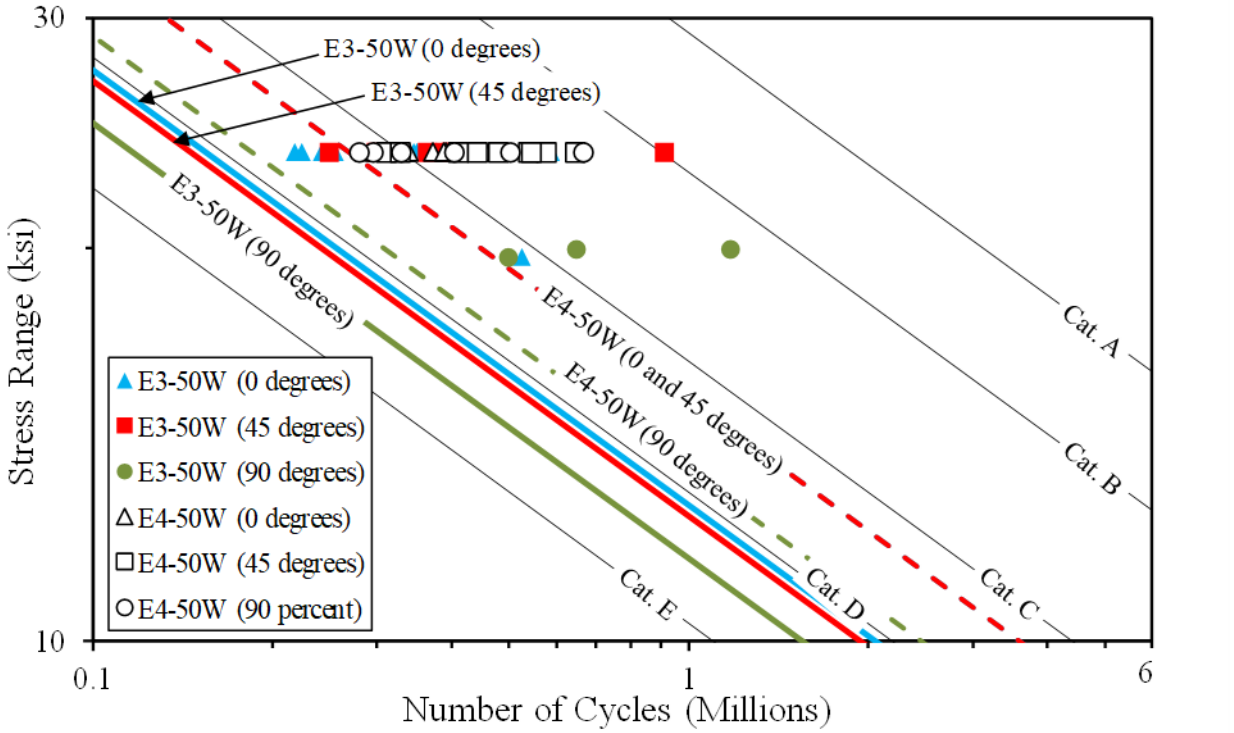

Source: FHWA.
Cat. = category.
Note: Runouts and outliers are not shown.

Figure 43. Graph. S-N plot for plate-fatigue tests grouped according to the position of the arc-termination notch on the hole.

Table 10. Mean statistics of E-series specimens.

Specimen Series	Position of Arc-Termination Notch (Degrees)	AASHTO Constant, A × 10^8 (ksi^3)[a]	Standard Estimate of Error in Log-Space	Number of Specimens
E3-50W	0	41.7	0.15	9
E3-50W	45	52.5	0.22	6
E3-50W	90	57.5	0.28	3
E4-50W	0	47.9	0.06	10
E4-50W	45	61.7	0.12	9
E4-50W	90	52.5	0.16	6

[a]For reference, constant A equals 120.0 × 10^8 for category B details, equals 44.0 × 10^8 for category C details, and 22.0 × 10^8 for category D details.

Plasma Process

The S-N plot in figure 44 presents the data in terms of the conventional and enhanced plasma-cutting processes, combining results for all plate-fatigue specimens without consideration

of fabricator, steel grade, or location of the cut-termination notch on the hole. Combining the results from all tests into a single dataset provides the most pragmatic means to judge the fatigue performance of the plate-fatigue specimens for two key reasons. First, the location of the cut-termination notch, in conjunction with the local stress around the hole, can significantly affect the fatigue strength of the hole, and fabricating each hole to favorably accommodate this effect would slow fabrication time and increase the need for quality control (i.e., inspection for the presence and location of a cut-termination notch). Second, the fatigue resistance of plasma-cut holes in plate-fatigue specimens was not much different when sorted by steel grades and fabricators. Therefore, to be consistent with fatigue design provisions in the AASHTO LRFD BDS, the S-N data were evaluated independent of steel grade.[2] Moreover, the fatigue design provisions in the AASHTO LRFD BDS were developed without consideration of the fabricator but with consideration of the quality of fabrication. Through visual inspection, the mean of the conventional plasma-cut hole data is less than category C but the mean of the enhanced HD plasma-cut hole is greater than category C. The lower bound fatigue resistance (consistent with the AASHTO LRFD BDS fatigue design provisions) of open holes cut by the two plasma-cutting processes were similar and fell between categories D and E. Open plasma-cut holes, regardless of the cutting process, are classified category E, which is one category lower than the current classification for open holes in the AASHTO LRFD BDS.[2] Figure 45 shows all the data together with the lower bound regression indicated by a heavy line between categories D and E.

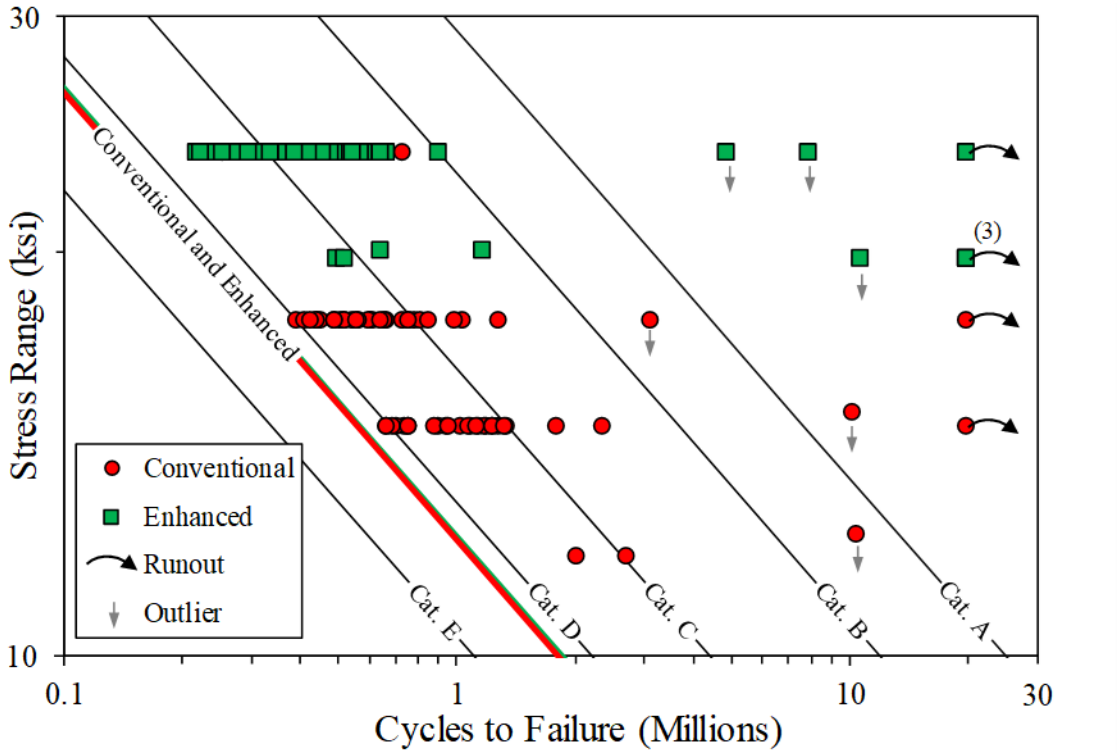

Source: FHWA.
(3) = three coincident points.
Cat. = category.

Figure 44. Graph. S-N plot for all plate-fatigue tests per plasma process.

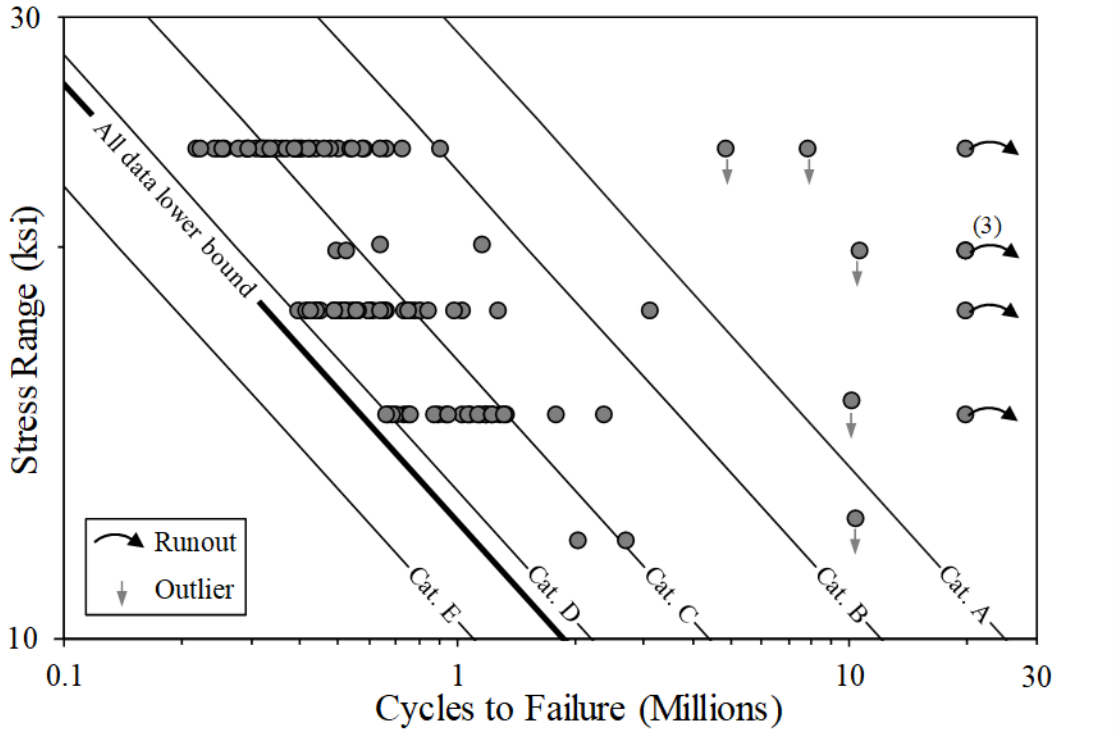

Source: FHWA.
(3) = three coincident points.
Cat. = category.

Figure 45. Graph. S-N plot for all plate-fatigue tests.

CONNECTION-FATIGUE TEST RESULTS

The raw data from all 162 connection-fatigue tests are reported in appendix B. A typical failed connection specimen with a fatigue crack is shown in figure 46. Ultimately, 150 tests provided usable data to calculate the lower bound curves for the connection-fatigue tests after runouts and outliers were excluded from the analysis. The method used to identify outliers in plate-fatigue test data was also applied to connection-fatigue test data. The fatigue data, estimated lower bound fatigue resistance curves, and AASHTO LRFD BDS fatigue design curves are presented in S-N plots. Since the bolts were only finger tightened, plasma-cut holes were expected to be category D fatigue details.

The fatigue performance of the plasma-cut holes in the connection-fatigue specimens is discussed in the following sections with respect to influence of the experiment design variables, including steel grade, fabricator, location of the arc-termination notch, and plasma-cutting process.

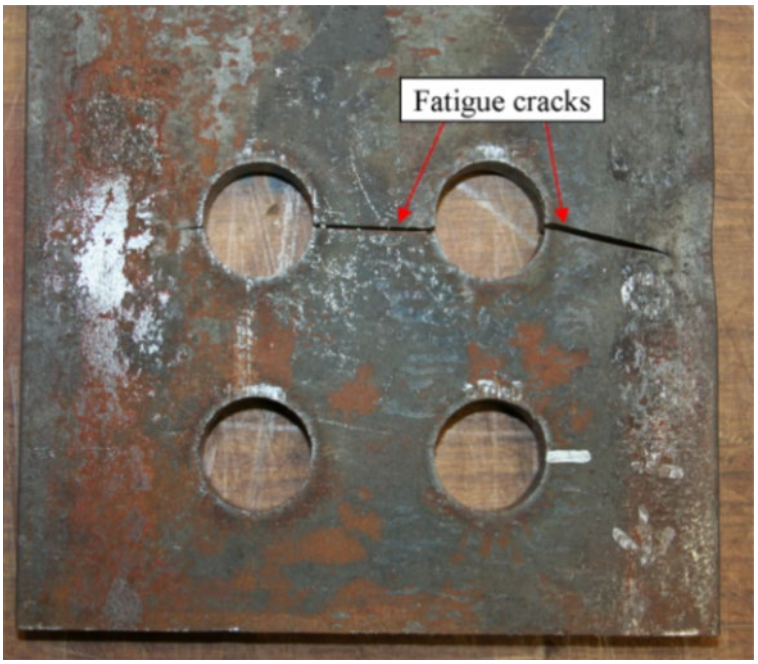

Source: FHWA.

Figure 46. Photo. Fatigue cracked connection specimen.

Steel Grade

All connection-fatigue test data are reported on the S-N plot in figure 47 and are grouped according to steel grade. The connection-fatigue specimens showed the same trend as the plate-fatigue specimens, with the grade 36 and 50 specimens having the same fatigue strength, but less than that of grade 50W. The lower bound fatigue resistance for grade 50W was between categories D and E, while that of grade 36 and 50 was less than category E.

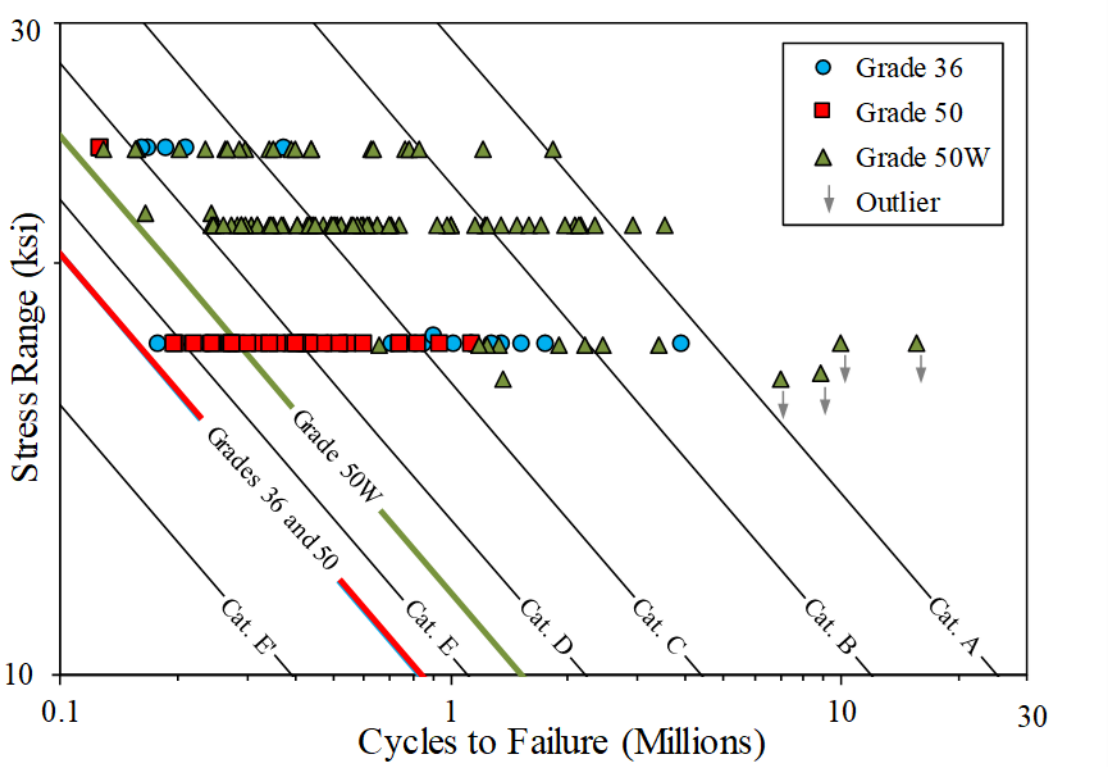

Source: FHWA.
Cat. = category.

Figure 47. Graph. S-N plot for connection-fatigue tests grouped according to steel grade.

Fabricator

Figure 48 presents the connection-fatigue test data grouped according to fabricator. The best lower bound fatigue resistance was achieved by fabricator E4, followed by fabricator E3, although both were less than category D. Both fabricators C1 and C2 had lower bound resistance less than category E.

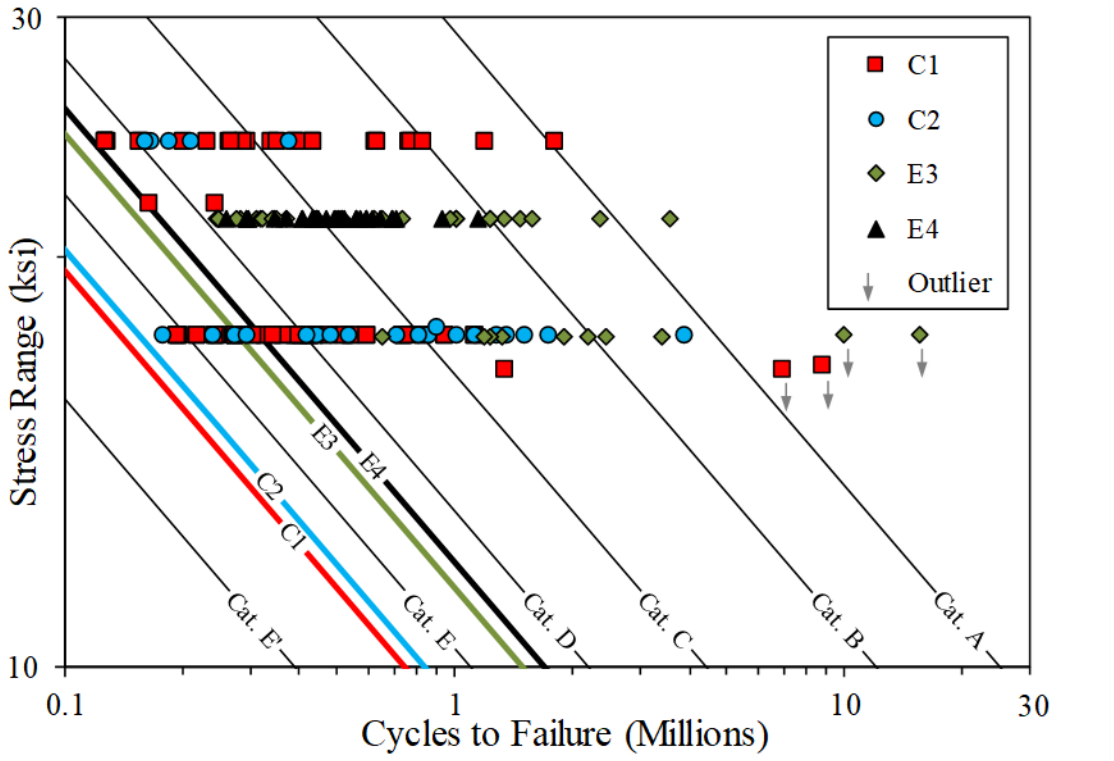

Source: FHWA.
Cat. = category.

Figure 48. Graph. S-N plot for connection-fatigue tests grouped according to fabricator.

Arc-Termination Notch Location

The raw data for all the connection-fatigue tests are reported in table 26 through table 36 in appendix B. Table 26 through table 36 also provide the angle of the arc-termination notch and whether the fatigue crack originated from this location. For the conventional plasma-cutting process, the crack overwhelmingly originated from the arc-termination notch, with a couple isolated exceptions in series C1-50W. For the enhanced plasma-cutting process, none of the 90-degree specimens cracked from the arc-termination notch, though all of the 0-degree specimens did. The 45-degree specimens showed mixed results, though more of the specimens showed the arc-termination notch initiating the crack than did not.

Since the conventional plasma-cut holes in the connection-fatigue specimens had arc-termination notches over a range of angles, the test data for the connection-fatigue specimens presented in figure 49 are grouped similarly to those for the plate-fatigue specimens shown in figure 42. Both series C1-50 and C2-36 specimens had arc-termination notches located between 0 and 30 degrees with respect to the loading direction (figure 30). Both these specimen series had identical lower bound fatigue resistance, which was less than category E. For series C1-50W with the arc-termination notch located between 30 and 60 degrees, the lower bound fatigue resistance exceeded category E. The trend was similar to the plate-fatigue specimens except for approximately one fatigue category reduction in the lower bound fatigue resistance and a little more separation between the series with different arc-termination notch locations. The

connection-fatigue test results of enhanced plasma-cut holes are presented in figure 50. A lower fatigue strength was expected from the specimens with arc-termination notch at 0 degrees. As seen in the plot, both series E3-50W (0 degrees) and E4-50W (0 degrees) exhibited a lower bound fatigue resistance of category E. For each series, the specimens with arc-termination notches at 45 and 90 degrees demonstrated nearly identical lower bound resistance, albeit greater than the specimens with a arc-termination notch at 0 degrees. The series E3-50W (45 degrees) and E3-50W (90 degrees) specimens exhibited a lower bound fatigue resistance greater than category D, and the series E4-50W (45 degrees) and E4-50W (90 degrees) specimens exhibited a lower bound fatigue resistance less than category D.

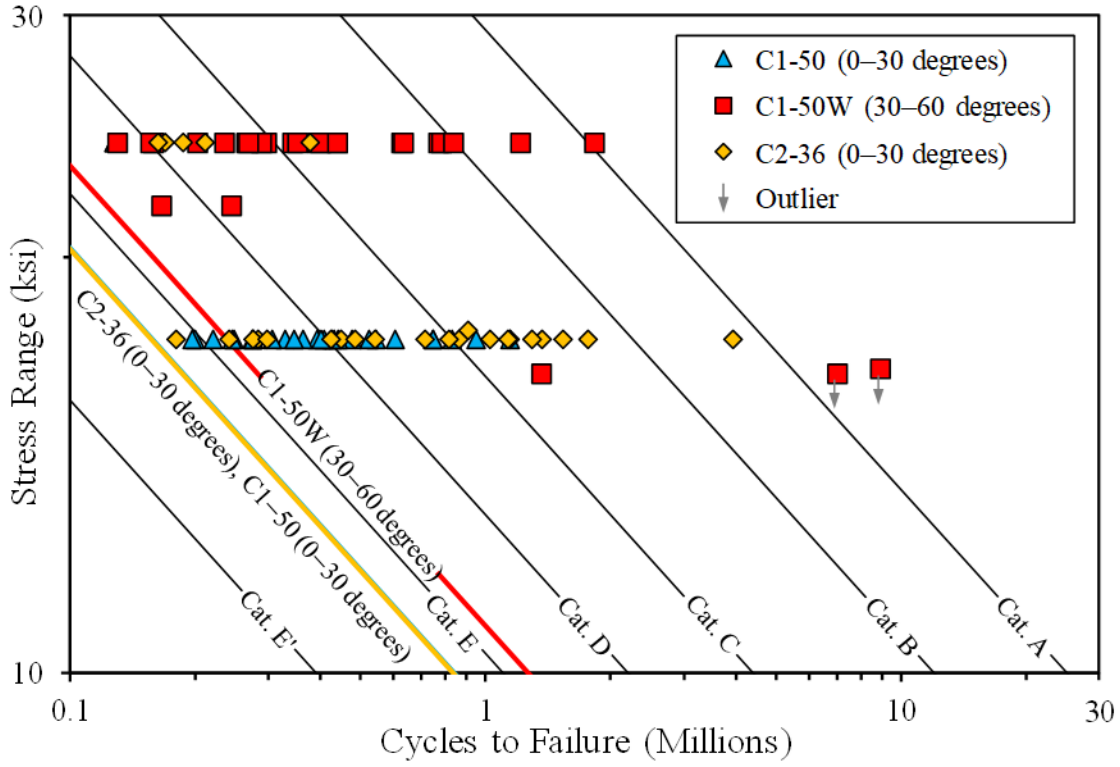

Source: FHWA.
Cat. = category.

Figure 49. Graph. S-N plot for connection-fatigue tests grouped according to the position of the arc-termination notch for conventional plasma.

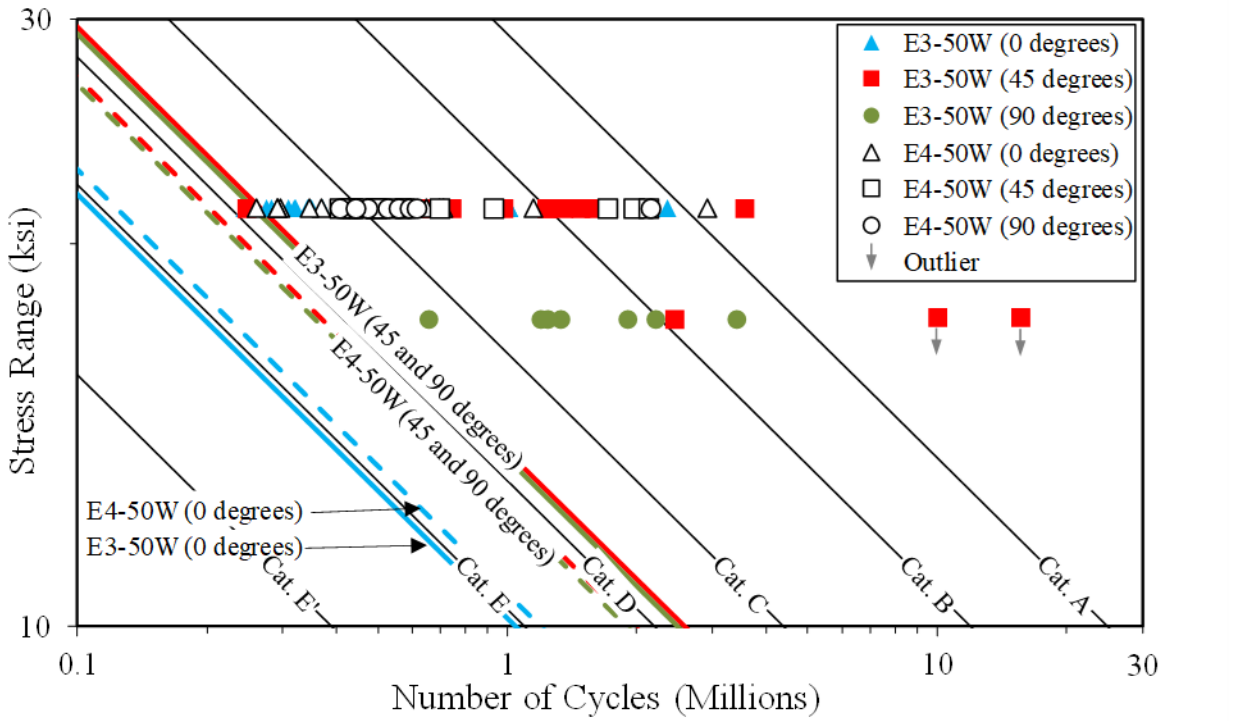

Source: FHWA.
Cat. = category.

Figure 50. Graph. S-N plot for connection-fatigue tests grouped according to the position of the arc-termination notch for enhanced plasma.

Process

All the connection-fatigue test data presented in figure 51 are grouped by conventional and enhanced plasma-cutting processes. Both conventional and enhanced plasma-cut holes in the connection-fatigue specimens exhibited lower bound fatigue resistance between categories E and E′ with the enhanced plasma-cut holes showing higher fatigue resistance. Accordingly, the plasma-cut holes in nonpretensioned bolted connections are classified as category E′ fatigue details, irrespective of the plasma-cutting process. Analysis of test data for all connection-fatigue specimens is presented in figure 52. The plasma-cut holes in nonpretensioned (i.e., bearing-type) bolted connections have a lower bound fatigue resistance less than category E and are classified as category E′ fatigue details. This is a reduction of two categories in design strength from the current category D classification for open holes in the AASHTO LRFD BDS.

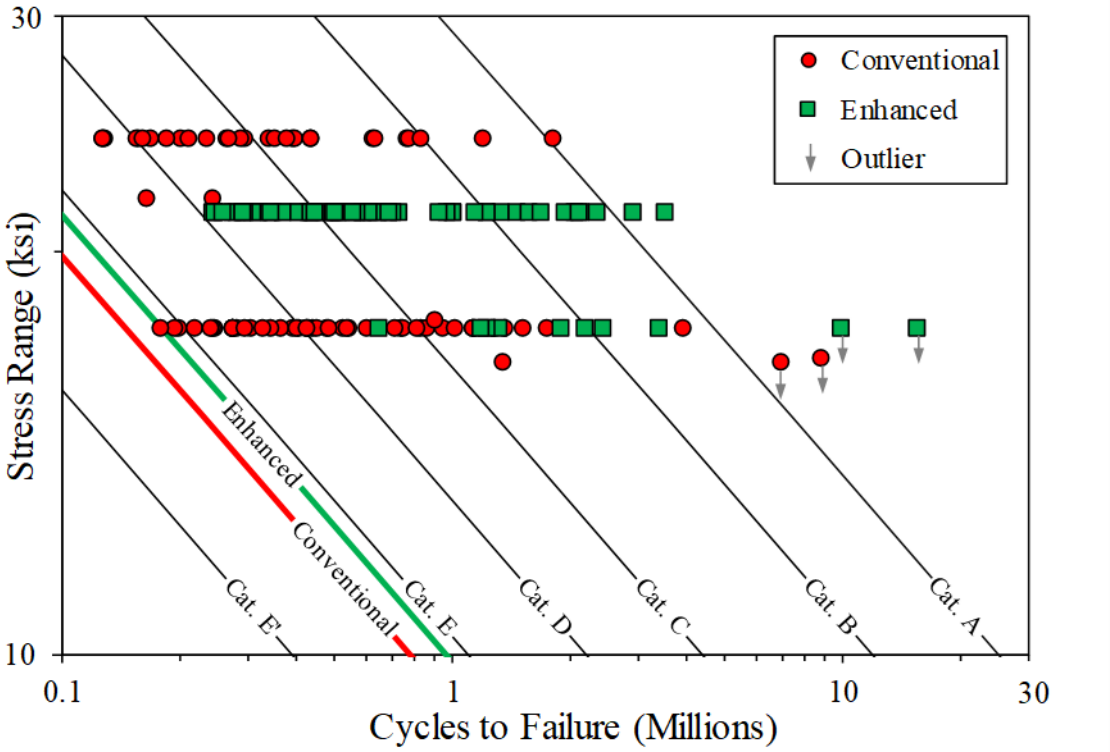

Source: FHWA.
Cat. = category.

Figure 51. Graph. S-N plot for all connection-fatigue tests grouped by plasma-cutting process.

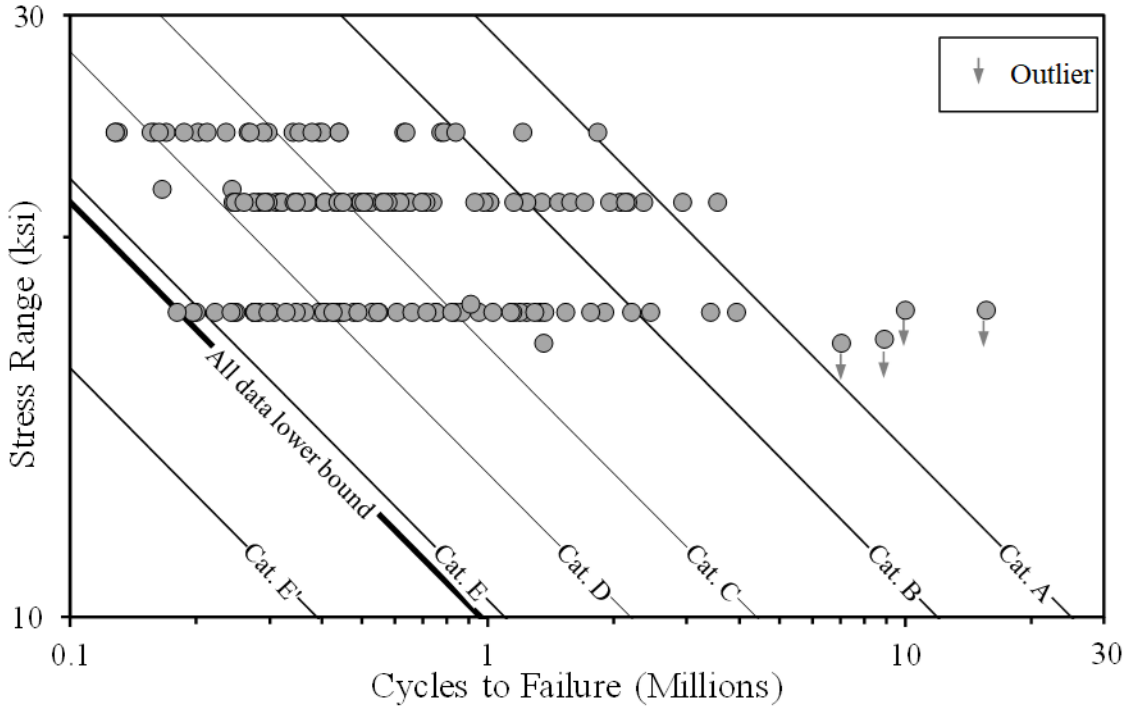

Source: FHWA.
Cat. = category.

Figure 52. Graph. S-N plot for all connection-fatigue tests.

PLASMA-CUT HOLES IN PRETENSIONED JOINTS

The fatigue test results presented hitherto were obtained from bearing connections with nonpretensioned (i.e., snug-tight) bolts. However, connections in steel bridge structures are often specified/designed as slip-critical or designed as bearing connections but installed and fabricated to meet slip-critical requirements.[(2)] In either case, the bolts within the joint are pretensioned during installation and are classified as category B fatigue details with the only difference being if the stress range is calculated with gross or net section properties. To investigate the effect of bolt pretension on the fatigue resistance of bolted connections with plasma-cut holes, four connection specimens of series C2-36 were tested with the bolts tensioned. The connection assembly was first installed in the testing machine with the bolts just finger-tight. The specimen was then subjected to 1-kip tension, which allowed the bolts to go into bearing. Because of tolerance on the hole *D* and spacing between the individual holes, the load distribution between the bolts was not equal. The bolts were then uniformly snugged, followed by tightening each heavy hex nut ⅓ of a rotation from the snug-tight position.

Visual inspection of all four connection-fatigue specimens confirmed the absence of any fatigue cracking. The tensile fatigue load was resisted by friction forces between the faying surfaces in the pretensioned joints. This effect is illustrated by comparing the post-test faying surface of the plate-fatigue specimen from a typical pretensioned connection-fatigue test (figure 53) and a typical finger-tightened (i.e., bearing) connection test (figure 54). The faying surface of figure 53 looks no different than an as-fabricated connection-fatigue specimen, whereas the faying surface of figure 54 was burnished from the cyclic shearing. Transfer of load through friction reduced

the stress concentration around the holes, rendering the connection less sensitive to the hole quality. The data for the two potential stress range calculations from the four runout specimens are shown in figure 55. Since the specimens were all tested at the same stress range and were declared a runout at the same cycle count of 10 million cycles, all data appear as one point.

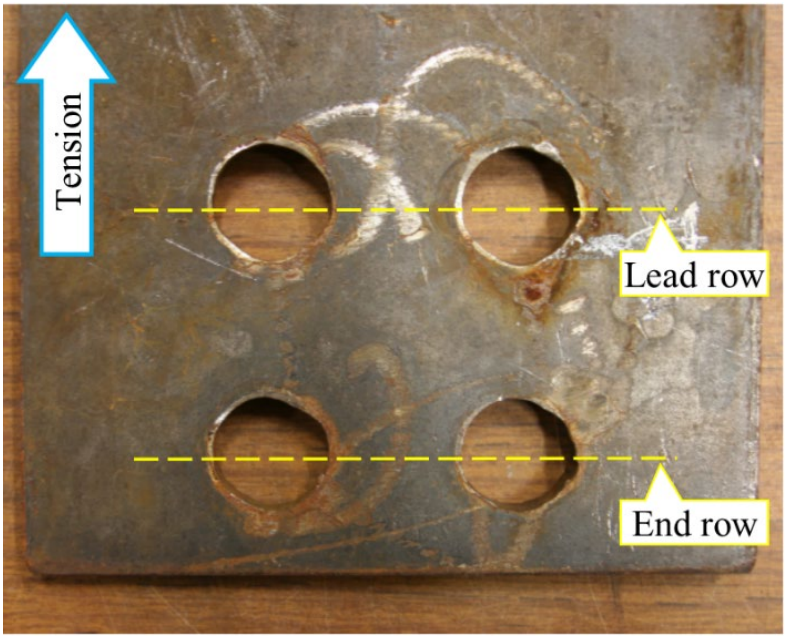

Source: FHWA.

Figure 53. Photo. Pretensioned connection specimen.

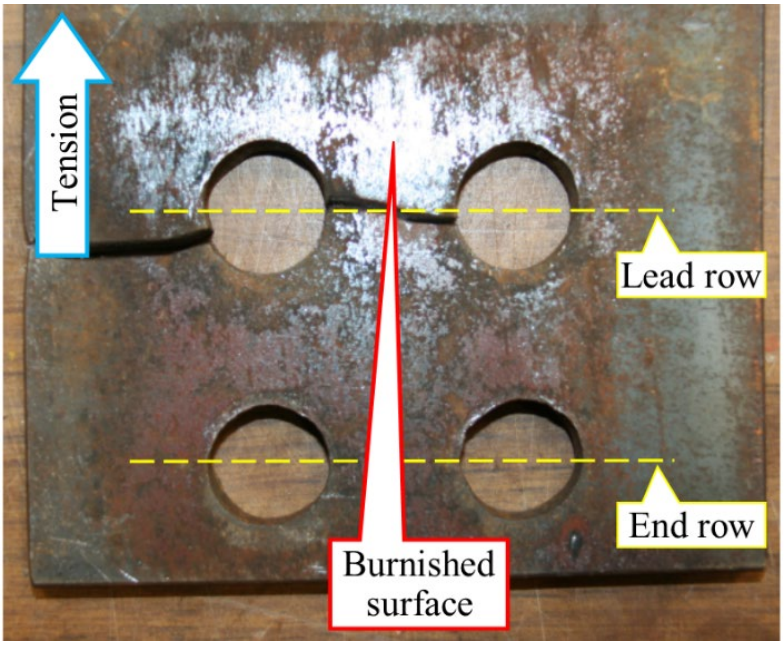

Source: FHWA.

Figure 54. Photo. Bearing connection specimen.

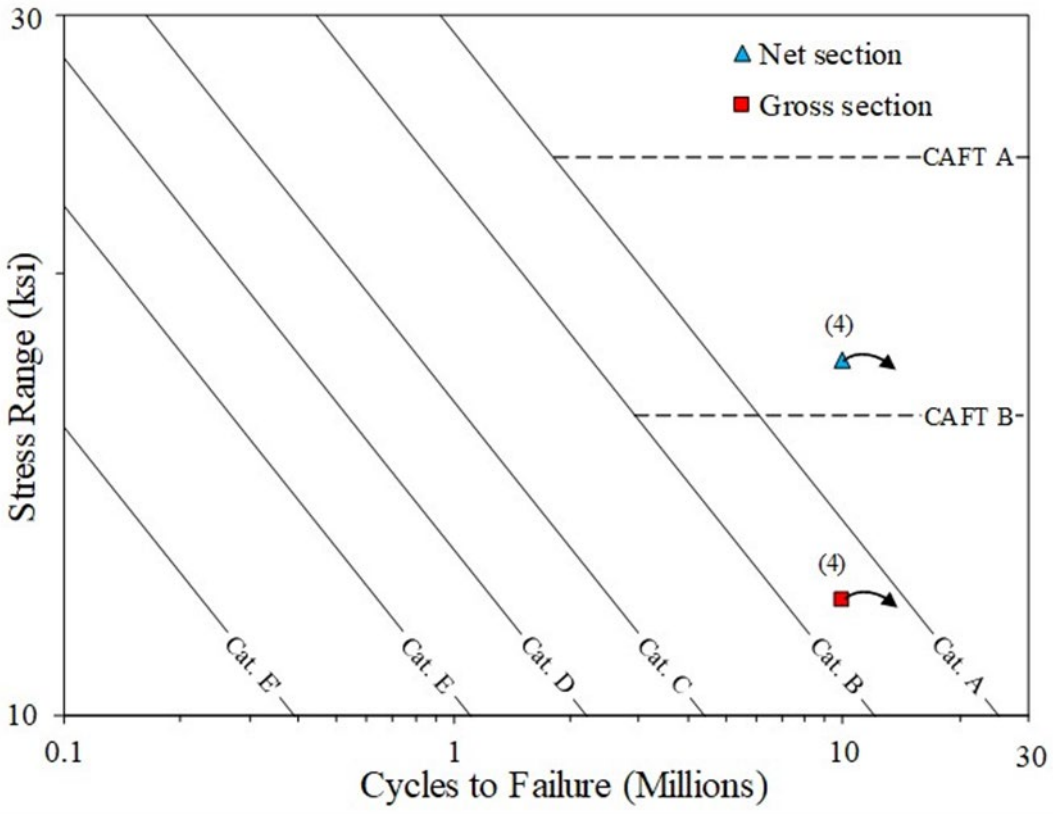

Source: FHWA.
(4) = four coincident points.
CAFT = constant amplitude fatigue threshold; Cat. = category.

Figure 55. Graph. S-N plot for pretensioned bolt connection fatigue tests.

The specimens were tested with bolts in a bearing condition, though pretensioned, and the faying surface was clean mill scale. In this condition, the results should be compared to category B using the net section stress range consistent with the design philosophy of the AASHTO LRFD BDS.[(2)] Using the net section stress range, the data points plot above the category B constant amplitude fatigue threshold (CAFT) and finite life line, indicating they met the design intent of infinite life. Furthermore, the pretensioned bearing bolts demonstrated infinite life performance using series C2-36 specimens that displayed the lowest fatigue performance of all the test series (figure 47). Though they were not tested in this manner, the enhanced HD plasma-cut holes would not be expected to perform any worse because their cut quality was better. Unfortunately, plasma-cut holes in a slip-critical condition were not tested. Per the AASHTO LRFD BDS, these are classified category B using gross section stresses. The square data point in figure 53 represents the experimental data based on gross section stress, and while it is above the category B finite life line, it is below the category B CAFT and a firm conclusion cannot be drawn.

CORRELATION OF FATIGUE STRENGTH WITH HOLE SIZE

The hole *D* varied considerably among connection specimens in series C1-50. As shown in figure 16, this series had the most variation in hole *D*, with a significant number outside the

acceptable AASHTO LRFD BCS tolerance range. For the series C1-50 connection-fatigue specimens, it was noted (and reported in appendix B) whether the bolts were tight- or loose-fitting. Tight-fitting specimens had inadequate hole clearance for easily inserting bolts through holes, as illustrated in figure 56. The bolts did not slide through the holes under their own weight, and at least one bolt was not perpendicular to the plate. Bolts in series C1-50 connection-fatigue specimens had to be hammered through the holes when installing into the test machine. Figure 57 illustrates the loose-fitting condition. Here the bolts were placed into the drilled coverplate of the connection-fatigue specimens and then inserted through the holes in the plate-fatigue specimens. The holes in the connection-fatigue specimens were oversized, and the plasma-cut hole pattern did not match well to the drilled pattern of the coverplate. Tight-fitting bolts engaged prior to loose-fitting bolts, and the bearing condition among the four bolts was nonuniform. As seen in figure 58, the lower bound fatigue resistance of both the tight- and loose-fitting conditions were both between categories E and E′. The loose-fitting holes exhibited higher fatigue resistance, but lower than category E. Since the overall lower bound curve for all bearing connection specimens (figure 52) fell in between the lower bound curves for bearing connections with tight- and loose-fitting conditions (figure 58), the violation of the AASHTO LRFD BCS-specified hole tolerance was not considered a relevant parameter in determining the fatigue strength of the bearing connections.

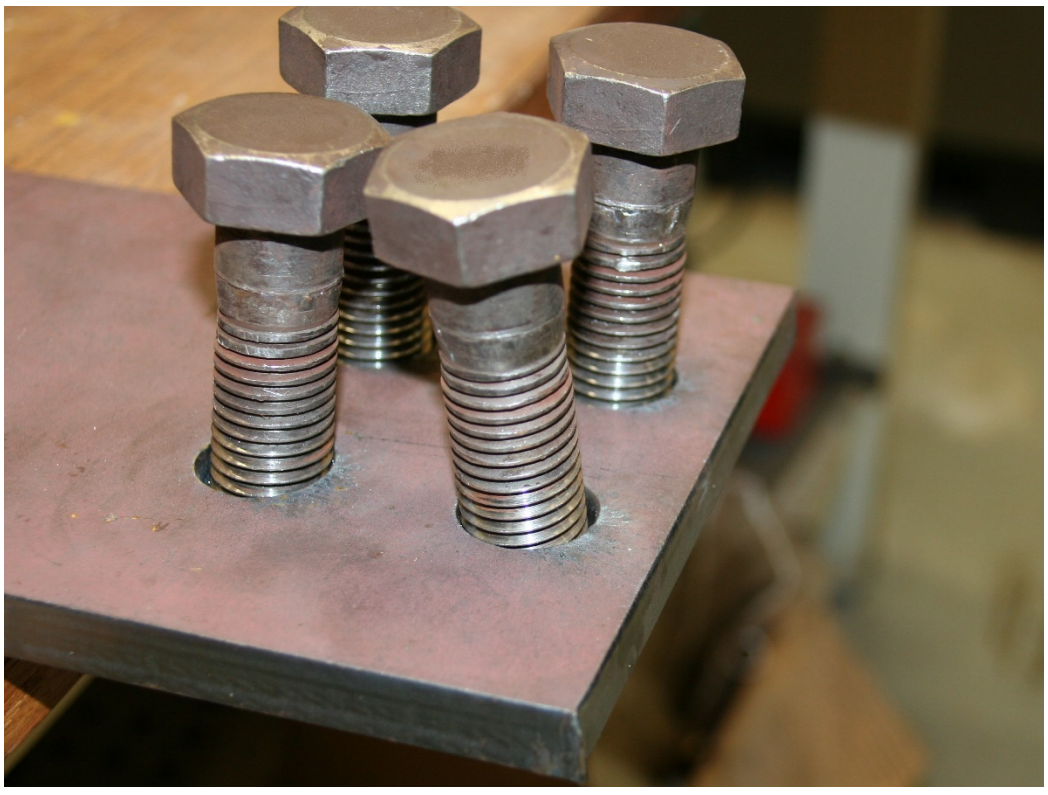

Source: FHWA.

Figure 56. Photo. Tight-fitting holes.

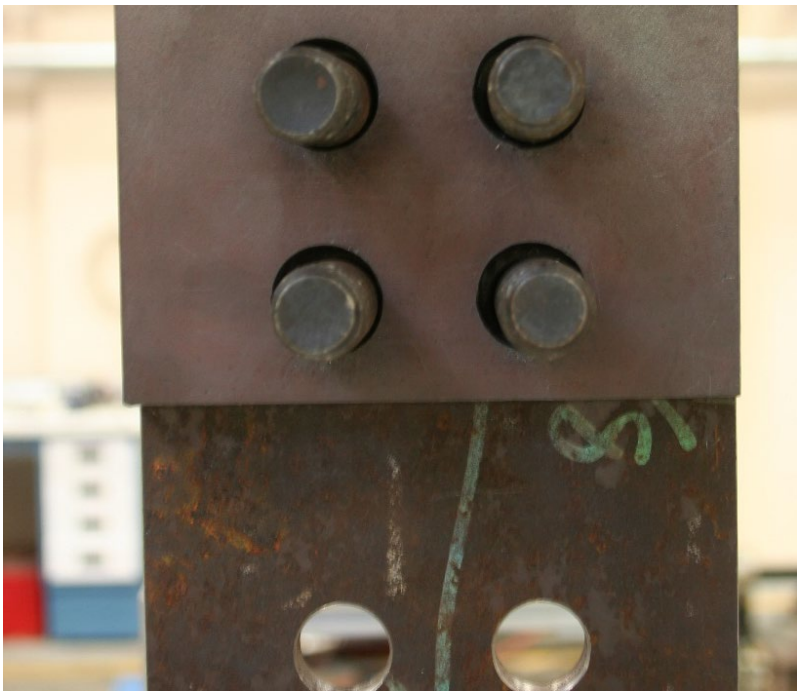

Source: FHWA.

Figure 57. Photo. Loose-fitting holes.

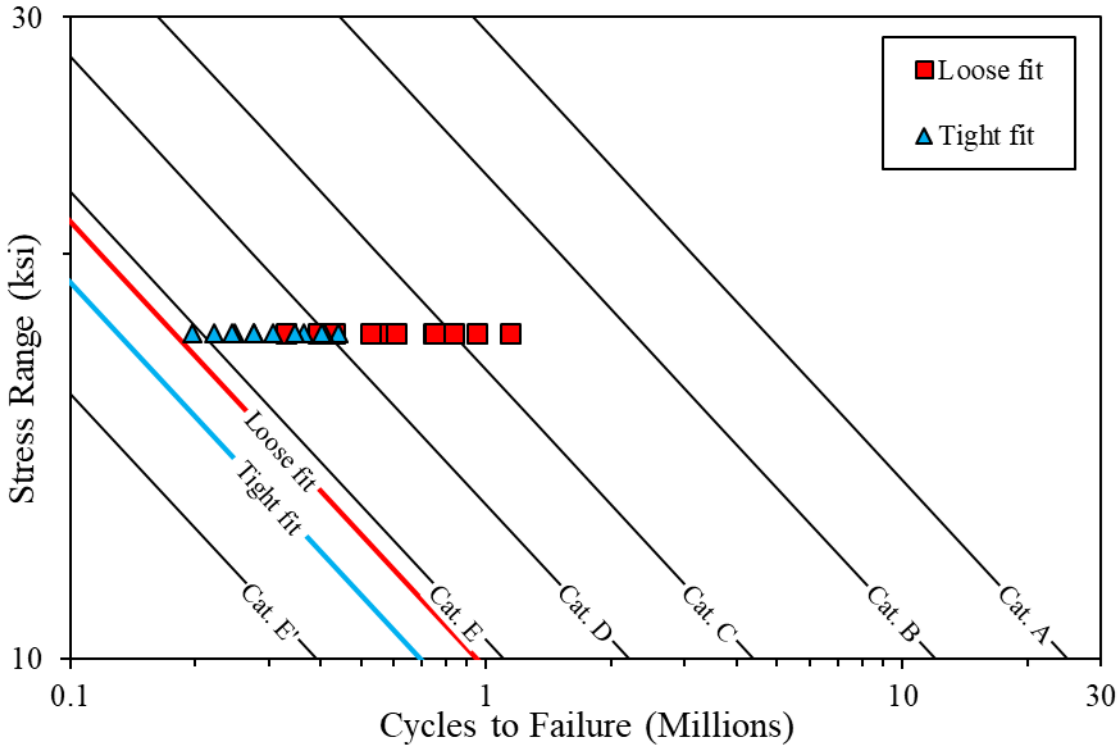

Source: FHWA.
Cat. = category.

Figure 58. Graph. S-N plot comparing effect of hole clearance.

TENSION TESTING

The tensile strength and ductility of bridge members with plasma-cut holes was determined through tension testing. Since plasma arc cutting is a thermal process, the HAZ embrittlement was a concern; therefore, this testing was conducted at low temperatures.

TEST MATRIX

All tension-test specimens shared the same geometry: a single plasma-cut hole in the middle of a 6-inch-wide, ½-inch-thick plate, as shown in figure 59. The specified hole *D* was $^{15}/_{16}$ inch.

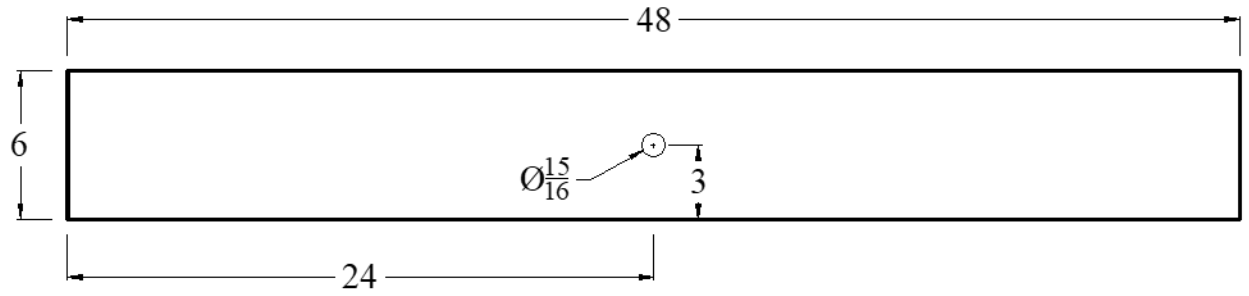

Source: FHWA.
⌀ = hole diameter.
Note: Units are in inches.

Figure 59. Schematic. Tension-test specimen geometry.

Some of the test series produced brittle fractures. It could not be determined if this was caused by the steel itself or the plasma-cutting process. There was no extra steel left at the end of the study to conduct additional tests to decouple the two variables, which led to a smaller tension-test specimen, as shown in figure 60, that was cut from tested fatigue specimens.

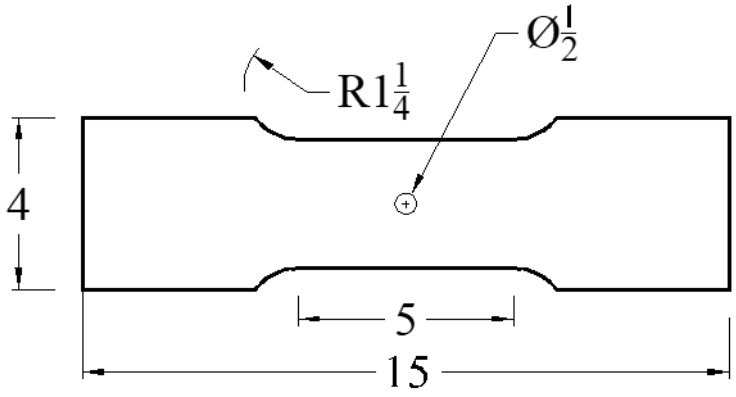

Source: FHWA.
⌀ = hole diameter.
Note: Units are in inches.

Figure 60. Schematic. Small tension-test specimen geometry.

Three variables were explored in the tension tests: specimen series (combination of plasma-cutting process, fabricator, and steel grade); test temperature; and loading rate. The concern of any embrittlement from the plasma-cutting process was driven by concerns of allowing the use of plasma arc cutting on primary and fracture critical bridge members where material impact energy requirements should prevent brittle fracture. Therefore, the test temperature and the loading rate were the variables of concern as they have the greatest effect on fracture performance.

The tension test matrix is provided in table 11. Cold temperatures were selected based on the Charpy V-notch (CVN) temperature-transition curves reported in appendix C for each specimen series. The CVN temperature-transition curves were used to identify the temperature where the steel had 25 ft-lbf of energy, and testing was performed at this temperature. This testing recreated a scenario where the steel for a bridge was delivered to just meet the minimum AASHTO LRFD BDS fracture critical energy requirements for grades 36, 50, and 50W steel.[(2)] The goal was to see if fractures of plasma-cut holes operating at this temperature would exhibit brittle or ductile behavior. Brittle behavior may indicate the plasma-cutting process should not be used on fracture critical bridge members. Room-temperature tests were carried out to show that higher temperatures would provide a ductile failure mode. These tests were conducted at the ambient temperature of the laboratory, which varied from 66 to 80 °F depending on the test.

Table 11. Tension test matrix.

Specimen Series	Testing Temperature (°F)	Temperature with Average CVN of 25 ft-lbf	Strain Rate	Number of Specimens
C1-50	−17.0	−22.5	Slow	6
			Intermediate	11[b]
	[a]	−22.5	Slow	1
			Intermediate	2
C1-50W	−4.0	−2.8	Slow	6
			Intermediate	6
	[a]	−2.8	Slow	1
			Intermediate	2
C2-36	4.0	9.5	Slow	5
			Intermediate	10[b]
	[a]	9.5	Slow	2
			Intermediate	2
E3-50W	0.0	−1.4	Slow	9
			Intermediate	9
	[a]	−1.4	Slow	3
			Intermediate	3

Specimen Series	Testing Temperature (°F)	Temperature with Average CVN of 25 ft-lbf	Strain Rate	Number of Specimens
E4-50W	−6.0	−5.0	Slow	9
			Intermediate	9
	[a]	−5.0	Slow	3
			Intermediate	3

[a]Room temperature, which was not controlled; ambient temperature in the laboratory at the time of testing varied from 66 to 80 °F.
[b]Five specimens were tested using the small tension-test specimen shown in figure 60.

The two strain rates mimicked the testing rates reported by Barsom used in developing the AASHTO CVN requirements. The intermediate strain rate was 10^{-3} per second, and the slow strain rate was around 10^{-5} per second.(16) After all testing was complete, an error was found in the curve-fitting algorithm used to define the average temperature-transition curve for the steel. This is why table 11 reports the temperature at which the test was run and the temperature where the corrected curve fit predicts an average impact energy of 25 ft-lbf. The consequence of the error is considered minor since CVN data are generally scattered, and the temperature difference was on the order of 1 °F for series C1-50W, E3-50W, and E4-50W. For series C1-50 and C2-36, the difference was 5.5 °F. The test temperature for series C1-50 yielded an impact energy of 28.8 ft-lbf, which is higher than expected. If brittle fractures occurred at this higher energy, it would be concerning. For series C2-36, the impact energy at the test temperature was 18.4 ft-lbf, which is lower than the target of 25 ft-lbf. This could influence a preference toward brittle fracture; however, it is still higher than the nonfracture-critical impact energy requirement of 15 ft-lbf.

TENSION TEST SETUP AND TESTING PROCEDURE

Tension tests were conducted in a 550-kip uniaxial test frame with a computer-controlled hydraulic actuator. Load values were measured using a load cell mounted within the test frame. The actuator displacement was monitored using an internal LVDT. The specimen elongation was measured over a 27-inch gauge length using two LVDTs mounted to each side of the specimen prior to testing. The test frame was equipped with large hydraulic grips that gripped the specimens directly. Tensile load was applied under displacement control at rates of approximately 0.10 and 2.40 inches per minute to produce the respective slow and intermediate strain rates within the 27-inch gauge length. The experimental setup is shown in figure 61 and figure 62.

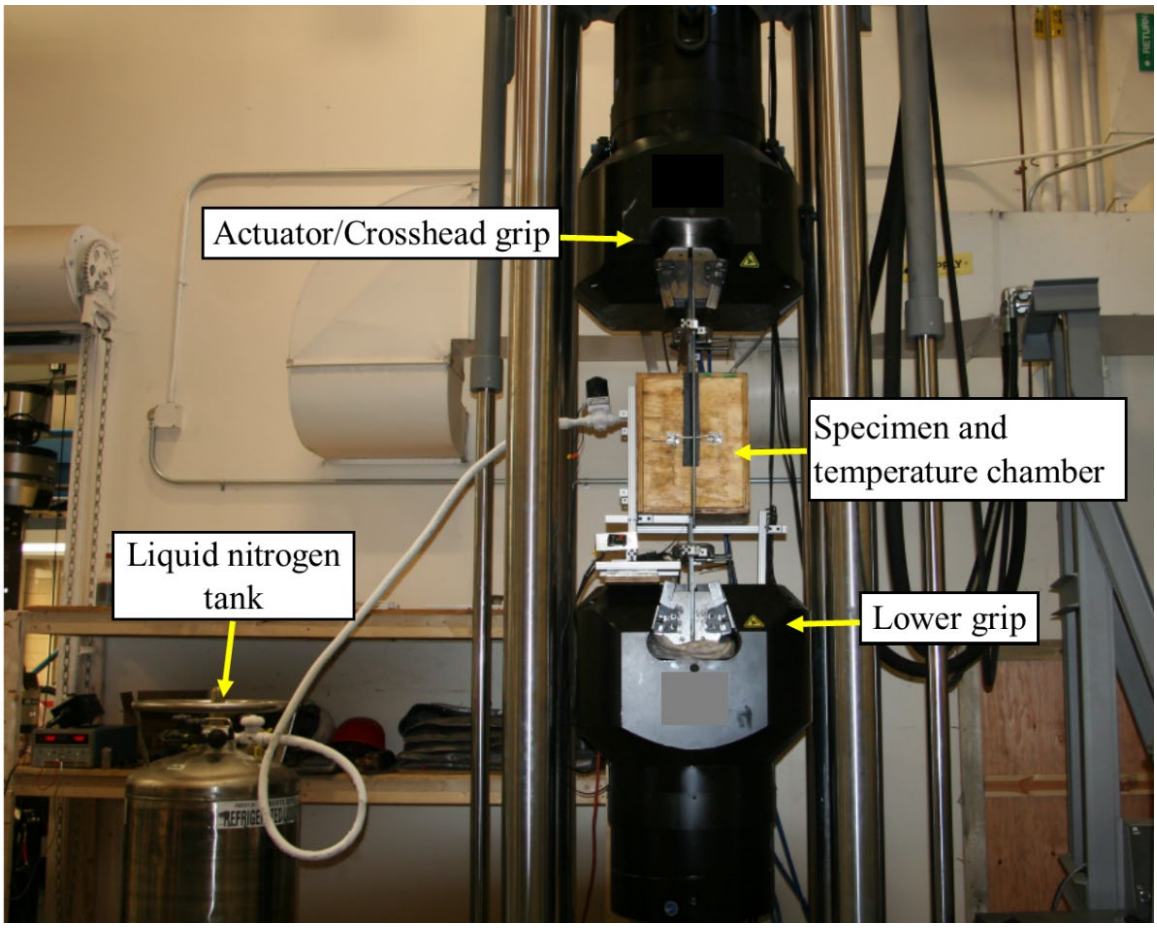

Source: FHWA.

Figure 61. Photo. Load frame setup for tension testing.

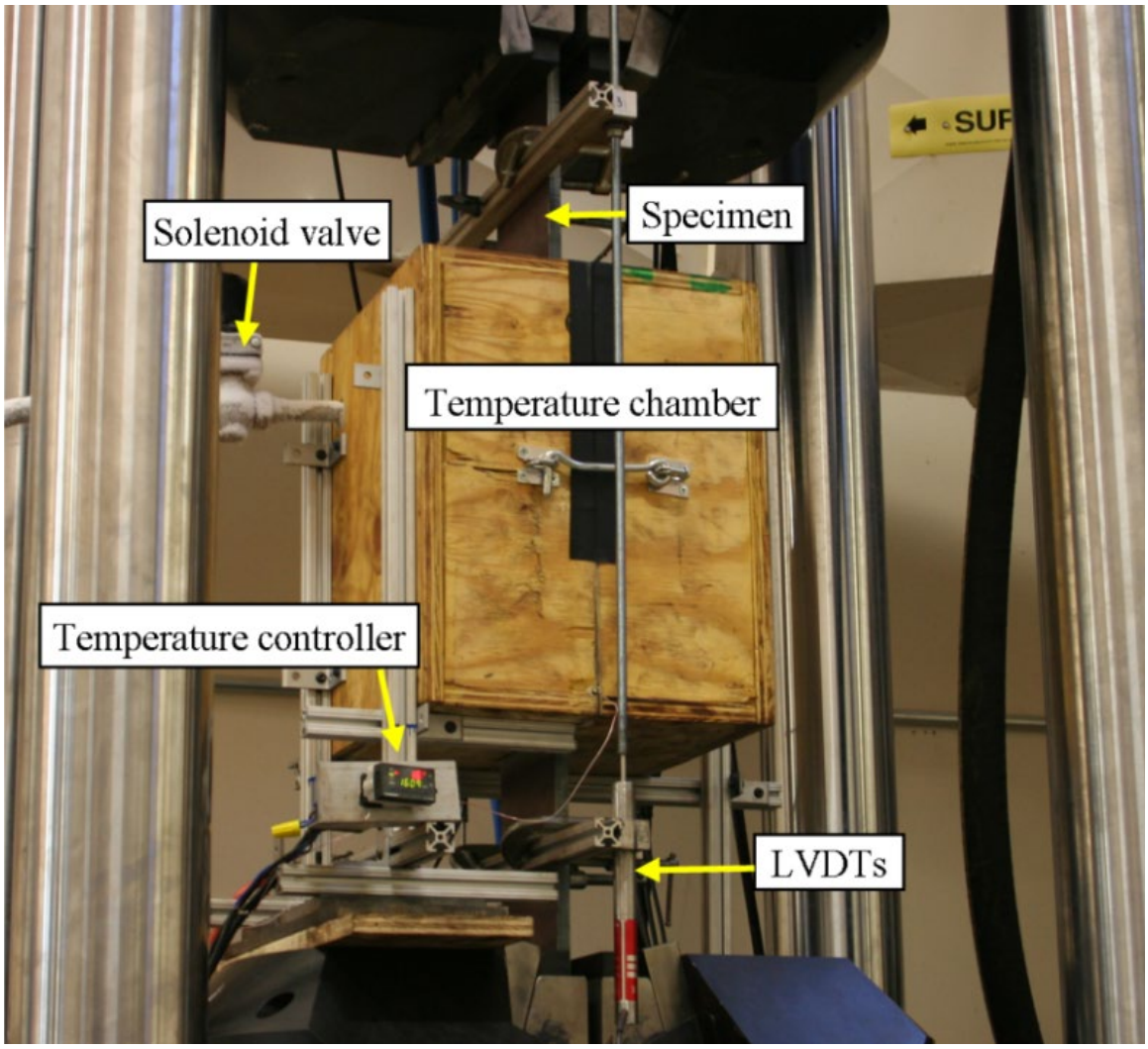

Source: FHWA.

Figure 62. Photo. Tension test setup.

During low-temperature tests, a custom temperature chamber, pictured in figure 63, was placed around the test specimen's net section. The chamber fit around approximately 6 inches on each side of the plasma-cut hole. After the temperature chamber was closed and sealed, the valve on the liquid nitrogen tank was opened, allowing liquid nitrogen to flow through a solenoid valve and into the chamber, cooling the specimen. Specimen temperature was monitored using a self-adhesive surface thermocouple placed near the net section. Output from the thermocouple-controlled flow of liquid nitrogen through the solenoid valve was regulated using a closed-loop digital temperature controller. Once the desired temperature was achieved, the temperature controller maintained the temperature of the specimen within ±1 °F. The specimen soaked for 1 h to ensure a uniform temperature through the thickness of the plate before testing.

Source: FHWA.

Figure 63. Photo. Temperature chamber.

The testing of the smaller tension-test specimens (figure 60) did not require the capacity of the 550-kip load frame. Rather, they were tension tested in frame 3 (figure 37), which had a 220-kip capacity. Because these specimens were smaller, a smaller temperature box was constructed similar in form to that in figure 62 and figure 63. Lastly, because the specimens were so short, they were completely covered by the temperature box and external LVDTs could not be used to measure elongation. For the small tension-test specimens, 5-inch-long gauge marks were placed on the specimens and before-and-after measurements were taken to determine elongation.

TENSION TEST RESULTS

Raw data from all 98 tension tests are reported in table 12 through table 17. Each table reports the specimen number (i.e., identification (ID)), testing temperature, actual strain rate, net and gross area stresses at fracture, elongation, ratio of net area stress (F_{net}) to measured tensile strength (F_u), ratio of gross area stress (F_{gross}) to measured yield strength (F_y), and the failure mode. Measured values of yield and tensile strength can be found in appendix C. Elongation was calculated as the average LVDT measurement (on the 27-inch gauge) taken at the peak load and dividing by the original gauge length. Since most fractures were by sudden brittle cleavage, this is an accurate representation of elongation. However, for the specimens failing by ductile tearing, this algorithm may underestimate total elongation and better represents the elongation when ductile tearing begins. The Failure Mode column of each table reports the failure mode as either brittle or ductile. Pictures of the tested specimens are shown in appendix D. Brittle fractures can

be identified by a cleavage fracture face that emanated from the hole out to the edge of the plate in a relatively straight path. Ductile failures propagated as angled paths either across the width of the plate or through the thickness and were also associated with significant necking in the width of the net section. Table 17 reports the results from drilled specimens—three each from fabricators E3 and E4 where the plasma-cut hole D was enlarged to $1\text{-}^{1}/_{16}$ and 1 inch, respectively, by drilling. Drilling was performed with a twist bit, effectively leaving a smooth surface finish with no HAZ or arc-termination notch.

Table 12. Tension test results for series C1-50.

Specimen ID	Testing Temperature (°F)	Actual Strain Rate (Strain/s)	F_{net} (ksi)	F_{gross} (ksi)	Elongation (Percent)	F_{net}/F_u	F_{gross}/F_y	Failure Mode	Fracture Initiate at Notch?
C1-50-1	−17	3.6E−5	74.46	62.74	3.60	1.00	1.21	Brittle	Yes
C1-50-3	−17	2.8E−5	63.29	53.37	0.33	0.85	1.03	Brittle	Yes
C1-50-5	−17	3.5E−5	75.36	63.69	3.62	1.01	1.23	Brittle	Yes
C1-50-7	−17	3.6E−5	73.57	62.15	3.38	0.99	1.20	Brittle	Yes
C1-50-9	−17	3.7E−5	74.16	62.71	3.55	0.99	1.21	Brittle	Yes
C1-50-11	−17	3.2E−5	64.99	54.85	1.45	0.87	1.06	Brittle	Yes
C1-50-2	−17	9.0E−4	76.79	64.97	3.85	1.03	1.26	Brittle	Yes
C1-50-4	−17	8.8E−4	73.08	61.46	2.96	0.98	1.19	Brittle	Yes
C1-50-6	−17	8.7E−4	72.54	61.20	2.79	0.97	1.18	Brittle	Yes
C1-50-8	−17	8.5E−4	68.84	58.06	2.09	0.92	1.12	Brittle	Yes
C1-50-10	−17	8.8E−4	78.14	65.90	4.35	1.05	1.27	Brittle	Yes
C1-50-12	−17	8.3E−4	66.67	56.24	0.49	0.89	1.09	Brittle	Yes
C1-50-13	66	4.0E−5	71.90	60.57	3.56	0.96	1.17	Ductile	Yes
C1-50-14	68	9.4E−4	72.65	61.55	3.61	0.97	1.19	Ductile	Yes
C1-50-15	68	9.5E−4	73.19	61.76	3.65	0.98	1.19	Ductile	Yes

Table 13. Tension test results for series C1-50W.

Specimen ID	Testing Temperature (°F)	Actual Strain Rate (Strain/s)	F_{net} (ksi)	F_{gross} (ksi)	Elongation (Percent)	F_{net}/F_u	F_{gross}/F_y	Failure Mode	Fracture Initiate at Notch?
C1-50W-1	−4	4.2E−5	88.06	74.76	4.68	1.03	1.25	Brittle	Yes
C1-50W-3	−4	4.4E−5	89.10	75.78	4.93	1.05	1.27	Brittle	No
C1-50W-5	−4	4.3E−5	88.02	74.90	4.97	1.03	1.25	Brittle	No
C1-50W-7	−4	4.4E−5	88.75	75.48	4.99	1.04	1.26	Brittle	Yes
C1-50W-9	−4	4.5E−5	88.28	74.88	4.69	1.04	1.25	Brittle	Yes
C1-50W-11	−4	4.5E−5	89.70	76.20	5.10	1.05	1.28	Brittle	No
C1-50W-2	−4	1.0E−3	90.27	76.68	4.50	1.06	1.28	Brittle	No
C1-50W-4	−4	1.0E−3	91.06	76.59	4.95	1.07	1.28	Ductile	No
C1-50W-6	−4	1.1E−3	90.31	76.75	4.64	1.06	1.29	Brittle	No
C1-50W-8	−4	1.0E−3	90.21	76.70	4.83	1.06	1.28	Ductile	No
C1-50W-10	−4	1.1E−3	90.46	76.77	4.82	1.06	1.29	Ductile	No
C1-50W-12	−4	1.0E−3	91.76	77.86	4.70	1.08	1.30	Ductile	Yes
C1-50W-13	70	1.1E−3	86.73	73.75	4.25	1.02	1.24	Ductile	—
C1-50W-14	74	1.1E−3	86.35	72.57	4.13	1.01	1.22	Ductile	No
C1-50W-15	74	4.4E−5	82.70	70.39	3.90	0.97	1.18	Ductile	Yes

—No data to report. Broken specimen was lost; therefore, notch location could not be identified.

Table 14. Tension test results for series C2-36.

Specimen ID	Testing Temperature (°F)	Actual Strain Rate (Strain/s)	F_{net} (ksi)	F_{gross} (ksi)	Elongation (Percent)	F_{net}/F_u	F_{gross}/F_y	Failure Mode	Fracture Initiate at Notch?
C2-36-1	—	—	—	—	—	—	—	—	—
C2-36-2	4	4.0E−5	74.10	62.09	1.12	1.01	1.35	Brittle	Yes
C2-36-3	4	3.8E−5	75.94	63.65	1.26	1.04	1.38	Brittle	Yes
C2-36-10	4	3.3E−5	74.34	62.41	0.89	1.02	1.36	Brittle	Yes
C2-36-12	4	4.0E−5	76.55	64.32	1.63	1.05	1.40	Brittle	Yes
C2-36-14	4	3.8E−5	74.02	62.27	1.33	1.01	1.35	Brittle	Yes
C2-36-4	4	9.2E−4	78.40	65.73	1.89	1.07	1.43	Brittle	Yes
C2-36-5	4	9.5E−4	76.57	64.30	1.25	1.05	1.40	Brittle	Yes
C2-36-6	4	1.1E−3	82.31	69.00	2.95	1.12	1.50	Ductile	Yes
C2-36-13	4	1.0E−3	79.69	67.02	2.45	1.09	1.46	Brittle	Yes
C2-36-15	4	7.9E−4	73.94	62.06	0.77	1.01	1.35	Brittle	Yes
C2-36-8	80	3.9E−5	73.95	62.22	1.66	1.01	1.35	Ductile	No
C2-36-11	68	4.1E−5	75.04	62.96	1.62	1.03	1.37	Ductile	Yes
C2-36-7	80	9.9E−4	75.77	63.71	1.71	1.04	1.38	Ductile	Yes
C2-36-9	78	1.0E−3	74.98	63.00	1.94	1.02	1.37	Ductile	Yes

—No data to report. There was a hole pattern in the gripped region that suffered from a net section fracture that prevented further loading of the specimen.

Table 15. Tension test results for series E3-50W.

Specimen ID	Testing Temperature (°F)	Actual Strain Rate (Strain/s)	F_{net} (ksi)	F_{gross} (ksi)	Elongation (Percent)	F_{net}/F_u	F_{gross}/F_y	Failure Mode	Fracture Initiate at Notch?
E3-0-3	0	5.0E−05	84.80	71.34	3.58	1.00	1.24	Brittle	Yes
E3-0-4	0	4.9E−05	86.56	72.83	4.03	1.02	1.26	Brittle	Yes
E3-0-5	0	4.9E−05	86.91	73.13	3.98	1.02	1.27	Brittle	Yes
E3-45-3	0	3.7E−05	88.92	75.09	4.66	1.05	1.30	Brittle	No
E3-45-4	0	3.2E−05	90.30	75.82	4.42	1.06	1.31	Brittle	No
E3-45-5	0	3.3E−05	88.36	74.09	4.61	1.04	1.28	Brittle	No
E3-90-3	0	4.0E−05	88.77	74.90	4.25	1.05	1.30	Brittle	No
E3-90-4	0	3.4E−05	90.33	76.62	4.74	1.07	1.33	Brittle	No
E3-90-5	0	3.2E−05	89.51	75.16	4.63	1.06	1.30	Brittle	No
E3-0-6	0	1.1E−03	89.55	75.32	4.20	1.06	1.31	Brittle	Yes
E3-0-7	0	1.1E−03	89.92	75.56	4.31	1.06	1.31	Ductile	Yes
E3-0-8	0	1.1E−03	88.65	74.59	4.16	1.05	1.29	Brittle	Yes
E3-45-6	0	1.1E−03	90.39	76.20	4.21	1.07	1.32	Brittle	No
E3-45-7	0	1.1E−03	90.17	76.08	4.36	1.06	1.32	Brittle	No
E3-45-8	0	1.1E−03	90.35	76.29	4.14	1.07	1.32	Brittle	No
E3-90-6	0	1.0E−03	91.83	77.25	4.53	1.08	1.34	Brittle	No
E3-90-7	0	1.1E−03	91.70	77.64	4.80	1.08	1.35	Brittle	No
E3-90-8	0	1.2E−03	92.38	77.71	5.36	1.09	1.35	Brittle	No
E3-0-1	74	1.2E−03	84.97	71.68	3.54	1.00	1.24	Ductile	Yes
E3-45-1	78	1.1E−03	84.55	71.42	3.94	1.00	1.24	Ductile	No
E3-90-1	74	1.2E−03	87.96	74.20	4.26	1.04	1.29	Ductile	No

Specimen ID	Testing Temperature (°F)	Actual Strain Rate (Strain/s)	F_{net} (ksi)	F_{gross} (ksi)	Elongation (Percent)	F_{net}/F_u	F_{gross}/F_y	Failure Mode	Fracture Initiate at Notch?
E3-0-2	74	4.6E−05	82.80	69.81	3.46	0.98	1.21	Brittle	Yes
E3-45-2	78	5.0E−05	83.20	70.18	3.64	0.98	1.22	Ductile	No
E3-90-2	74	5.1E−05	84.23	70.92	3.97	0.99	1.23	Ductile	No

Table 16. Tension test results for series E4-50W.

Specimen ID	Testing Temperature (°F)	Actual Strain Rate (Strain/s)	F_{net} (ksi)	F_{gross} (ksi)	Elongation (Percent)	F_{net}/F_u	F_{gross}/F_y	Failure Mode	Fracture Initiate at Notch?
E4-0-3	−6	4.2E−05	83.21	69.96	3.99	1.07	1.21	Brittle	Yes
E4-0-4	−6	4.1E−05	82.05	69.10	3.70	1.06	1.19	Brittle	Yes
E4-0-5	−6	4.6E−05	81.44	68.50	3.94	1.05	1.18	Brittle	Yes
E4-45-3	−6	4.1E−05	82.42	69.36	4.02	1.06	1.20	Brittle	No
E4-45-4	−6	5.0E−05	82.53	69.39	4.16	1.06	1.20	Brittle	No
E4-45-5	−6	5.0E−05	81.94	68.93	3.94	1.06	1.19	Brittle	No
E4-90-3	−6	4.3E−05	83.66	70.42	4.11	1.08	1.22	Brittle	No
E4-90-4	−6	5.1E−05	82.15	69.11	4.26	1.06	1.19	Brittle	No
E4-90-5	−6	4.5E−05	82.00	68.89	4.14	1.06	1.19	Brittle	No
E4-0-6	−6	1.2E−03[a]	82.91	69.76	4.04[a]	1.07	1.20	Brittle	Yes
E4-0-7	−6	1.2E−03	83.89	70.59	4.21	1.08	1.22	Ductile	Yes
E4-0-8	−6	1.2E−03	82.64	69.44	3.73	1.07	1.20	Ductile	Yes
E4-45-6	−6	1.2E−03	83.57	70.32	4.37	1.08	1.21	Ductile	No
E4-45-7	−6	1.2E−03	84.15	70.69	4.31	1.09	1.22	Ductile	No
E4-45-8	−6	1.2E−03	84.57	71.16	4.32	1.09	1.23	Ductile	No
E4-90-6	−6	1.2E−03	84.09	70.71	4.32	1.08	1.22	Ductile	No
E4-90-7	−6	1.2E−03	84.07	70.78	4.51	1.08	1.22	Ductile	No
E4-90-8	−6	1.2E−03	84.02	70.71	4.42	1.08	1.22	Ductile	No
E4-0-1	70	1.1E−03	77.76	65.48	3.32	1.00	1.13	Ductile	Yes
E4-45-1	70	1.1E−03	80.55	67.77	3.46	1.04	1.17	Ductile	No
E4-90-1	68	1.2E−03	78.43	65.99	3.38	1.01	1.14	Ductile	No

Specimen ID	Testing Temperature (°F)	Actual Strain Rate (Strain/s)	F_{net} (ksi)	F_{gross} (ksi)	Elongation (Percent)	F_{net}/F_u	F_{gross}/F_y	Failure Mode	Fracture Initiate at Notch?
E4-0-2	70	5.3E−05	75.51	63.59	3.03	0.97	1.10	Ductile	Yes
E4-45-2	70	5.1E−05	77.26	65.02	3.21	1.00	1.12	Ductile	No
E4-90-2	68	5.1E−05	77.59	65.32	3.18	1.00	1.13	Ductile	No

[a]LVDT data failed to record. Data reported are based on the LVDT internal to the actuator minus the average machine compliance measured in all other specimens.

Table 17. Tension test results for drilled specimens.

Specimen ID	Testing Temperature (°F)	Actual Strain Rate (Strain/s)	F_{net} (ksi)	F_{gross} (ksi)	Elongation (Percent)	F_{net}/F_u	F_{gross}/F_y	Failure Mode
E3-d1	0	3.5E−5	89.14	73.37	4.88	1.05	1.27	Ductile
E3-d2	0	3.4E−5	89.05	73.32	4.65	1.05	1.27	Ductile
E3-d3	0	1.1E−3	92.49	76.31	4.54	1.09	1.32	Ductile
E4-d1	−6	3.3E−5	82.01	68.37	3.92	1.06	1.18	Brittle
E4-d2	−6	3.3E−5	82.06	68.46	4.20	1.06	1.18	Brittle
E4-d3	−6	2.3E−3	83.74	69.89	4.34	1.08	1.21	Ductile
C1-50-5c	−17	3.1E−4	79.47	52.98	7.86	1.07	1.02	Ductile
C1-50-7c	−17	3.1E−4	78.54	51.91	7.78	1.05	1.00	Ductile
C1-50-18c	−17	3.1E−4	81.36	53.75	7.50	1.09	1.04	Ductile
C1-50-20c	−17	3.1E−4	78.51	51.84	7.81	1.05	1.00	Ductile
C1-50-21c	−17	3.1E−4	80.94	53.49	9.70	1.08	1.03	Ductile
C2-36-04c	−4	3.1E−4	75.38	50.50	5.27	1.03	1.10	Brittle
C2-36-22c	−4	3.1E−4	80.04	53.57	5.34	1.09	1.16	Ductile
C2-36-23c	−4	3.1E−4	77.60	52.08	7.79	1.06	1.13	Ductile
C2-36-27c	−4	3.1E−4	78.48	52.57	8.57	1.07	1.14	Ductile
C2-36-29c	−4	3.1E−4	77.92	52.09	7.71	1.06	1.13	Ductile

Several trends can be identified by inspecting the data in table 12 through table 17. First, all specimens demonstrated yield ratios greater than 1.0, indicating that every specimen could develop the theoretical yield strength across the gross section. However, not all specimens could attain the theoretical fracture strength on the net section. Second, all room-temperature tests resulted in ductile failures, which is not surprising considering all the steels tested were well into transition or upper-shelf CVN impact energy at this temperature. The low-temperature tests were conducted at temperatures meant to replicate AASHTO LRFD BDS minimum impact energy for fracture-critical applications. These tests resulted in a blend of brittle and ductile fractures depending on the series and loading rate.

Table 18 presents the data from the 86 low-temperature tests in terms of the specimen series and strain rate and the associated statistics of fracture ratio and elongation. The strain rate did not have an obvious effect on the results, as the average fracture ratio and average elongation were generally within one standard deviation of each other at both loading rates. Series C1-50 could not attain average fracture ratios greater than 1.0, indicating unconservative performance. Also, the average elongation values for series C1-50 and C2-36 are lower and have considerably more scatter than the remaining series. This is shown in figure 64, which plots the fracture ratio versus elongation for each specimen. Figure 64 shows the wide variety of elongations in series C1-50 and C2-36, but the remaining series are more closely clustered together. Series C1-50 and C2-36 both used conventional plasma-cutting processes and exhibited the worst static testing results. However, one of the better performing series was C1-50W, which used a conventional plasma-cutting process of a weathering steel grade, leading to the conclusion the propensity of poor tension behavior was more likely due the to the steel than the cutting process. This confluence of material and cutting process variables was the genesis of the smaller tension test samples (figure 60) with drilled holes from series C1-50 and C2-36 fatigue specimens.

Table 18. Low-temperature tension testing results.

Specimen Series	Strain Rate	Average F_{net}/F_u	COV of F_{net}/F_u	Average Percent Elongation	COV of Elongation
C1-50	Slow	0.95	0.075	2.65	0.533
C1-50	Intermediate	0.97	0.061	2.75	0.496
C1-50-drilled[a]	Intermediate	1.07	0.017	8.13	0.109
C1-50W	Slow	1.04	0.007	4.90	0.033
C1-50W	Intermediate	1.07	0.008	4.74	0.034
C2-36	Slow	1.02	0.016	1.25	0.220
C2-36	Intermediate	1.07	0.040	1.86	0.474
C2-36-drilled[a]	Intermediate	1.06	0.020	6.94	0.220
E3-50W	Slow	1.04	0.021	4.32	0.091
E3-50W	Intermediate	1.07	0.013	4.45	0.090
E3-50W-drilled	Slow	1.05	[b]	4.77	[b]
E3-50W-drilled	Intermediate	1.09[c]	[c]	4.54[c]	[c]
E4-50W	Slow	1.06	0.008	4.02	0.040
E4-50W	Intermediate	1.08	0.007	4.25	0.055
E4-50W-drilled	Slow	1.06	[b]	4.06	[b]
E4-50W-drilled	Intermediate	1.08[c]	[c]	4.34[c]	[c]

[a]Small tension-test specimen as shown in figure 60.
[b]Only two specimens, so COV could not be calculated.
[c]Only one specimen, therefore average is result of one test, and COV could not be calculated.

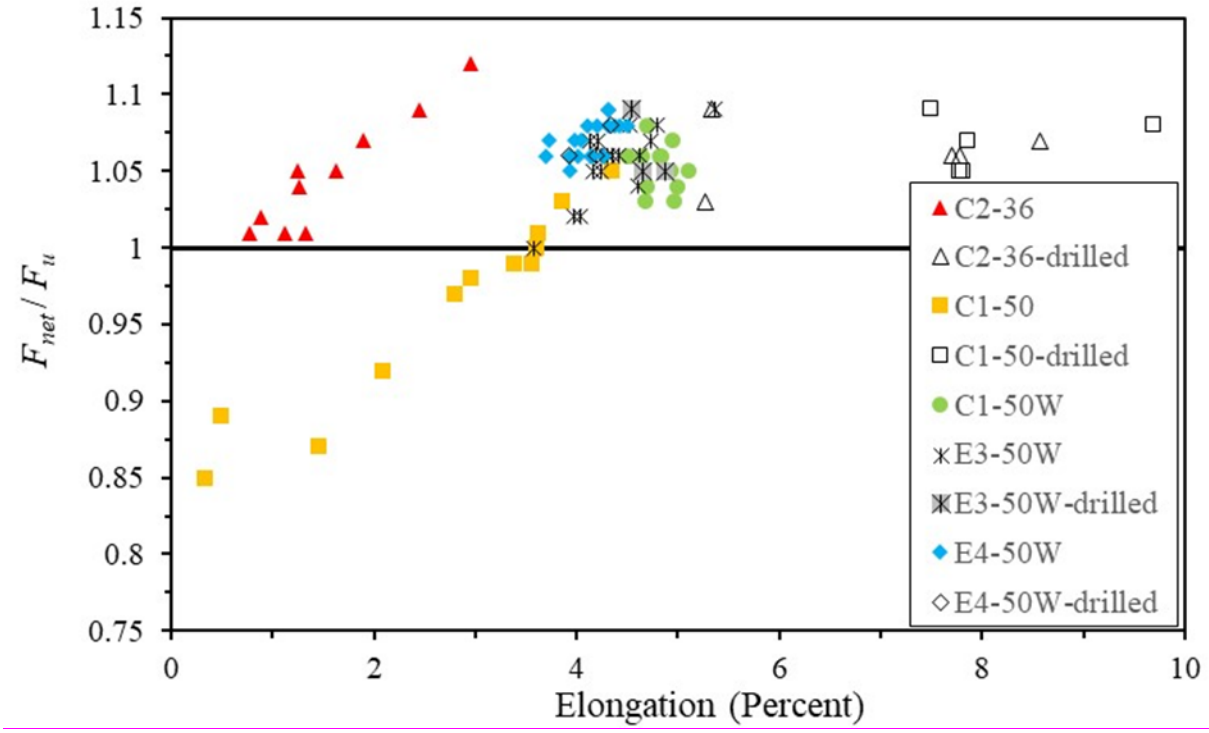

Source: FHWA.

Figure 64. Graph. Fracture ratio versus elongation of low-temperature specimens.

Influence of Cutting Process

The drilled specimens represent the ideal scenario by which to compare a plasma-cut hole as any deleterious effects from the HAZ and imperfect hole geometry were eliminated. The results of drilled holes require careful analysis because there were two different specimen sizes, which greatly influence the elongation results. The drilled specimens for series E3-50W and E4-50W had elongation measured over a 27-inch length (or 28.8*D*), whereas the drilled specimens for series C1-50 and C2-36 had elongation measured over 5.5 inches (or 11*D*). In these types of tests, plasticity is localized around the hole, and this region contributes to the overall elongation. Therefore, elongations decrease as the gauge length over which they are measured increases. Because of this, elongations for smaller specimens appear much larger. However, there was no choice in the manner; the smaller specimen size for series C1-50 and C2-36 drilled tension specimens were dictated by the available material. This size effect is the reason for the high elongations measured for the drilled series C1-50 and C2-36 specimens as seen in figure 64, table 17, and table 18.

The results shown in figure 64 demonstrate that drilled hole data for series E3-50W and E4-50W fall into the cluster of data from series E3-50W and E4-50W with enhanced plasma-cut holes. This is an indicator that enhanced HD plasma-cut holes do not influence the static performance of net sections, though there was a slight increase in elongation with the drilled holes. The fracture faces from specimen E3-0-3 (plasma arc cut) and E3-d1 (drilled) are shown in figure 65 and figure 66, respectively. The fracture face for the plasma-cut hole specimen mostly manifested as cleavage with little reduction in thickness and ductile tearing around the hole,

whereas the fracture face of the specimen with the drilled hole showed significant evidence of ductile tearing near the hole (i.e., section reduction and inclined fracture plane through the thickness) followed by the brittle fracture.

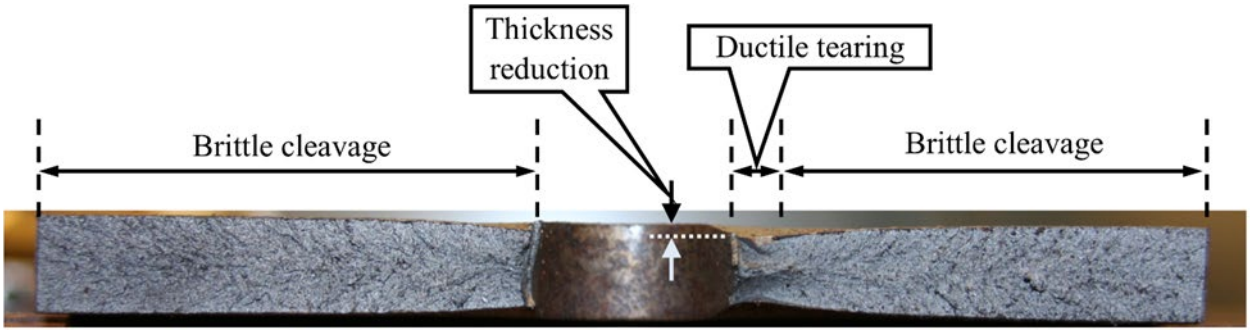

Source: FHWA.

Figure 65. Photo. Fracture face of specimen E3-0-3.

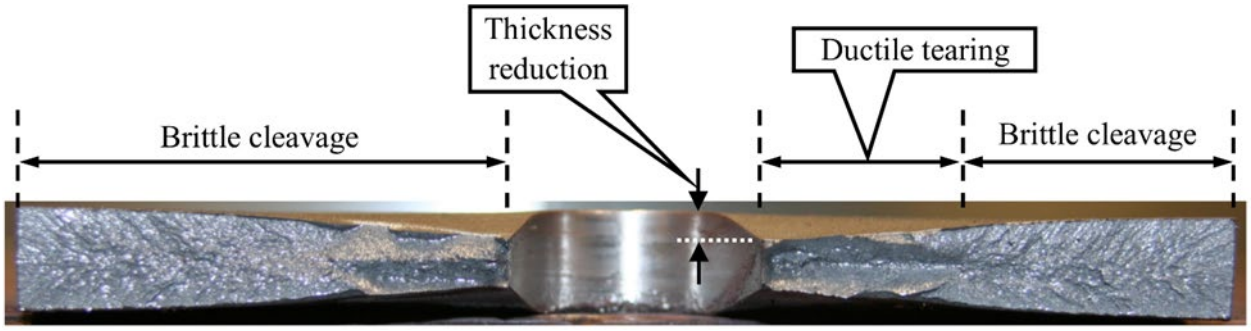

Source: FHWA.

Figure 66. Photo. Fracture face of drilled specimen E3-d1.

The results shown in figure 64 for series C1-50 show unacceptable results for conventional plasma-cut holes with low elongations and numerous fracture ratios less than 1.0. However, the same steel with a drilled hole showed a clustering of data with fracture ratios greater than 1.0 with good elongation results. With the caveat of the size effect on the elongation values for the drilled hole specimens, those elongation data are clustered, indicating that the subpar behavior of the conventional plasma-cut holes was related to the plasma-cutting process itself.

The results shown in figure 64 for series C2-36 with conventional plasma-cut holes show acceptable fracture ratios but poor elongation relative to the remainder of the results from other steels. The drilled specimens made from this steel also had acceptable fracture ratios but varied elongation results ranging from 5.27 to 8.57 percent. The range of elongation values was wider in the drilled specimen versus the conventional-plasma-cut specimen, which is an indicator that the poor performance of this series was related to the steel itself.

Although it was only explored for grade 50W steel, the tension data indicate that the use of enhanced HD plasma for tension members is acceptable since the results between plasma-cut holes and drilled holes do not vary much. However, at least one of the conventional plasma-cut

hole series (C1-50) was proven to produce deleterious tension results indicating that conventional plasma should not be allowed for use in tension members.

Influence of Arc-Termination Notch

Table 12 through table 16 note whether the fracture initiated at the arc-termination notch. Every specimen of series C1-50 and C2-36 had the fracture initiate at the arc-termination notch. However, this was not always the case with the remaining series. Table 19 reports the average fracture ratio of low-temperature specimens from each series grouped by the orientation of the arc-termination notch. At best, there does not appear to be a trend regarding the orientation of the arc-termination notch. The notable exception is series C1-50 with fracture ratios less than 1.0. However, it cannot be parsed from the data if this was from the particular heat of steel, the plasma-cutting process, or the arc-termination notch. Since series C1-50 was fabricated by the same machine as series C1-50W, the reduction cannot be attributed to the plasma-cutting process. The series C1-50 post-test pictures in appendix E show that the specimens completely fractured through two events: the brittle cleavage through half the plate originating at the arc-termination notch, followed by either a brittle or ductile facture on the other side of the plate. Figure 67 shows the C1-50-11 specimen with an annotation showing additional elongation around the hole before the second fracture event. It was typical for the 12 low-temperature specimens that the remaining ligament after the initial fracture had additional ductility, ruling out that overall reduced ductility of the specimen was related to the steel. The cut plans provided by fabricator C1 show the applied tension load in the static test coincide with the plate direction of roll, so it was also ruled out as a possibility for the poor performance. Therefore, at least for series C1-50, the unfavorable fracture ratios and elongations are wholly attributable to the arc-termination notch.

Table 19. Average fracture ratios of low-temperature specimens grouped according to position of arc-termination notch.

Specimen Series	Arc-Termination Notch at 0 Degrees	Arc-Termination Notch at 45 Degrees	Arc-Termination Notch at 90 Degrees
C1-50	0.96	—	—
C1-50W	—	1.05	—
C2-36	1.05	—	—
E3-50W	1.03	1.06	1.07
E4-50W	1.07	1.07	1.08

—No specimens tested.

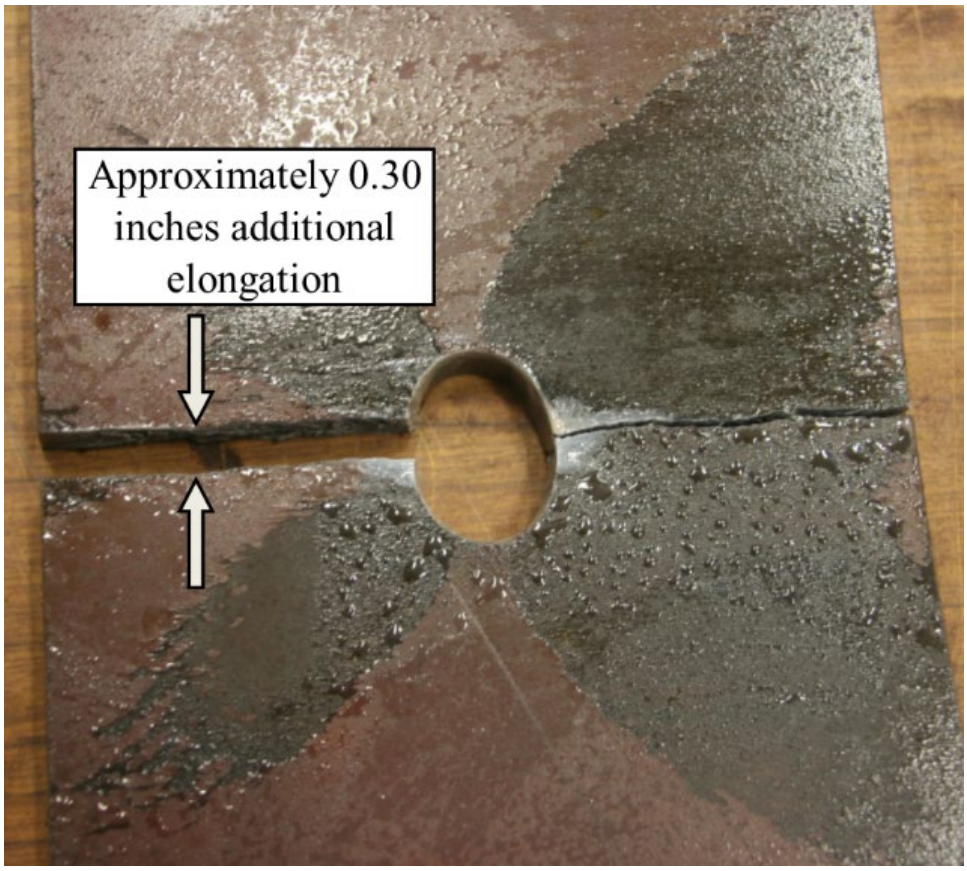

Source: FHWA.

Figure 67. Photo. Additional elongation until second fracture in specimen C1-50-11.

CONCLUSIONS

This study investigated the fatigue and tensile performance of plasma-cut holes in steel bridge members. Four different fabricators provided fatigue and tension specimens with plasma-cut holes manufactured in grade 36, 50, and 50W steel plates. Each fabricator produced round holes using different plasma-cutting equipment and techniques, referred throughout this report as conventional or enhanced HD technology.

Hole quality was characterized using measurements of geometric properties and visual inspections. A major concern was whether the plasma-cut holes could meet fabrication tolerances specified in the AASHTO LRFD BCS.[1] Another key interest was comparing the quality of plasma arc cutting offered by each fabricator. Specifically, conventional plasma arc cutting was compared to newer, enhanced HD plasma arc cutting techniques.

Fatigue data were collected for plates with a single open hole and connections having both pretensioned and nonpretensioned bolts. Fatigue resistance was characterized using S-N data and regression analysis to classify plasma-cut holes to the AASHTO LRFD BDS fatigue categories. Ultimate strength and fracture behavior were examined through tension testing at low and room temperatures. Fracture behavior at low temperatures provided insight on the fitness of plasma-cut holes in primary members. The variables of concern throughout fatigue and tension testing included steel grade, plasma arc cutting process, and the location of an arc-termination notch common in plasma-cut holes.

Conclusions drawn from this research are reported in the following sections.

HOLE QUALITY

Conclusions regarding hole quality include the following:

- Visual inspection found that plasma-cut holes provided by fabricators using conventional plasma arc cutting were far more out-of-round than those cut using enhanced HD plasma.
- Several holes fabricated using conventional plasma arc cutting showed some amount of dross adhered to the cut surface. The presence of this material, in tandem with being under *D*, prevented bolts from passing through the holes. This issue was not encountered with the enhanced HD plasma-cut holes.
- The depth of the arc-termination notch was significantly reduced or eliminated on holes fabricated using enhanced HD plasma arc cutting.
- The variability provided by conventional plasma-cut holes was too far out of range to ever be used in bridge fabrication. Enhanced HD plasma-cut holes can be produced within sufficient tolerance to work in bridge fabrication, though the bridge-construction industry would have to accept a larger *D* tolerance than currently allowed. Enhanced HD plasma-cut holes can work within a $^{1}/_{16}$-inch-hole-diameter tolerance but cannot reliably meet the current $^{1}/_{32}$-inch tolerance in the AASHTO LRFD BCS.

FATIGUE TESTING

Conclusions regarding fatigue testing include the following:

- All fatigue test data were analyzed in terms of steel grade, fabricator, and location of the arc-termination notch. The lower bound fatigue resistance from the data was estimated for all analyses to consistently compare to the existing AASHTO LRFD BDS design fatigue categories.
- For open holes, there were slight differences in fatigue strength between steel grade, fabricator, and location of the arc-termination notch. Since there was little difference, it made sense to consider all the data collected (both conventional and enhanced HD plasma) to determine the lower bound resistance, which was between categories D and E. Therefore, open plasma-cut holes must be classified as category E fatigue details. Currently, open holes are category D fatigue details, and this represents a one category reduction in design life.
- The category E classification of open holes may appear punitive against fabricator E4 because the holes produced by this fabricator fulfill category D design requirements. However, from the standpoint of writing a specification, there was not enough data collected in this study to determine what process variables between fabricators E3 and E4 caused the difference. Thus, they must be treated one in the same.
- For connection specimens with nonpretensioned bolts, there was a marked difference in fatigue strength relative to the orientation of the arc-termination notch. The lowest fatigue resistance was produced when the notch was at 0 degrees, which was expected. However, inspecting the notch location for every hole in a hole pattern is a major imposition, and it is not justifiable to recommend a higher resistance considering a more favorable notch location. Once the notch location was eliminated, little difference existed between conventional and enhanced HD plasma-cutting processes. The lower bound resistance for both conventional and enhanced HD plasma was below category E, and these must be classified as category E′. Currently, holes in nonpretensioned connections are category D fatigue details, and this represents a two-category reduction in design life.
- Four specimens tested with pretensioned bolts were declared runout specimens at 10 million cycles at a 12.0-ksi stress range. This represents a finite fatigue life greater than category B; however, the stress range is less than the category B CAFT. The compressive stresses induced around the hole from the bolt pretension may improve the fatigue resistance of plasma-cut holes.

TENSION TESTING

Conclusions regarding tension testing include the following:

- Conventional plasma-cut holes in grade 50 steel could not achieve the tensile strength on the net section and thus is unsafe for bridge connections. Premature fracture mostly initiated at the arc-termination notch.
- Conventional plasma-cut open holes in grade 36 steel produced favorable fracture ratios. However, elongations were much lower than that of drilled holes and this is not recommended for use in bridge connections.

- The enhanced HD plasma-cutting process produced favorable fracture ratios and elongations, which were commensurate with drilled holes; it would be allowable for use in bridge connections.
- The most favorable fracture ratios and elongations were produced by specimens with conventional plasma-cut holes in grade 50W steel. They were commensurate with drilled holes and would be allowable for use in bridge connections.
- The orientation of the arc-termination notch was not considered relevant to the tensile resistance of specimens except for conventional plasma-cut holes in grade 50 steel.
- The study did not explore a full factorial matrix of tensile tests considering process, fabricator, and steel grade. The best results were attained with grade 50W steel, but it is unclear why grades 36 and 50 performed so poorly and whether this was related to heat input or steel chemistry. Until this is better understood, plasma arc cutting should not be allowed on fracture-critical and primary tension members made from grades other than 50W.
- Drilling the D of plasma-cut holes approximately $^{1}/_{16}$ inch larger removed any deleterious effect of imperfect hole geometry and HAZ. This tended to increase the ductility of the hole, though this was only explored in grade 50W steel with enhanced HD plasma arc cutting.

FUTURE WORK

Although steel bridge construction relies mostly on slip-critical bolted connections with pretensioned bolts, this research emphasized testing open holes. Only four connection specimens were tested with pretensioned bolts, and though the results were positive, they were inconclusive regarding the protective benefit of bolt pretension on the fatigue and fracture performance of plasma-cut holes. Therefore, further research is recommended in the following areas:

- The fatigue resistance of plasma-cut hole connections with pretensioned bolts. This study demonstrated that the fatigue strength of plasma-cut holes is not sensitive to steel grade or the fabricator, though the arc-termination notch could be a factor. The testing matrix of the recommended study should be performed on slip-critical and bearing-type connections with pretensioned bolts with notches oriented at the least favorable position. The recommended study should only focus on enhanced HD plasma-cutting technologies.
- The wide variation of fracture resistance relative to material grade. The recommended study should focus on the open hole testing conducted in the present study but also explore whether bolt pretension is beneficial. The recommended study should only focus on enhanced HD plasma-cutting technologies.

RECOMMENDATIONS

The following recommendations are proposed regarding the potential inclusion of plasma-cut holes as an acceptable hole-making method in the AASHTO LRFD BDS and the AASHTO LRFD BCS:[1,2]

- Prohibit the use of full-size conventional plasma-cut holes in the fabrication of hole patterns for bolted connections. This process cannot make holes or hole patterns to the expected requirements historically produced by other hole-making methods.
- Limit the use enhanced HD plasma-cut holes in primary tension and fracture-critical members to grade 50W steel.
- Allow reamed, subsized plasma-cut holes with either conventional or enhanced HD plasma.
- Apply a reduction factor equal to 0.90 for plasma-cut holes to account for the notion that hole *D* are typically larger than the standard $^{1}/_{16}$-inch hole oversize.
- Include open holes fabricated in steel bridge members using plasma arc cutting as a category E fatigue detail.
- Include plasma-cut holes in bearing connections with nonpretensioned bolts as a category E′ fatigue detail.

APPENDIX A. DIMENSIONAL MEASUREMENTS

Table 20 through table 25 contain the raw data from high-accuracy laser measurements collected during this study. The specified hole *D* and maximum allowable hole *D* per the AASHTO LRFD BCS are provided for comparison purposes when necessary.[1] Geometric standards for e_h, C_h, and α are not codified and cannot be compared to published specifications.

Table 20. Dimensional measurements for series C1-50.

Hole	*D* Face 1 (Inch)[a,b]	*D* Face 2 (Inch)[a,b]	e_h Face 1	e_h Face 2	C_h Face 1 (Inch)	C_h Face 2 (Inch)	α (Degree)
C1-50 2-1	1.054	1.027	0.261	0.340	0.024	0.047	1.55
C1-50 2-2	1.052	1.013	0.244	0.352	0.020	0.039	2.23
C1-50 2-3	1.051	1.025	0.281	0.361	0.030	0.050	1.49
C1-50 2-4	1.048	1.016	0.274	0.351	0.027	0.044	1.83
C1-50 3-1	1.052	1.015	0.258	0.349	0.022	0.041	2.12
C1-50 3-2	1.046	1.000	0.274	0.364	0.028	0.040	2.63
C1-50 3-3	1.051	1.018	0.260	0.365	0.022	0.044	1.89
C1-50 3-4	1.045	1.011	0.263	0.362	0.022	0.049	1.95
C1-50 4-1	1.042	1.001	0.245	0.377	0.020	0.049	2.34
C1-50 4-2	1.041	1.006	0.273	0.386	0.024	0.054	2.00
C1-50 4-3	1.043	1.006	0.248	0.363	0.022	0.042	2.12
C1-50 4-4	1.043	1.007	0.270	0.375	0.026	0.048	2.06
C1-50 5-1	0.939	0.916	0.281	0.354	0.019	0.039	1.32
C1-50 5-2	0.939	0.899	0.283	0.385	0.024	0.043	2.29
C1-50 5-3	0.938	0.916	0.278	0.372	0.022	0.046	1.26
C1-50 5-4	0.939	0.899	0.306	0.371	0.025	0.042	2.29
C1-50 6-1	0.940	0.898	0.241	0.341	0.022	0.038	2.40
C1-50 6-2	0.940	0.896	0.235	0.355	0.021	0.038	2.51
C1-50 6-3	0.939	0.900	0.247	0.320	0.017	0.032	2.23
C1-50 6-4	0.941	0.900	0.224	0.367	0.018	0.034	2.34
C1-50 7-1	0.939	0.900	0.266	0.327	0.023	0.039	2.23
C1-50 7-2	0.939	0.896	0.306	0.379	0.027	0.044	2.46

Hole	*D* Face 1 (Inch)[a,b]	*D* Face 2 (Inch)[a,b]	e_h Face 1	e_h Face 2	C_h Face 1 (Inch)	C_h Face 2 (Inch)	α (Degree)
C1-50 7-3	0.949	0.908	0.271	0.351	0.022	0.043	2.34
C1-50 7-4	0.946	0.909	0.297	0.398	0.027	0.052	2.12
C1-50 8-1	1.050	1.012	0.225	0.346	0.024	0.044	2.17
C1-50 8-2	1.044	1.012	0.244	0.343	0.023	0.038	1.83
C1-50 8-3	1.051	1.021	0.238	0.336	0.024	0.037	1.72
C1-50 8-4	1.050	1.011	0.235	0.350	0.040	0.039	2.23
C1-50 9-1	0.938	0.893	0.247	0.348	0.018	0.037	2.57
C1-50 9-2	0.938	0.899	0.290	0.379	0.025	0.040	2.23
C1-50 9-3	0.933	0.904	0.243	0.331	0.017	0.036	1.66
C1-50 9-4	0.938	0.896	0.257	0.357	0.023	0.035	2.40
C1-50 10-1	1.046	1.012	0.248	0.381	0.023	0.049	1.95
C1-50 10-2	1.049	1.007	0.252	0.371	0.031	0.042	2.40
C1-50 10-3	1.044	1.011	0.249	0.358	0.027	0.041	1.89
C1-50 10-4	1.048	1.003	0.222	0.369	0.019	0.047	2.57
C1-50 11-1	0.942	0.888	0.267	0.333	0.023	0.035	3.08
C1-50 11-2	0.942	0.888	0.273	0.340	0.023	0.050	3.08
C1-50 11-3	0.941	0.897	0.257	0.337	0.019	0.031	2.51
C1-50 11-4	0.945	0.893	0.288	0.363	0.022	0.038	2.97

[a]Specified *D* is 0.937 inches.
[b]Maximum allowable per the AASHTO LRFD BCS is 0.968 inches.(1)

Table 21. Dimensional measurements for series C1-50W.

Hole	*D* Face 1 (Inch)[a,b]	*D* Face 2 (Inch)[a,b]	e_h Face 1	e_h Face 2	C_h Face 1 (Inch)	C_h Face 2 (Inch)	α (Degree)
C1-50W 10-1	0.942	0.902	0.196	0.266	0.017	0.043	2.32
C1-50W 10-2	0.940	0.894	0.253	0.292	0.019	0.051	2.66
C1-50W 10-3	0.935	0.894	0.271	0.292	0.019	0.056	2.30
C1-50W 10-4	0.933	0.890	0.275	0.339	0.021	0.039	2.47
C1-50W 11-1	0.933	0.901	0.269	0.191	0.020	0.040	1.84
C1-50W 11-2	0.935	0.895	0.224	0.236	0.016	0.031	2.30
C1-50W 11-3	0.939	0.905	0.243	0.221	0.018	0.030	1.96
C1-50W 11-4	0.931	0.894	0.235	0.268	0.014	0.040	2.12
C1-50W 12-1	0.934	0.897	0.238	0.298	0.018	0.032	2.11
C1-50W 12-2	0.936	0.893	0.254	0.304	0.018	0.034	2.44
C1-50W 12-3	0.932	0.897	0.260	0.286	0.015	0.027	1.97
C1-50W 12-4	0.941	0.899	0.301	0.301	0.021	0.035	2.40
C1-50W 13-1	0.943	0.910	0.250	0.177	0.028	0.035	1.94
C1-50W 13-2	0.947	0.914	0.205	0.235	0.031	0.045	1.89
C1-50W 13-3	0.941	0.907	0.244	0.229	0.027	0.048	1.96
C1-50W 13-4	0.943	0.908	0.213	0.212	0.033	0.055	2.02
C1-50W 14-1	0.940	0.904	0.263	0.312	0.019	0.033	2.05
C1-50W 14-2	0.942	0.901	0.264	0.296	0.021	0.025	2.34
C1-50W 14-3	0.941	0.897	0.261	0.329	0.021	0.035	2.50
C1-50W 14-4	0.939	0.899	0.258	0.311	0.022	0.032	2.28
C1-50W 15-1	0.940	0.898	0.331	0.253	0.034	0.029	2.40
C1-50W 15-2	0.932	0.893	0.313	0.248	0.018	0.028	2.25

Hole	*D* Face 1 (Inch)[a,b]	*D* Face 2 (Inch)[a,b]	e_h Face 1	e_h Face 2	C_h Face 1 (Inch)	C_h Face 2 (Inch)	α (Degree)
C1-50W 15-3	0.942	0.890	0.379	0.270	0.019	0.045	2.99
C1-50W 15-4	0.940	0.893	0.305	0.293	0.020	0.035	2.68
C1-50W 16-1	0.935	0.891	0.261	0.295	0.022	0.033	2.53
C1-50W 16-2	0.941	0.900	0.249	0.326	0.025	0.044	2.35
C1-50W 16-3	0.931	0.892	0.250	0.319	0.026	0.033	2.26
C1-50W 16-4	0.936	0.896	0.258	0.306	0.026	0.032	2.29
C1-50W 17-1	0.937	0.890	0.286	0.358	0.024	0.042	2.68
C1-50W 17-2	0.940	0.886	0.272	0.326	0.031	0.038	3.05
C1-50W 17-3	0.937	0.887	0.280	0.320	0.021	0.041	2.86
C1-50W 17-4	0.940	0.896	0.300	0.313	0.028	0.039	2.51
C1-50W 18-1	0.936	0.902	0.260	0.296	0.016	0.028	1.94
C1-50W 18-2	0.938	0.898	0.245	0.266	0.019	0.031	2.28
C1-50W 18-3	0.938	0.891	0.265	0.276	0.017	0.035	2.67
C1-50W 18-4	0.936	0.901	0.237	0.305	0.014	0.034	2.03
C1-50W 19-1	0.936	0.893	0.284	0.328	0.025	0.046	2.47
C1-50W 19-2	0.940	0.891	0.299	0.317	0.026	0.036	2.81
C1-50W 19-3	0.942	0.895	0.298	0.299	0.034	0.030	2.66
C1-50W 19-4	0.935	0.891	0.274	0.292	0.020	0.041	2.52

[a]Specified *D* is 0.937 inches.
[b]Maximum allowable per the AASHTO LRFD BCS is 0.968 inches.(1)

Table 22. Dimensional measurements for series C2-36.

Hole	*D* Face 1 (Inch)[a,b]	*D* Face 2 (Inch)[a,b]	e_h Face 1	e_h Face 2	C_h Face 1 (Inch)	C_h Face 2 (Inch)	α (Degree)
C2 1-1	0.991	0.933	0.119	0.312	0.030	0.045	3.34
C2 1-2	0.974	0.913	0.168	0.294	0.025	0.038	3.47
C2 1-3	0.971	0.926	0.249	0.387	0.022	0.064	2.56
C2 1-4	0.979	0.936	0.254	0.355	0.025	0.061	2.45
C2 2-1	0.969	0.931	0.143	0.364	0.033	0.076	2.19
C2 2-2	0.970	0.936	0.245	0.397	0.024	0.062	1.91
C2 2-3	0.982	0.937	0.227	0.385	0.024	0.060	2.54
C2 2-4	0.983	0.947	0.213	0.419	0.019	0.058	2.07
C2 3-1	0.970	0.939	0.175	0.360	0.019	0.061	1.77
C2 3-2	0.974	0.939	0.164	0.370	0.019	0.052	2.00
C2 3-3	0.970	0.935	0.154	0.337	0.019	0.049	2.00
C2 3-4	0.968	0.937	0.172	0.301	0.022	0.047	1.77
C2 4-1	0.982	0.962	0.188	0.324	0.027	0.058	1.15
C2 4-2	0.961	0.950	0.116	0.367	0.018	0.059	0.63
C2 4-3	0.970	0.950	0.161	0.373	0.016	0.080	1.15
C2 4-4	0.961	0.941	0.151	0.415	0.015	0.066	1.15
C2 5-1	0.981	0.955	0.155	0.331	0.022	0.057	1.47
C2 5-2	0.982	0.936	0.186	0.430	0.027	0.088	2.62
C2 5-3	0.982	0.944	0.218	0.379	0.021	0.052	2.18
C2 5-4	0.982	0.958	0.251	0.370	0.030	0.065	1.36
C2 6-1	0.985	0.950	0.126	0.381	0.020	0.054	2.02
C2 6-2	0.989	0.969	0.085	0.306	0.026	0.046	1.15

Hole	*D* Face 1 (Inch)[a,b]	*D* Face 2 (Inch)[a,b]	e_h Face 1	e_h Face 2	C_h Face 1 (Inch)	C_h Face 2 (Inch)	α (Degree)
C2 6-3	0.970	0.970	0.092	0.352	0.020	0.054	0.05
C2 6-4	0.975	0.957	0.151	0.243	0.028	0.035	1.04
C2 7-1	0.980	0.947	0.239	0.437	0.029	0.082	1.89
C2 7-2	0.980	0.943	0.218	0.365	0.018	0.051	2.12
C2 7-3	0.979	0.942	0.234	0.412	0.029	0.077	2.12
C2 7-4	0.971	0.943	0.251	0.430	0.029	0.055	1.60
C2 8-1	0.986	0.926	0.249	0.288	0.024	0.048	3.42
C2 8-2	0.979	0.927	0.121	0.329	0.022	0.048	2.97
C2 8-3	0.982	0.929	0.136	0.337	0.023	0.069	3.03
C2 8-4	0.998	0.928	0.196	0.241	0.028	0.033	3.98
C2 9-1	0.971	0.926	0.127	0.415	0.023	0.079	2.57
C2 9-2	0.974	0.929	0.168	0.394	0.025	0.089	2.57
C2 9-3	0.971	0.953	0.216	0.404	0.029	0.057	1.03
C2 9-4	0.977	0.942	0.188	0.399	0.034	0.085	2.00
C2 10-1	0.985	0.989	0.194	0.358	0.022	0.060	0.23
C2 10-2	0.988	0.980	0.167	0.363	0.033	0.061	0.46
C2 10-3	0.985	0.987	0.175	0.379	0.031	0.068	0.11
C2 10-4	0.982	0.988	0.193	0.326	0.024	0.048	0.34

[a]Specified *D* is 0.937 inches.
[b]Maximum allowable per the AASHTO LRFD BCS is 0.968 inches.(1)

Table 23. Dimensional measurements for series E3-50W.

Hole	*D* Face 1 (Inch)[a,b]	*D* Face 2 (Inch)[a,b]	e_h Face 1	e_h Face 2	C_h Face 1 (Inch)	C_h Face 2 (Inch)	α (Degree)
E3 1-1	0.974	0.947	0.098	0.158	0.010	0.021	1.53
E3 1-2	0.977	0.946	0.054	0.195	0.008	0.021	1.80
E3 1-3	0.982	0.946	0.121	0.200	0.016	0.040	2.08
E3 1-4	0.974	0.944	0.132	0.136	0.015	0.022	1.72
E3 2-1	0.980	0.949	0.139	0.150	0.012	0.019	1.81
E3 2-2	0.978	0.956	0.069	0.131	0.010	0.022	1.22
E3 2-3	0.981	0.951	0.086	0.114	0.012	0.021	1.68
E3 2-4	0.989	0.948	0.112	0.175	0.011	0.021	2.34
E3 3-1	0.973	0.956	0.081	0.134	0.007	0.011	1.01
E3 3-2	0.978	0.952	0.091	0.141	0.010	0.017	1.51
E3 3-3	0.977	0.948	0.095	0.098	0.011	0.015	1.63
E3 3-4	0.976	0.954	0.139	0.161	0.025	0.016	1.23
E3 4-1	0.980	0.948	0.130	0.179	0.012	0.014	1.81
E3 4-2	0.993	0.951	0.111	0.165	0.013	0.014	2.37
E3 4-3	0.975	0.961	0.125	0.150	0.009	0.013	0.79
E3 4-4	0.993	0.951	0.098	0.201	0.013	0.022	2.37
E3 5-1	0.975	0.952	0.059	0.088	0.009	0.012	1.29
E3 5-2	0.978	0.953	0.108	0.194	0.008	0.014	1.43
E3 5-3	0.976	0.954	0.080	0.185	0.012	0.015	1.26
E3 5-4	0.973	0.953	0.067	0.152	0.012	0.017	1.14
E3 6-1	0.977	0.945	0.117	0.097	0.015	0.015	1.82
E3 6-2	0.980	0.949	0.109	0.212	0.013	0.025	1.76

Hole	*D* Face 1 (Inch)[a,b]	*D* Face 2 (Inch)[a,b]	e_h Face 1	e_h Face 2	C_h Face 1 (Inch)	C_h Face 2 (Inch)	α (Degree)
E3 6-3	0.972	0.954	0.087	0.164	0.005	0.018	1.07
E3 6-4	0.973	0.949	0.038	0.172	0.010	0.016	1.38
E3 7-1	0.972	0.947	0.133	0.107	0.009	0.014	1.42
E3 7-2	0.973	0.941	0.086	0.225	0.011	0.022	1.85
E3 7-3	0.975	0.952	0.071	0.161	0.007	0.033	1.35
E3 7-4	0.977	0.952	0.103	0.173	0.007	0.020	1.43
E3 9-1	0.976	0.951	0.112	0.085	0.009	0.016	1.46
E3 9-2	0.986	0.946	0.065	0.200	0.011	0.024	2.30
E3 9-3	0.980	0.950	0.121	0.117	0.013	0.023	1.72
E3 9-4	0.975	0.953	0.071	0.179	0.009	0.026	1.27
E3 10-1	0.968	0.941	0.111	0.180	0.016	0.035	1.56
E3 10-2	0.964	0.937	0.142	0.099	0.017	0.032	1.52
E3 10-3	0.970	0.943	0.092	0.138	0.015	0.022	1.51
E3 10-4	0.966	0.949	0.149	0.258	0.015	0.028	0.94

[a]Specified *D* is 0.937 inches.
[b]Maximum allowable per the AASHTO LRFD BCS is 0.968 inches.(1)

Table 24. Dimensional measurements for series E4-50W.

Hole	*D* Face 1 (Inch)[a,b]	*D* Face 2 (Inch)[a,b]	e_h Face 1	e_h Face 2	C_h Face 1 (Inch)	C_h Face 2 (Inch)	α (Degree)
E4 1-1	0.963	0.957	0.156	0.189	0.017	0.019	0.33
E4 1-2	0.970	0.952	0.126	0.178	0.029	0.018	1.05
E4 1-3	0.955	0.953	0.183	0.165	0.018	0.020	0.10
E4 1-4	0.955	0.952	0.176	0.204	0.019	0.027	0.14
E4 2-1	0.952	0.970	0.147	0.139	0.020	0.013	1.08
E4 2-2	0.956	0.954	0.171	0.154	0.018	0.012	0.08
E4 2-3	0.951	0.965	0.173	0.119	0.024	0.017	0.81
E4 2-4	0.958	0.958	0.194	0.106	0.026	0.012	0.01
E4 3-1	0.963	0.966	0.192	0.123	0.026	0.013	0.18
E4 3-2	0.962	0.962	0.139	0.076	0.020	0.017	0.02
E4 3-3	0.963	0.956	0.133	0.064	0.017	0.011	0.42
E4 3-4	0.959	0.961	0.175	0.139	0.024	0.015	0.13
E4 4-1	0.956	0.959	0.143	0.100	0.018	0.015	0.15
E4 4-2	0.960	0.968	0.159	0.149	0.029	0.020	0.42
E4 4-3	0.960	0.963	0.119	0.155	0.013	0.016	0.17
E4 4-4	0.957	0.959	0.104	0.121	0.016	0.016	0.16
E4 5-1	0.960	0.955	0.101	0.098	0.018	0.016	0.28
E4 5-2	0.967	0.955	0.144	0.080	0.025	0.015	0.69
E4 5-3	0.958	0.965	0.121	0.143	0.018	0.014	0.40
E4 5-4	0.959	0.959	0.110	0.130	0.015	0.012	0.01
E4 6-1	0.956	0.954	0.166	0.109	0.021	0.013	0.15
E4 6-2	0.951	0.952	0.195	0.102	0.017	0.015	0.05

Hole	*D* Face 1 (Inch)[a,b]	*D* Face 2 (Inch)[a,b]	e_h Face 1	e_h Face 2	C_h Face 1 (Inch)	C_h Face 2 (Inch)	α (Degree)
E4 6-3	0.956	0.956	0.156	0.114	0.025	0.018	0.02
E4 6-4	0.961	0.956	0.174	0.112	0.033	0.017	0.25
E4 7-1	0.954	0.954	0.199	0.121	0.019	0.021	0.02
E4 7-2	0.959	0.955	0.176	0.224	0.016	0.010	0.22
E4 7-3	0.959	0.959	0.153	0.136	0.021	0.020	0.05
E4 7-4	0.960	0.958	0.212	0.108	0.030	0.018	0.14
E4 8-1	0.954	0.966	0.234	0.112	0.022	0.010	0.66
E4 8-2	0.966	0.956	0.202	0.112	0.026	0.021	0.54
E4 8-3	0.960	0.956	0.182	0.126	0.025	0.018	0.26
E4 8-4	0.960	0.957	0.218	0.149	0.025	0.022	0.19
E4 9-1	0.960	0.948	0.140	0.167	0.023	0.016	0.66
E4 9-2	0.959	0.947	0.170	0.207	0.017	0.018	0.67
E4 9-3	0.961	0.949	0.159	0.138	0.025	0.018	0.68
E4 9-4	0.964	0.950	0.177	0.174	0.026	0.017	0.81
E4 10-1	0.956	0.968	0.148	0.152	0.020	0.016	0.68
E4 10-2	0.958	0.959	0.179	0.090	0.015	0.017	0.05
E4 10-3	0.958	0.959	0.164	0.125	0.014	0.030	0.06
E4 10-4	0.957	0.961	0.123	0.110	0.017	0.016	0.23

[a]Specified *D* is 0.937 inches.
[b]Maximum allowable per the AASHTO LRFD BCS is 0.968 inches.(1)

Table 25. Dimensional measurements for drilled holes.

Hole	*D* Face 1 (Inch)[a,b]	*D* Face 2 (Inch)[a,b]	e_h Face 1	e_h Face 2	C_h Face 1 (Inch)	C_h Face 2 (Inch)	α (Degree)
Hole 1	0.824	0.839	0.068	0.046	0.004	0.010	0.87
Hole 2	0.824	0.831	0.091	0.100	0.006	0.004	0.43
Hole 3	0.824	0.833	0.056	0.054	0.011	0.003	0.52
Hole 4	0.824	0.833	0.105	0.035	0.005	0.004	0.52
Hole 5	0.823	0.835	0.082	0.027	0.003	0.003	0.66
Hole 6	0.822	0.835	0.022	0.058	0.003	0.002	0.72
Hole 7	0.823	0.835	0.087	0.105	0.006	0.005	0.71
Hole 8	0.825	0.834	0.085	0.076	0.005	0.008	0.48
Hole 9	0.822	0.835	0.088	0.067	0.004	0.003	0.73
Hole 10	0.823	0.832	0.044	0.074	0.004	0.005	0.53

[a]Specified *D* is 0.813 inches.
[b]Maximum allowable per the AASHTO LRFD BCS is 0.843 inches.(1)

APPENDIX B. FATIGUE TESTING DATA

Table 26 through table 36 present the raw data from all fatigue tests in this study. Plate-fatigue test data are provided first, followed by connection-fatigue test data. Tests that reached 20 million cycles without fatigue crack initiation were declared runout specimens and were excluded from the regression analysis. Specimens that developed a fatigue crack near the grips or fixtures (i.e., away from the net section) and outlier data points were also excluded from the regression analysis.

Table 26. Plate-fatigue tests results for series C1-50.

Specimen ID	Minimum Load (kips)	Maximum Load (kips)	Stress Range (ksi)	Cycles to Failure	Notch Angle (Degree)	Failure at Notch
C1-50-1p	5.0	42.5	14.8	743,159	10	Yes
C1-50-2p	5.0	42.5	14.8	952,589	5	Yes
C1-50-3p	5.0	42.5	14.8	759,604	5	Yes
C1-50-4p	5.0	42.5	14.8	1,195,713	5	Yes
C1-50-5p	5.0	42.5	14.8	1,150,967	5	Yes
C1-50-6p	5.0	42.5	14.8	671,809	0	Yes
C1-50-7p	5.0	42.5	14.8	710,017	0	Yes
C1-50-8p	5.0	42.5	14.8	1,036,356	10	Yes
C1-50-9p	5.0	42.5	14.8	1,091,122	5	Yes
C1-50-10p	5.0	42.5	14.8	901,768	5	Yes
C1-50-11p	5.0	42.5	14.8	692,175	0	Yes
C1-50-12p	5.0	42.5	14.8	666,638	15	Yes
C1-50-13p	5.0	42.5	14.8	1,075,304	20	Yes
C1-50-14p	5.0	42.5	14.8	880,122	15	Yes
C1-50-15p	5.0	42.5	14.8	763,958	25	Yes

Table 27. Plate-fatigue test results for series C1-50W.

Specimen ID	Minimum Load (kips)	Maximum Load (kips)	Stress Range (ksi)	Cycles to Failure	Notch Angle (Degree)	Failure at Notch
C1-50W-1p	5.0	65.0	23.7	256,957	45	Yes
C1-50W-2p	5.0	[a]	19.6[a]	13,213,524[b]	45	[c]
C1-50W-3p	5.0	50.0	17.8	665,052	50	Yes
C1-50W-4p	5.0	50.0	17.8	609,140	45	Yes
C1-50W-5p	5.0	35.0	11.8	2,045,795	40	Yes
C1-50W-6p	5.0	65.0	23.7	735,589	45	Yes
C1-50W-7p	5.0	35.0	11.8	2,711,776	50	Yes
C1-50W-8p	5.0	50.0	17.8	616,043	50	Yes
C1-50W-9p	5.0	50.0	17.8	20,000,000[d]	30	[d]
C1-50W-10p	5.0	50.0	17.8	1,041,136	60	Yes
C1-50W-11p	5.0	50.0	17.8	1,281,652	35	No
C1-50W-12p	5.0	42.5	14.8	1,191,104	40	Yes
C1-50W-13p	5.0	42.5	14.8	1,805,837	40	Yes
C1-50W-14p	5.0	42.5	14.8	1,347,972	30	Yes
C1-50W-15p	5.0	42.5	14.8	20,000,000[d]	45	[d]
C1-50W-16p	5.0	42.5	14.8	1,137,104	40	Yes
C1-50W-17p	5.0	42.5	14.8	1,294,024	30	Yes
C1-50W-18p	5.0	42.5	14.8	959,107	35	Yes
C1-50W-19p	5.0	42.5	14.8	1,238,552	45	Yes
C1-50W-20p	5.0	42.5	14.8	2,378,009	50	Yes
C1-50W-21p	5.0	50.0	17.8	6,863,016	40	[c]
C1-50W-22p	5.0	50.0	17.8	758,724	50	Yes
C1-50W-23p	5.0	42.5	14.8	1,247,862	45	Yes
C1-50W-24p	5.0	[a]	15.2[a]	10,212,287[c]	40	Yes
C1-50W-25p	5.0	42.5	14.8	1,327,279	45	Yes

[a]Specimen tested at multiple stress ranges. Stress range reported as an equivalent stress range based on the Palmgren–Miner rule.
[b]Data point was determined to be an outlier and was excluded from regression analysis.
[c]Specimen failed in the grips and was excluded from regression analysis.
[d]Declared a runout specimen and excluded from regression analysis.

Table 28. Plate-fatigue test results for series C2-50W.

Specimen ID	Minimum Load (kips)	Maximum Load (kips)	Stress Range (ksi)	Cycles to Failure	Notch Angle (Degree)	Failure at Notch
C2-50W-1p	5.0	50.0	17.8	784,827	5	Yes
C2-50W-4p	5.0	50.0	17.8	661,611	0	Yes
C2-50W-6p	5.0	50.0	17.8	814,847	[a]	Yes
C2-50W-7p	5.0	50.0	17.8	442,644	5	Yes
C2-50W-8p	5.0	50.0	17.8	989,505	[a]	Yes
C2-50W-9p	5.0	50.0	17.8	597,979	[a]	Yes
C2-50W-11p	5.0	50.0	17.8	737,691	25	Yes
C2-50W-12p	5.0	50.0	17.8	547,509	0	Yes
C2-50W-13p	5.0	50.0	17.8	524,860	0	Yes
C2-50W-14p	5.0	50.0	17.8	508,483	20	Yes
C2-50W-15p	5.0	50.0	17.8	396,243	0	Yes
C2-50W-18p	5.0	50.0	17.8	644,395	20	No
C2-50W-19p	5.0	50.0	17.8	759,429	[a]	Yes
C2-50W-20p	5.0	50.0	17.8	568,410	[a]	Yes
C2-50W-21p	5.0	50.0	17.8	451,776	[a]	Yes

[a]Hole had an extensive area of noticeable surface defects unlike the distinct surface flaw observed on other specimens.

Table 29. Plate-fatigue test results for series C2-36.

Specimen ID	Minimum Load (kips)	Maximum Load (kips)	Stress Range (ksi)	Cycles to Failure	Notch Angle (Degree)	Failure at Notch
C2-36-2p	5.0	50.0	17.8	855,545	0	Yes
C2-36-3p	5.0	50.0	17.8	520,518	0	Yes
C2-36-5p	5.0	50.0	17.8	492,274	0	Yes
C2-36-10p	5.0	[a]	12.3[a]	10,519,403[b]	0	No
C2-36-16p	5.0	50.0	17.8	3,148,124[b]	[c]	Yes
C2-36-17p	5.0	50.0	17.8	414,950	0	Yes
C2-36-22p	5.0	50.0	17.8	560,045	0	Yes
C2-36-23p	5.0	50.0	17.8	440,701	0	Yes
C2-36-24p	5.0	50.0	17.8	492,113	0	Yes
C2-36-25p	5.0	50.0	17.8	427,989	5	Yes

[a]Tested at multiple stress ranges. Stress range represents an equivalent stress range based on the Palmgren–Miner rule.
[b]Data point was determined to be an outlier and was excluded from regression analysis.
[c]Hole had an extensive area of noticeable surface defects unlike the distinct surface flaw observed on other specimens.

Table 30. Plate-fatigue test results for series E3-50W.

Specimen ID	Minimum Load (kips)	Maximum Load (kips)	Stress Range (ksi)	Cycles to Failure	Notch Angle (Degree)	Failure at Notch
E3-90-1p	5.0	55.6	20.0	646,188	90	No
E3-90-2p	5.0	55.6	20.0	1,173,623	90	No
E3-90-3p	5.0	55.0	19.7	20,000,000[a]	90	[a]
E3-90-4p	5.0	55.0	19.7	10,745,156[b]	90	No
E3-90-5p	5.0	55.0	19.7	497,172	90	No
E3-90-6p	5.0	55.0	19.7	[c]	90	[d]
E3-45-1p	5.0	55.0	19.7	20,000,000[a]	45	[a]
E3-45-2p	5.0	65.0	23.7	4,906,261[b]	45	No
E3-45-3p	5.0	65.0	23.7	390,440	45	No
E3-45-4p	5.0	65.0	23.7	298,216	45	No
E3-45-5p	5.0	65.0	23.7	364,123	45	No
E3-45-6p	5.0	65.0	23.7	399,691	45	No
E3-45-7p	5.0	65.0	23.7	910,863	45	No
E3-45-8p	5.0	65.0	23.7	20,000,000[a]	45	[a]
E3-45-9p	5.0	65.0	23.7	248,751	45	No
E3-45-10p	5.0	65.0	23.7	7,897,929[b]	45	No
E3-0-1p	5.0	55.0	19.7	524,415	0	Yes
E3-0-2p	5.0	65.0	23.7	20,000,000[a]	0	[a]
E3-0-3p	5.0	65.0	23.7	427,734	0	Yes
E3-0-4p	5.0	65.0	23.7	345,459	0	Yes
E3-0-5p	5.0	65.0	23.7	586,460	0	Yes
E3-0-6p	5.0	65.0	23.7	242,410	0	Yes
E3-0-7p	5.0	65.0	23.7	218,182	0	Yes
E3-0-8p	5.0	65.0	23.7	224,580	0	Yes
E3-0-9p	5.0	65.0	23.7	349,225	0	Yes
E3-0-10p	5.0	65.0	23.7	255,191	0	Yes

[a]Declared a runout specimen and excluded from regression analysis.
[b]Data point was determined to be an outlier and was excluded from regression analysis.
[c]Accurate cycle count for this specimen could not be determined due to lost data.
[d]Specimen failed in the grips and was excluded from regression analysis.

Table 31. Plate-fatigue test results for series E4-50W.

Specimen ID	Minimum Load (kips)	Maximum Load (kips)	Stress Range (ksi)	Cycles to Failure	Notch Angle (Degree)	Failure at Notch
E4-90-1p	5.0	65.0	23.7	294,821	90	No
E4-90-2p	5.0	65.0	23.7	665,514	90	No
E4-90-3p	5.0	65.0	23.7	403,450	90	No
E4-90-4p	5.0	65.0	23.7	501,957	90	No
E4-90-5p	5.0	65.0	23.7	328,586	90	No
E4-90-6p	5.0	65.0	23.7	279,738	90	No
E4-45-1p	5.0	65.0	23.7	440,879	45	No
E4-45-2p	5.0	65.0	23.7	478,462	45	No
E4-45-3p	5.0	65.0	23.7	538,160	45	No
E4-45-4p	5.0	65.0	23.7	576,174	45	No
E4-45-5p	5.0	65.0	23.7	[a]	45	[a]
E4-45-6p	5.0	65.0	23.7	644,146	45	No
E4-45-7p	5.0	65.0	23.7	409,410	45	No
E4-45-8p	5.0	65.0	23.7	544,657	45	No
E4-45-9p	5.0	65.0	23.7	309,811	45	No
E4-45-10p	5.0	65.0	23.7	327,027	45	No
E4-0-1p	5.0	65.0	23.7	321,462	0	Yes
E4-0-2p	5.0	56.0	23.7	391,446	0	Yes
E4-0-3p	5.0	65.0	23.7	461,499	0	Yes
E4-0-4p	5.0	65.0	23.7	334,119	0	Yes
E4-0-5p	5.0	65.0	23.7	371,540	0	Yes
E4-0-6p	5.0	65.0	23.7	422,438	0	Yes
E4-0-7p	5.0	65.0	23.7	321,811	0	Yes
E4-0-8p	5.0	65.0	23.7	387,701	0	Yes
E4-0-9p	5.0	65.0	23.7	338,921	0	Yes
E4-0-10p	5.0	65.0	23.7	296,210	0	Yes

[a]Specimen never reached failure and an accurate cycle count could not be determined due to lost data.

Table 32. Connection-fatigue test results for series C1-50.

Specimen ID	Minimum Load (kips)	Maximum Load (kips)	Stress Range (ksi)	Cycles to Failure	Notch Angle (Degree)	Failure at Notch	Hole Fit[a]
C1-50-1c	5.0	41.0	17.5	428,393	5	Yes	Okay
C1-50-2c	5.0	41.0	17.5	432,794	5	Yes	Loose
C1-50-3c	5.0	41.0	17.5	1,144,566	10	Yes	Loose
C1-50-4c	5.0	41.0	17.5	749,778	10	Yes	Loose
C1-50-5c	5.0	41.0	17.5	276,364	5	Yes	Tight
C1-50-6c	5.0	41.0	17.5	478,272	10	Yes	Okay
C1-50-7c	5.0	41.0	17.5	221,475	0	Yes	Tight
C1-50-8c	5.0	41.0	17.5	329,025	5	Yes	Loose
C1-50-9c	5.0	41.0	17.5	403,571	0	Yes	Tight
C1-50-10c	5.0	41.0	17.5	547,446	5	Yes	Loose
C1-50-11c	5.0	41.0	17.5	276,740	5	Yes	Tight
C1-50-12c	5.0	41.0	17.5	277,644[b]	0	[b]	Loose
C1-50-13c	5.0	41.0	17.5	526,096	5	Yes	Loose
C1-50-14c	5.0	55.0	24.2	128,188	5	Yes	Okay
C1-50-15c	5.0	55.0	24.2	128,188	5	Yes	Okay
C1-50-16c	5.0	41.0	17.5	441,866	10	Yes	Tight
C1-50-17c	5.0	41.0	17.5	948,316	15	Yes	Loose
C1-50-18c	5.0	41.0	17.5	393,865	20	Yes	Loose
C1-50-19c	5.0	41.0	17.5	365,233	20	Yes	Tight
C1-50-20c	5.0	41.0	17.5	199,750	5	Yes	Okay
C1-50-21c	5.0	41.0	17.5	275,278	5	Yes	Okay
C1-50-22c	5.0	41.0	17.5	408,377	5	Yes	Tight

Specimen ID	Minimum Load (kips)	Maximum Load (kips)	Stress Range (ksi)	Cycles to Failure	Notch Angle (Degree)	Failure at Notch	Hole Fit[a]
C1-50-23c	5.0	41.0	17.5	346,770	5	Yes	Tight
C1-50-24c	5.0	41.0	17.5	196,985	5	Yes	Tight
C1-50-25c	5.0	41.0	17.5	306,427	5	Yes	Tight
C1-50-26c	5.0	41.0	17.5	833,543	15	Yes	Loose
C1-50-27c	5.0	41.0	17.5	605,450	5	Yes	Loose
C1-50-28c	5.0	41.0	17.5	748,208	10	Yes	Loose
C1-50-29c	5.0	41.0	17.5	248,581	0	Yes	Tight
C1-50-30c	5.0	41.0	17.5	245,859	0	Yes	Tight

[a]The *D* of several holes in this series of specimens was either too large or too small, resulting in a loose- or tight-fitting bolt accommodation.
[b]Specimen was used in last connection tested and never achieved failure; it is considered a runout and excluded from regression analysis.

Table 33. Connection-fatigue test results for series C1-50W.

Specimen ID	Minimum Load (kips)	Maximum Load (kips)	Stress Range (ksi)	Cycles to Failure	Notch Angle (Degree)	Failure at Notch
C1-50W-1c	5.0	50.0	21.8	166,052	35	Yes
C1-50W-2c	5.0	50.0	21.8	244,319	40	Yes
C1-50W-3c	5.0	[a]	16.6[a]	8,903,803[b]	35	No
C1-50W-4c	5.0	39.0	16.5	2,947,087[c]	35	Yes
C1-50W-5c	5.0	39.0	16.5	1,362,596	45	No
C1-50W-6c	5.0	39.0	16.5	8,876,127[c,d]	40	[d]
C1-50W-7c	5.0	39.0	16.5	7,020,512[b]	35	Yes
C1-50W-8c	5.0	39.0	16.5	11,540,519[c]	40	No
C1-50W-9c	5.0	55.0	24.2	392,761	40	Yes
C1-50W-10c	5.0	55.0	24.2	439,708	40	Yes
C1-50W-11c	5.0	55.0	24.2	158,261	40	Yes
C1-50W-12c	5.0	55.0	24.2	352,483	35	Yes
C1-50W-13c	5.0	55.0	24.2	266,061	45	Yes
C1-50W-14c	5.0	55.0	24.2	235,483	40	Yes
C1-50W-15c	5.0	55.0	24.2	202,519	40	Yes
C1-50W-16c	5.0	55.0	24.2	289,376	35	Yes
C1-50W-17c	5.0	55.0	24.2	634,920	40	No
C1-50W-18c	5.0	55.0	24.2	268,998	40	Yes
C1-50W-19c	5.0	55.0	24.2	156,103	45	Yes
C1-50W-20c	5.0	55.0	24.2	439,538	40	Yes
C1-50W-21c	5.0	55.0	24.2	627,430	40	Yes
C1-50W-22c	5.0	55.0	24.2	769,132	40	Yes
C1-50W-23c	5.0	55.0	24.2	1,829,848	45	Yes
C1-50W-24c	5.0	55.0	24.2	1,210,826	35	Yes
C1-50W-25c	5.0	55.0	24.2	399,293	35	No
C1-50W-26c	5.0	55.0	24.2	297,532	45	Yes
C1-50W-27c	5.0	55.0	24.2	341,977	45	Yes

Specimen ID	Minimum Load (kips)	Maximum Load (kips)	Stress Range (ksi)	Cycles to Failure	Notch Angle (Degree)	Failure at Notch
C1-50W-28c	5.0	55.0	24.2	781,754	45	Yes
C1-50W-29c	5.0	55.0	24.2	835,921	45	Yes
C1-50W-30c	5.0	55.0	24.2	129,682	45	Yes

[a]Specimen tested at multiple maximum loads. Stress range reported represents an equivalent stress range based on the Palmgren–Miner rule.
[b]Data point was determined to be an outlier and was excluded from regression analysis.
[c]Splice plates prohibited observation of the fatigue crack for an undetermined number of cycles, preventing an accurate cycle count. This specimen was excluded from regression analysis.
[d]Specimen was used in last connection test and never developed a fatigue crack.

Table 34. Connection-fatigue test results for series C2-36.

Specimen ID	Minimum Load (kips)	Maximum Load (kips)	Stress Range (ksi)	Cycles to Failure	Notch Angle (Degree)	Failure at Notch
C2-36-1c	5.0	41.0	12.0[a]	10,000,000	0	[a]
C2-36-2c	5.0	41.0	12.0[a]	10,000,000	10	[a]
C2-36-3c	5.0	41.0	17.5	1,764,150	0	Yes
C2-36-4c	5.0	41.0	17.5	283,286	25	Yes
C2-36-5c	5.0	41.0	12.0[a]	10,000,000	10	[a]
C2-36-6c	5.0	41.0	12.0[a]	10,000,000	25	[a]
C2-36-7c	5.0	41.0	17.5	1,027,895	20	Yes
C2-36-8c	5.0	41.0	17.5	180,131	5	Yes
C2-36-9c	5.0	41.0	17.5	424,730	0	Yes
C2-36-10c	5.0	41.0	17.5	3,946,382	10	Yes
C2-36-11c	5.0	55.0	24.2	187,239	25	Yes
C2-36-12c	5.0	55.0	24.2	169,228	0	Yes
C2-36-13c	5.0	55.0	24.2	212,059	10	Yes
C2-36-14c	5.0	55.0	24.2	378,699	15	Yes
C2-36-15c	5.0	55.0	24.2	163,151	5	Yes
C2-36-16c	5.0	[b]	17.7[b]	908,732	20	Yes
C2-36-17c	5.0	41.0	17.5	1,136,882	5	Yes
C2-36-18c	5.0	41.0	17.5	450,589	0	Yes
C2-36-19c	5.0	41.0	17.5	1,537,194	20	Yes
C2-36-20c	5.0	41.0	17.5	715,492	25	Yes
C2-36-21c	5.0	41.0	17.5	865,373	20	Yes
C2-36-22c	5.0	41.0	17.5	242,415	10	Yes
C2-36-23c	5.0	41.0	17.5	275,914	10	Yes
C2-36-24c	5.0	41.0	17.5	819,697	0	Yes
C2-36-25c	5.0	41.0	17.5	1,148,132	20	Yes
C2-36-26c	5.0	41.0	17.5	1,367,605	15	Yes
C2-36-27c	5.0	41.0	17.5	297,951	5	Yes
C2-36-28c	5.0	41.0	17.5	1,292,552	5	Yes
C2-36-29c	5.0	41.0	17.5	486,727	0	Yes
C2-36-30c	5.0	41.0	17.5	543,562	15	Yes

[a]Specimen was fatigue tested with pretensioned bolts, never cracked, and was declared a runout. Stress range was based on the gross specimen area to be consistent with AASHTO LRFD BDS.
[b]Tested at numerous maximum loads. The stress range reported represents an equivalent stress range based on the Palmgren–Miner rule.

Table 35. Connection-fatigue test results for series E3-50W.

Specimen ID	Minimum Load (kips)	Maximum Load (kips)	Stress Range (ksi)	Cycles to Failure	Notch Angle (Degree)	Failure at Notch
E3-90-1c	5.0	41.0	17.5	1,331,388	90	No
E3-90-2c	5.0	41.0	17.5	3,410,790	90	No
E3-90-3c	5.0	41.0	17.5	1,236,482	90	No
E3-90-4c	5.0	41.0	17.5	1,190,665	90	No
E3-90-5c	5.0	41.0	17.5	1,904,136	90	No
E3-90-6c	5.0	41.0	17.5	2,212,901	90	No
E3-90-7c	5.0	41.0	17.5	656,510	90	No
E3-90-8c	5.0	49.0	21.3	514,816	90	No
E3-45-1c	5.0	41.0	17.5	9,982,755[a]	45	No
E3-45-2c	5.0	41.0	17.5	2,447,066	45	Yes
E3-45-3c	5.0	49.0	17.5	15,623,185[a]	45	Yes
E3-45-4c	5.0	49.0	21.3	3,555,263	45	Yes
E3-45-5c	5.0	49.0	21.3	1,348,593	45	Yes
E3-45-6c	5.0	49.0	21.3	1,232,287	45	Yes
E3-45-7c	5.0	49.0	21.3	1,237,243	45	Yes
E3-45-8c	5.0	49.0	21.3	1,478,067	45	Yes
E3-45-9c	5.0	49.0	21.3	620,995	45	Yes
E3-45-10c	5.0	49.0	21.3	739,359	45	Yes
E3-45-11c	5.0	49.0	21.3	1,581,371	45	No
E3-45-12c	5.0	49.0	21.3	651,267	45	Yes
E3-45-13c	5.0	49.0	21.3	976,855	45	Yes
E3-45-14c	5.0	49.0	21.3	247,767	45	Yes
E3-0-1c	5.0	49.0	21.3	1,009,204	0	Yes
E3-0-2c	5.0	49.0	21.3	2,359,085	0	Yes
E3-0-3c	5.0	49.0	21.3	372,085	0	Yes
E3-0-4c	5.0	49.0	21.3	309,977	0	Yes
E3-0-5c	5.0	49.0	21.3	249,515	0	Yes
E3-0-6c	5.0	49.0	21.3	342,160	0	Yes
E3-0-7c	5.0	49.0	21.3	349,954	0	Yes
E3-0-8c	5.0	49.0	21.3	283,344	0	Yes
E3-0-9c	5.0	49.0	21.3	320,027	0	Yes
E3-0-10c	5.0	49.0	21.3	1,009,683	0	Yes
E3-0-11c	5.0	49.0	21.3	443,220	0	Yes

Specimen ID	Minimum Load (kips)	Maximum Load (kips)	Stress Range (ksi)	Cycles to Failure	Notch Angle (Degree)	Failure at Notch
E3-0-12c	5.0	49.0	21.3	244,969	0	Yes
E3-0-13c	5.0	49.0	21.3	275,708	0	Yes
E3-0-14c	5.0	49.0	21.3	321,794	0	Yes

[a]Specimen declared an outlier and excluded from regression analysis.

Table 36. Connection-fatigue test results for series E4-50W.

Specimen ID	Minimum Load (kips)	Maximum Load (kips)	Stress Range (ksi)	Cycles to Failure	Notch Angle (Degree)	Failure at Notch
E4-90-1c	5.0	49.0	21.3	407,352	90	No
E4-90-2c	5.0	49.0	21.3	525,300	90	No
E4-90-3c	5.0	49.0	21.3	2,155,451	90	No
E4-90-4c	5.0	49.0	21.3	557,957	90	No
E4-90-5c	5.0	49.0	21.3	472,528	90	No
E4-90-6c	5.0	49.0	21.3	592,176	90	No
E4-90-7c	5.0	49.0	21.3	442,150	90	No
E4-90-8c	5.0	49.0	21.3	615,302	90	No
E4-45-1c	5.0	49.0	21.3	1,709,480	45	Yes
E4-45-2c	5.0	49.0	21.3	430,274	45	Yes
E4-45-3c	5.0	49.0	21.3	494,375	45	No
E4-45-4c	5.0	49.0	21.3	574,704	45	Yes
E4-45-5c	5.0	49.0	21.3	561,951	45	No
E4-45-6c	5.0	49.0	21.3	406,538	45	No
E4-45-7c	5.0	49.0	21.3	436,417	45	No
E4-45-8c	5.0	49.0	21.3	496,412	45	No
E4-45-9c	5.0	49.0	21.3	695,680	45	Yes
E4-45-10c	5.0	49.0	21.3	928,531	45	Yes
E4-45-11c	5.0	49.0	21.3	1,960,343	45	Yes
E4-45-12c	5.0	49.0	21.3	2,132,263	45	Yes
E4-45-13c	5.0	49.0	21.3	503,450	45	Yes
E4-45-14c	5.0	49.0	21.3	450,012	45	No
E4-0-1c	5.0	49.0	21.3	2,918,078	0	Yes
E4-0-2c	5.0	49.0	21.3	694,154	0	Yes
E4-0-3c	5.0	49.0	21.3	649,423	0	Yes
E4-0-4c	5.0	49.0	21.3	260,927	0	Yes
E4-0-5c	5.0	49.0	21.3	368,912	0	Yes
E4-0-6c	5.0	49.0	21.3	508,726	0	Yes
E4-0-7c	5.0	49.0	21.3	297,001	0	Yes
E4-0-8c	5.0	49.0	21.3	291,796	0	Yes
E4-0-9c	5.0	49.0	21.3	291,796	0	Yes
E4-0-10c	5.0	49.0	21.3	2,080,373	0	Yes
E4-0-11c	5.0	49.0	21.3	595,216	0	Yes

Specimen ID	Minimum Load (kips)	Maximum Load (kips)	Stress Range (ksi)	Cycles to Failure	Notch Angle (Degree)	Failure at Notch
E4-0-12c	5.0	49.0	21.3	346,419	0	Yes
E4-0-13c	5.0	49.0	21.3	708,310	0	Yes
E4-0-14c	5.0	49.0	21.3	1,151,103	0	Yes

APPENDIX C. MATERIAL CHARACTERIZATION

This appendix contains information about the material properties of all steel procured for this study. Data for chemical composition, tensile testing, and CVN impact energy are reported. The chemical composition of material provided by fabricators C1, E3, and E4 is based on mill certifications delivered during material procurement. The chemical analysis for steel provided by fabricator C2 was performed by an independent laboratory. All steel provided for this study met ASTM A709 requirements.[9]

CHEMICAL ANALYSIS

Table 37 provides the chemical composition of each type of steel provided by the four fabricators. Data for fabricators C1, E3, and E4 are as reported in material certification documents provided by the steel supplier used by each fabricator. Similar documents were not provided for fabricator C2, so the chemical composition of material provided by fabricator C2 needed to be determined. A small core was extracted out of 9 plate-fatigue test specimens from series C2-36 and 15 plate-fatigue specimens from series C2-50W and sent to an independent metallurgical laboratory for a standard 9-element compositional analysis. The values reported in table 37 represent the average of all these compositional analyses.

Table 37. Material chemical composition (percent by weight).

Element	C1-50	C1-50W	C2-36	C2-50W	E3-50W	E4-50W
Carbon	0.18	0.16	0.17	0.13	0.14	0.13
Manganese	0.92	1.09	0.76	1.10	1.06	0.98
Phosphorus	0.013	0.013	0.017	0.019	0.010	0.009
Sulfur	0.001	0.002	0.006	0.005	0.003	0.023
Silicon	0.24	0.35	0.02	0.44	0.383	0.34
Copper	0.31	0.31	0.04	0.28	0.283	0.32
Nickel	0.08	0.22	0.01	0.18	0.16	0.08
Chromium	0.09	0.50	0.04	0.54	0.57	0.45
Molybdenum	0.01	0.02	0.01	0.01	0.005	0.02
Vanadium	0.029	0.031	—	—	0.035	0.026
Carbon Equivalent	0.43	0.55	0.31	0.53	0.53	0.48

—Value not provided.

TENSILE TESTING

Tensile specimens were prepared and tested in accordance with the ASTM E8 standard specification.[17] Tensile specimens were fabricated from extra material provided by the fabricator from the same motherplate as the specimens. Engineering stress versus strain data are plotted in figure 68 through figure 73 for series C1-50, C1-50W, C2-36, C2-50W, E3-50W, and

E4-50W, respectively. Individual results for tensile strength, yield strength, elongation, and area reduction are summarized in table 38.

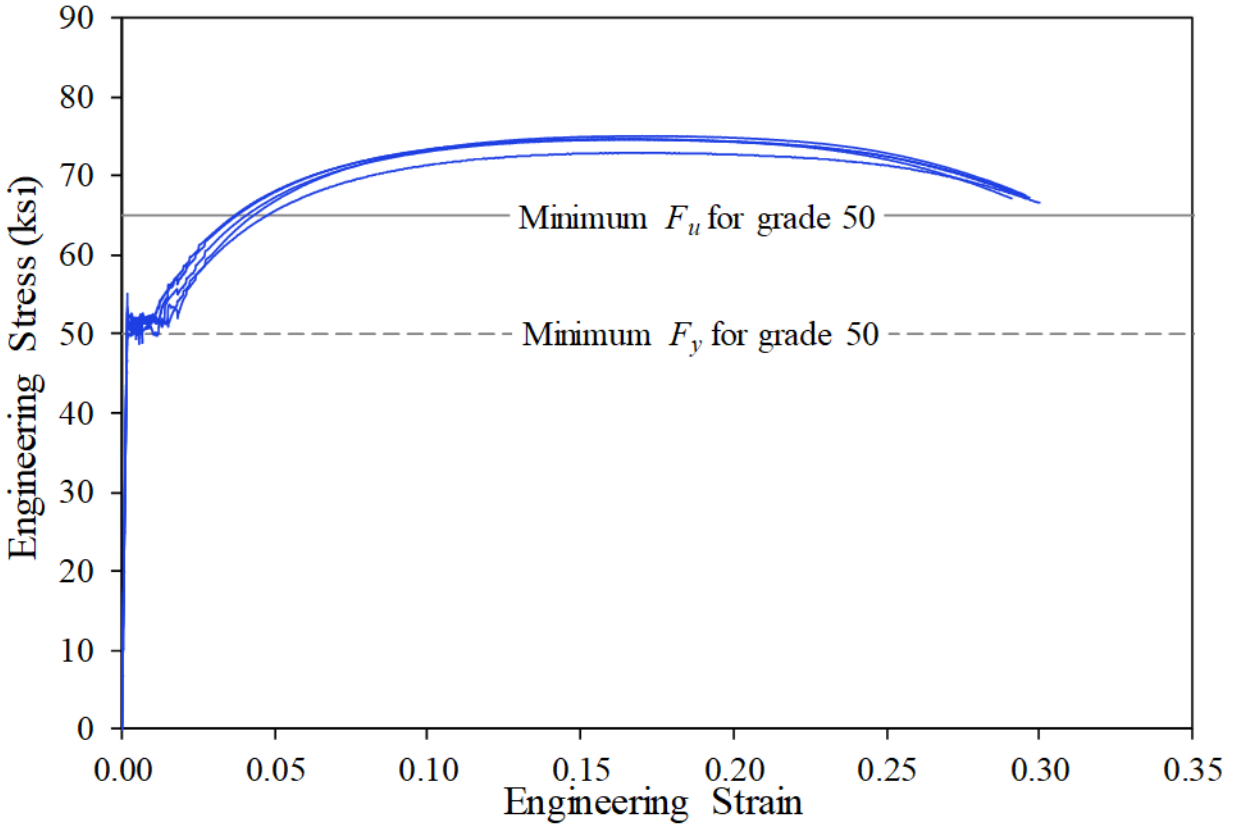

Source: FHWA.

Figure 68. Graph. Engineering stress versus strain for series C1-50.

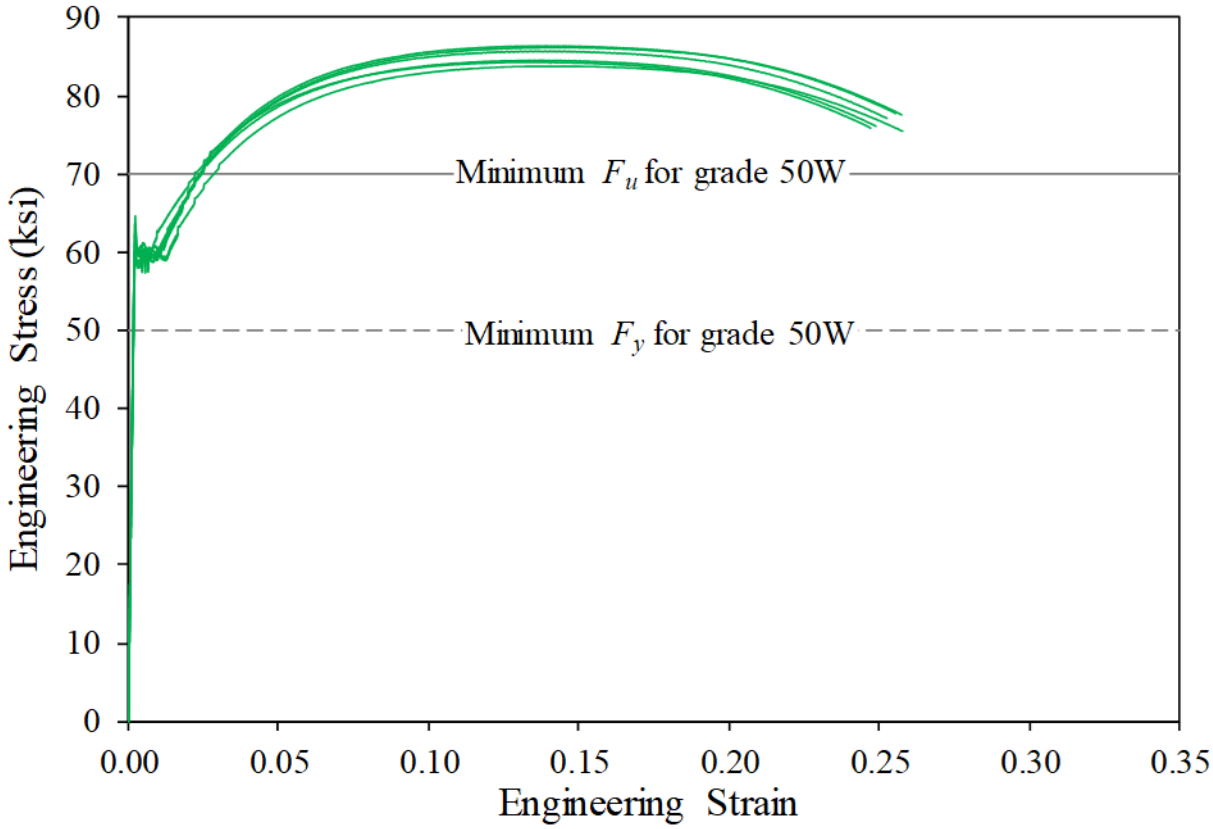

Source: FHWA.

Figure 69. Graph. Engineering stress versus strain for series C1-50W.

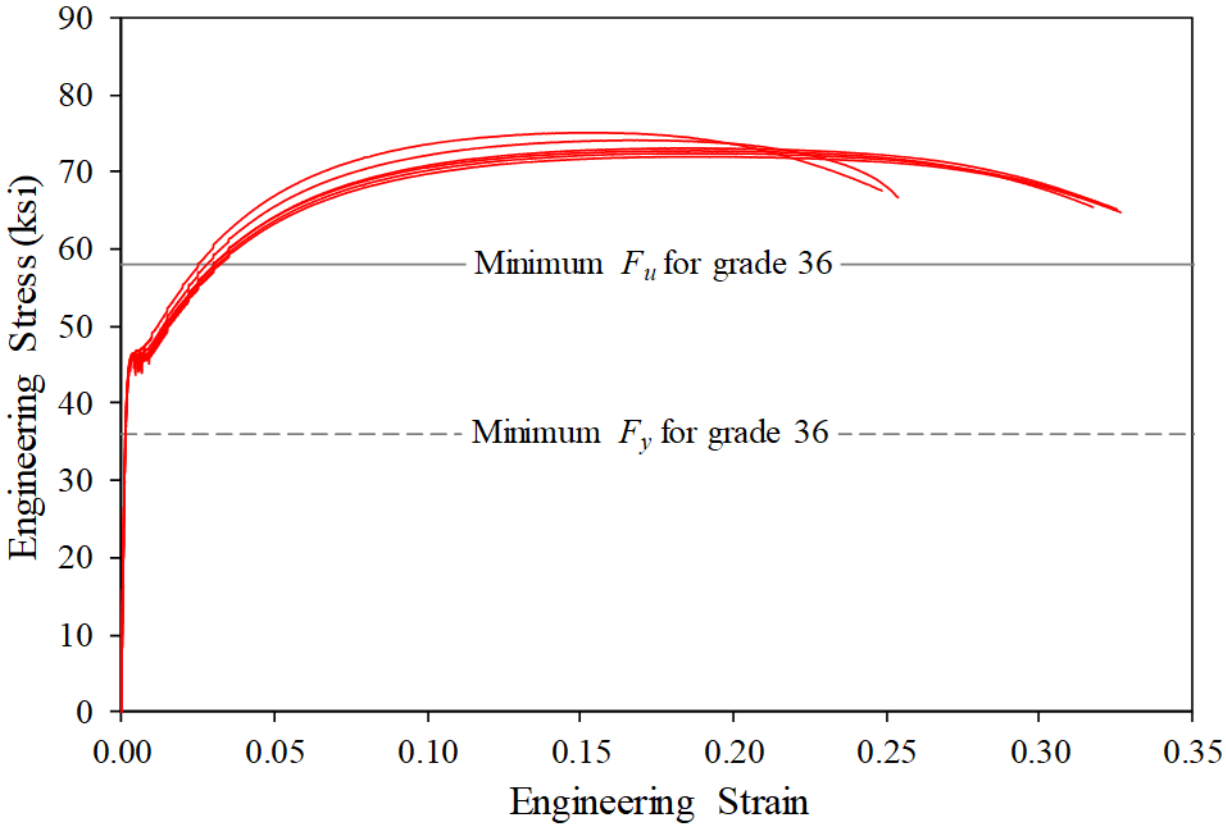

Source: FHWA.

Figure 70. Graph. Engineering stress versus strain for series C2-36.

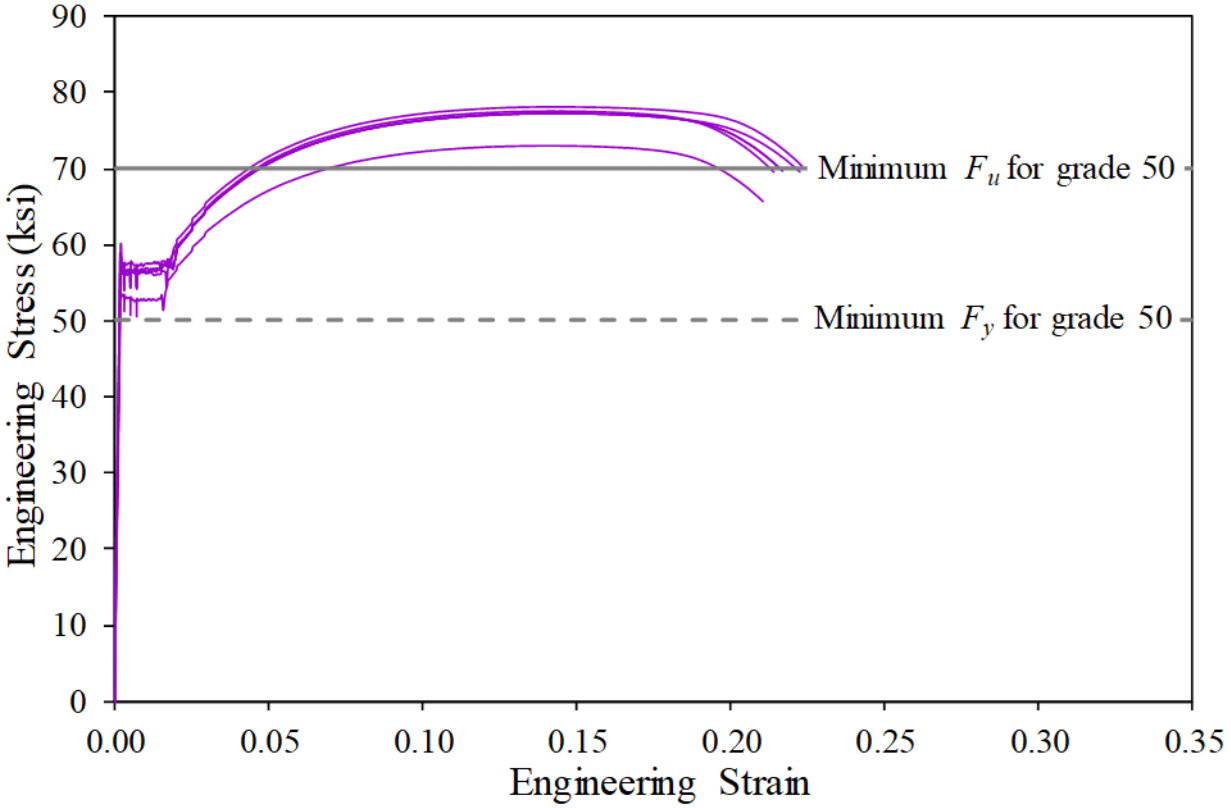

Source: FHWA.

Figure 71. Graph. Engineering stress versus strain for series C2-50W.

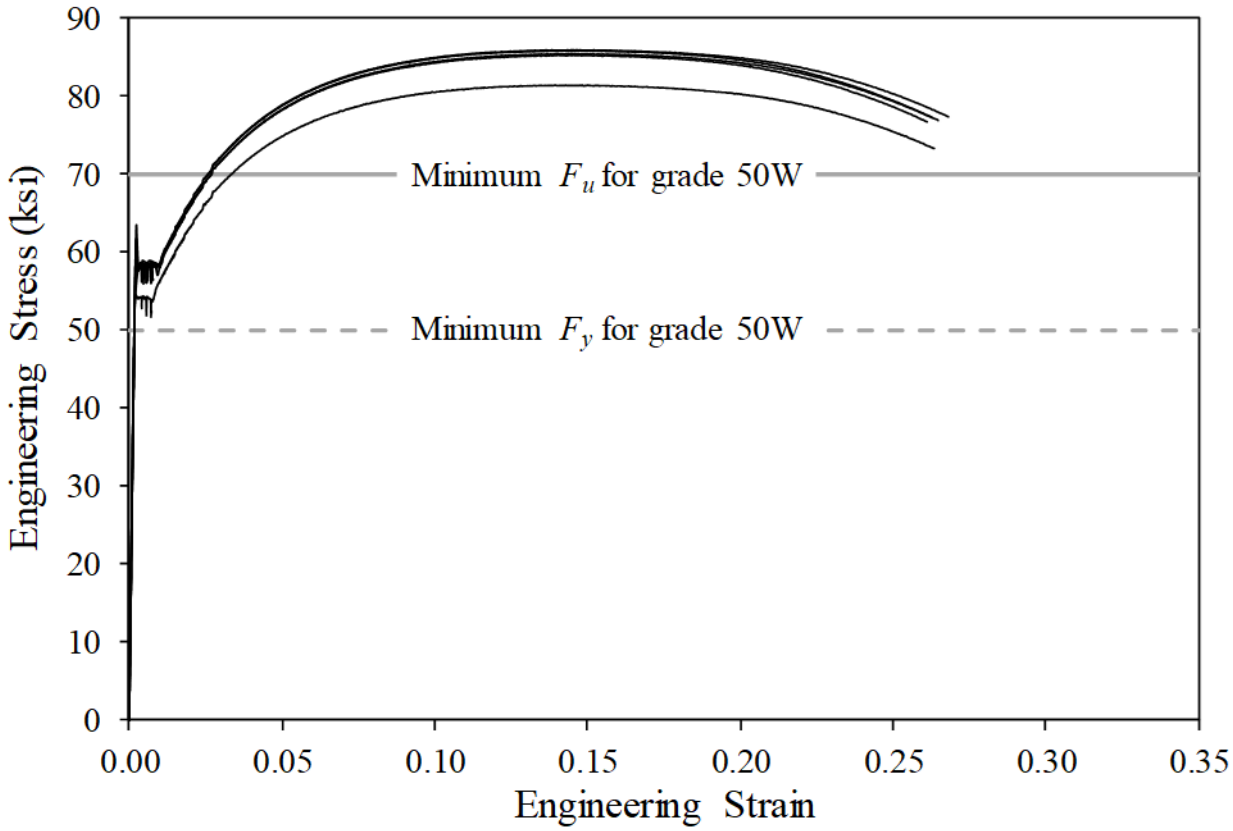

Source: FHWA.

Figure 72. Graph. Engineering stress versus strain for series E3-50W.

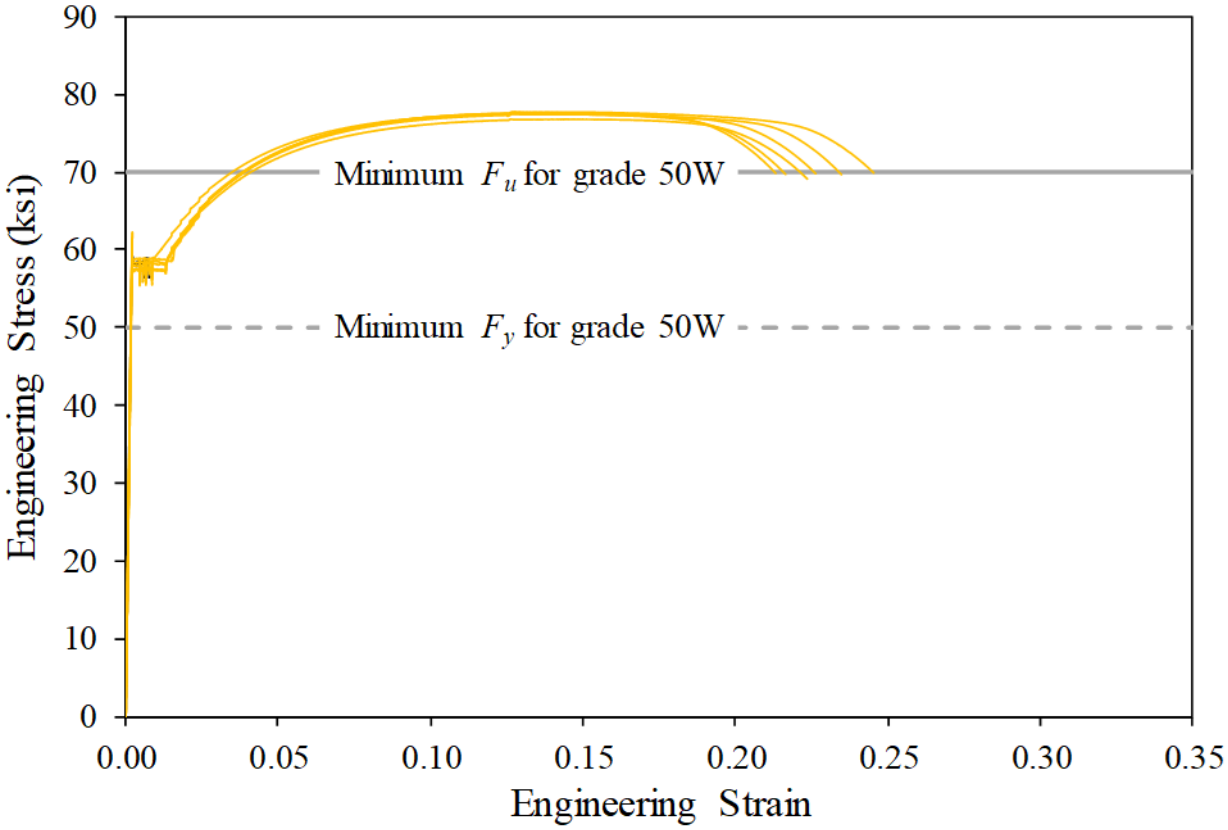

Source: FHWA.

Figure 73. Graph. Engineering stress versus strain for series E4-50W.

Table 38. Tensile specimen test results.

Series	Test Number	F_u (ksi)	0.2-Percent Offset Yield, F_y (ksi)	F_y/F_u	Elongation at Fracture (Percent)[a]	Reduction of Area (Percent)
C1-50	1	74.6	51.1	0.68	29.6	63.0
	2	74.3	52.1	0.70	29.1	67.1
	3	74.6	51.6	0.69	29.1	68.2
	4	74.7	51.8	0.69	29.7	65.6
	5	75.0	51.7	0.69	29.5	67.0
	Average	**74.6**	**51.7**	**0.69**	**29.4**	**66.2**
C1-50W	1	83.8	59.6	0.71	25.8	68.2
	2	86.2	60.0	0.70	25.8	66.9
	3	84.3	60.7	0.72	24.7	69.1
	4	86.4	60.0	0.69	25.5	69.7
	5	85.7	58.8	0.69	25.3	68.5
	6	84.5	59.0	0.70	24.9	69.3
	Average	**85.2**	**59.7**	**0.70**	**25.3**	**68.6**
C2-36	1	73.1	46.1	0.63	32.1	57.7
	2	75.1	46.5	0.62	24.9	54.4
	3	71.9	45.6	0.63	32.7	63.1
	4	72.4	45.9	0.63	32.5	67.4
	5	72.7	46.1	0.63	31.8	65.8
	6	74.1	46.0	0.62	25.4	47.6
	Average	**73.2**	**46.0**	**0.63**	**29.9**	**59.3**
C2-50W	1	**77.2**	**56.6**	**0.73**	**21.7**	—
	2	**77.2**	**56.2**	**0.73**	**22.2**	—
	3	**77.5**	**56.6**	**0.73**	**21.4**	—
	4	**78.1**	**55.9**	**0.72**	**22.2**	—
	5	**73.1**	**53.1**	**0.73**	**21.0**	—
	Average	**76.6**	**55.7**	**0.73**	**21.7**	—
E3-50W	1	86.0	58.7	0.68	26.8	69.2
	2	85.5	58.5	0.68	26.5	70.6
	3	85.3	58.5	0.69	26.1	72.3
	4	81.5	54.1	0.66	26.4	70.8
	5	85.9	58.8	0.68	26.3	69.6

Series	Test Number	F_u (ksi)	0.2-Percent Offset Yield, F_y (ksi)	F_y/F_u	Elongation at Fracture (Percent)[a]	Reduction of Area (Percent)
	Average	**84.8**	**57.7**	**0.68**	**26.4**	**70.5**
E4-50W	1	76.8	57.5	0.75	22.3	56.2
	2	77.8	58.8	0.76	24.5	50.8
	3	77.7	57.5	0.74	21.3	58.9
	4	77.5	58.3	0.75	22.6	61.9
	5	77.6	57.5	0.74	21.6	54.4
	6	77.4	57.9	0.75	23.5	53.6
	Average	**77.5**	**57.9**	**0.75**	**22.6**	**56.0**

[a]Specimens for series C1-50, C1-50W, C2-36, and E3-50W were sheet-type with a 2-inch gauge length. Specimens for series C2-50W and E4-50W were plate-type with an 8-inch gauge length.
—Measurements not taken, no data to report.

CVN DATA AND TRANSITION CURVES

The testing temperature specified for each group of specimens listed in table 11 corresponds to the temperature at which the base material displayed a CVN impact energy of 25 ft-lbf. This is the minimum impact energy permitted in fracture-critical bridge members and is specified to ensure a material displays adequate impact energy at the lowest possible anticipated service temperature. Knowing the fracture behavior of the tension specimens tested at temperatures corresponding to specified minimum impact energy can help determine whether plasma-cut holes should be permitted in fracture-critical bridge members. The tension members should have adequate tensile strength and display significant inelastic deformation at the prescribed testing temperature.

To determine the required testing temperature for tension tests, a CVN transition curve was constructed for each steel grade from each fabricator. Tests were conducted in accordance with ASTM E23 standards using Type-A notched bar specimens.[(18)] For fabricators E3 and E4, the CVN specimens were fabricated from blank steel plates requested during procurement of the fatigue and tension members. For fabricators C1 and C2, CVN specimens were machined from the gross section of discarded fatigue test specimens. Series C1 and C2 CVN specimens were tested over a temperature range from −80 to 40 °F. Series E3 and E4 CVN specimens were tested over a temperature range from −80 to 100 °F. Both temperature ranges were sufficient for characterizing the lower portions of the CVN transition, including the lower shelf.

After impact testing, a line was fitted by least-square regression to the data for each specimen series. The regression line is based on a double-hyperbolic tangent function that produces an inverted S-curve meant to characterize CVN data with lower and upper shelves and a transition region. The temperature at an impact energy of 25 ft-lbf was then determined from the regression line. The raw CVN data for all the steel types are tabulated in table 39 through table 43. Plots of the data, along with the fitted curve, are shown in figure 74 through figure 78.

Table 39. CVN impact data for series C1-50W.

Specimen ID	Temperature (°F)	CVN Impact Energy (ft-lbf)
5	−80	7.3
16	−80	8.4
12	−80	6.5
15	−60	3.8
4	−60	6.8
11	−60	6.8
14	−40	9.0
22	−40	15.5
17	−40	10.0
10	−20	19.5
21	−20	21.0
8	−20	28.5
2	0	21.5
3	0	27.8
9	0	20.5
1	20	45.0
13	20	38.0
20	20	39.5
6	40	71.0
7	40	63.3
19	40	58.0

Table 40. CVN impact data for series C1-50.

Specimen ID	Temperature (°F)	CVN Impact Energy (ft-lbf)
20	−80	3.8
16	−80	7.8
21	−80	7.3
9	−60	6.0
15	−60	7.3
17	−60	10.8
4	−40	8.5
6	−40	20.0
19	−40	34.3
2	−20	16.3
3	−20	25.3
22	−20	20.0
5	0	54.3
12	0	61.8
11	0	26.0
10	20	76.5
14	20	43.5
13	20	69.3
1	40	84.8
8	40	79.5
7	40	95.5

Table 41. CVN impact data for series C2-36.

Specimen ID	Temperature (°F)	CVN Impact Energy (ft-lbf)
20	−80	2.0
21	−80	2.8
22	−80	2.0
11	−60	3.0
14	−60	2.5
4	−60	3.8
15	−40	6.0
17	−40	5.0
18	−40	3.3
5	−20	8.8
9	−20	8.3
10	−20	10.8
6	0	16.3
1	0	12.8
19	0	15.5
8	20	72.5
2	20	26.8
3	20	37.3
12	40	106.3
13	40	91.5
16	40	218.5

Table 42. CVN impact data for series E3-50W.

Specimen ID	Temperature (°F)	CVN Impact Energy (ft-lbf)
30	−80	8.0
29	−80	8.3
28	−80	6.8
27	−60	7.3
26	−60	7.0
25	−60	6.3
24	−40	8.3
23	−40	9.8
22	−40	8.3
21	−20	14.5
20	−20	36.0
19	−20	14.0
18	0	15.0
17	0	22.5
16	0	33.0
15	20	31.5
14	20	64.5
13	20	39.5
12	40	97.5
11	40	51.5
10	40	130.0
9	60	98.0
8	60	152.0
7	60	82.0
6	80	108.0
5	80	158.0
4	80	119.0
3	100	132.0
2	100	144.0
1	100	151.0

Table 43. CVN impact data for series E4-50W.

Specimen ID	Temperature (°F)	CVN Impact Energy (ft-lbf)
28	−80	3.0
29	−80	3.3
30	−80	5.0
25	−60	4.3
26	−60	3.5
27	−60	4.5
22	−40	12.3
23	−40	7.5
24	−40	4.5
19	−20	10.8
20	−20	10.3
21	−20	15.5
16	0	27.0
17	0	28.0
18	0	49.8
13	20	38.0
14	20	35.0
15	20	50.8
10	40	53.8
11	40	70.0
12	40	76.8
7	60	65.3
8	60	88.3
9	60	74.5
4	80	98.3
5	80	89.8
6	80	98.0
1	100	89.5
2	100	101.5
3	100	113.8

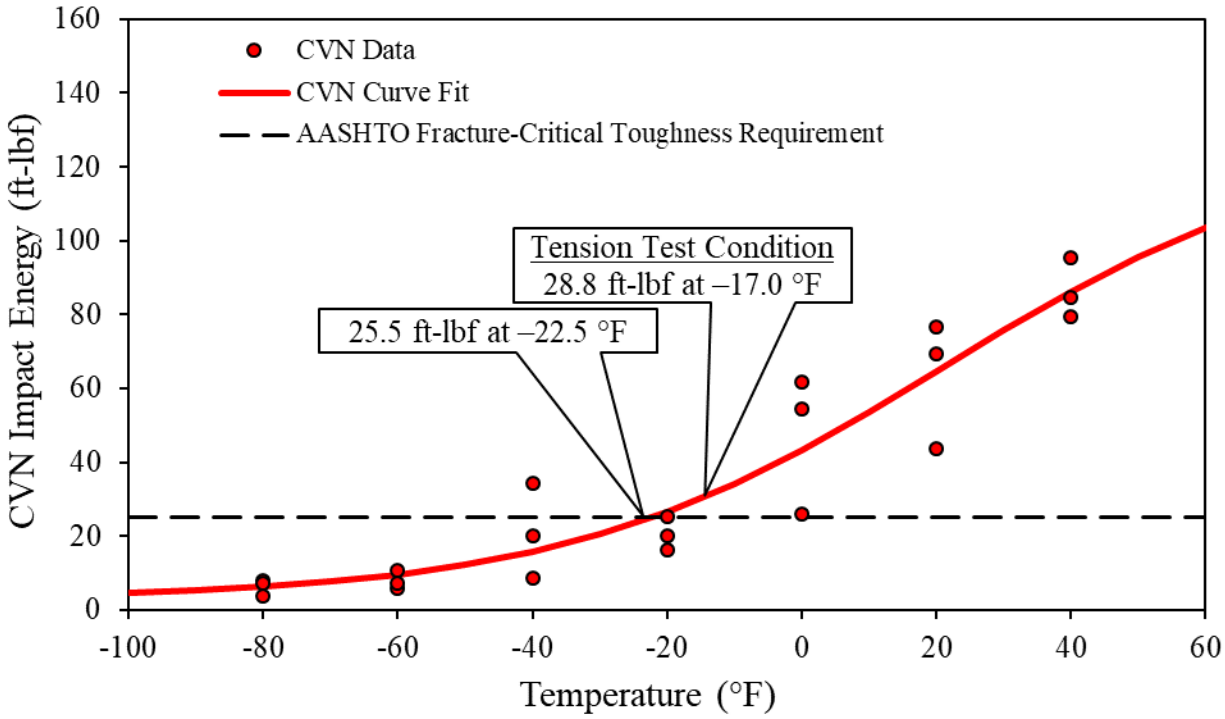

Source: FHWA.

Figure 74. Graph. CVN transition curve for series C1-50.

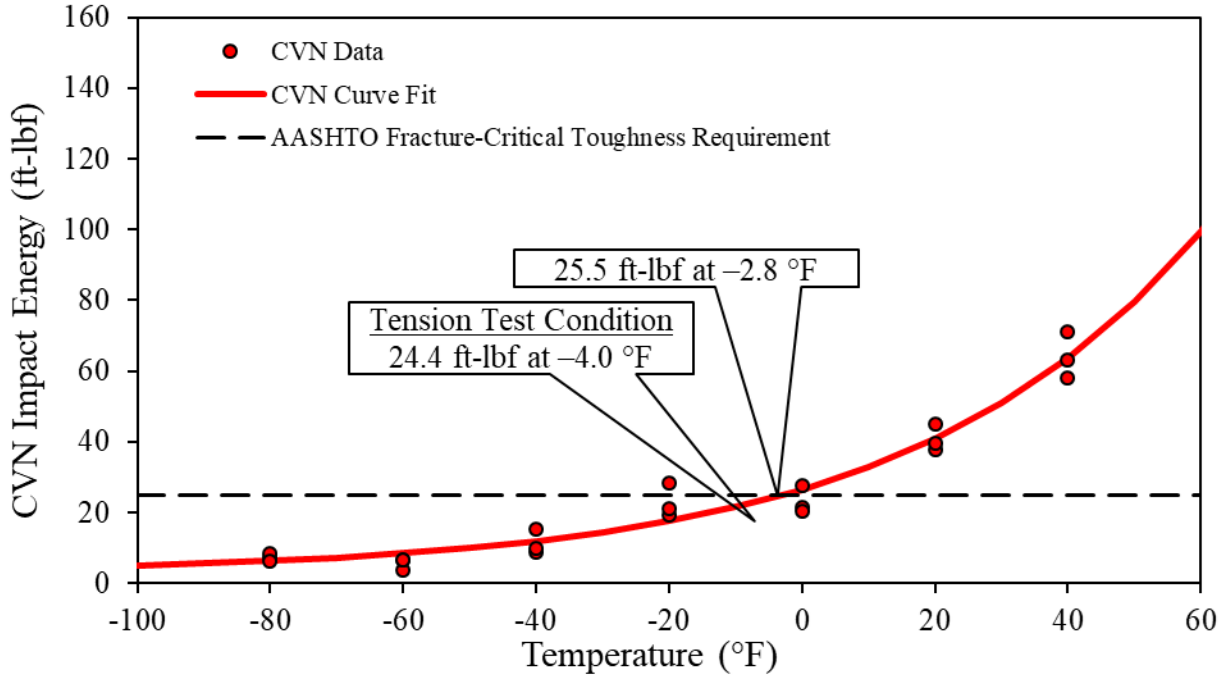

Source: FHWA.

Figure 75. Graph. CVN transition curve for series C1-50W.

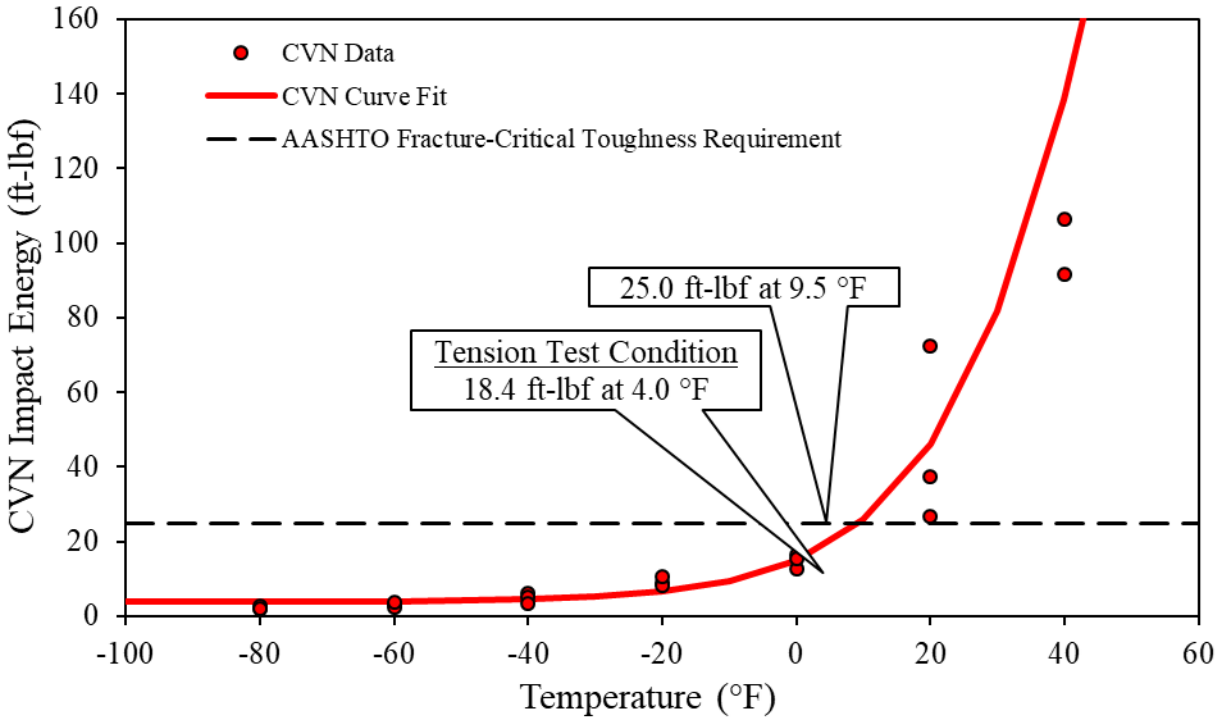

Source: FHWA.

Figure 76. Graph. CVN transition curve for series C2-36.

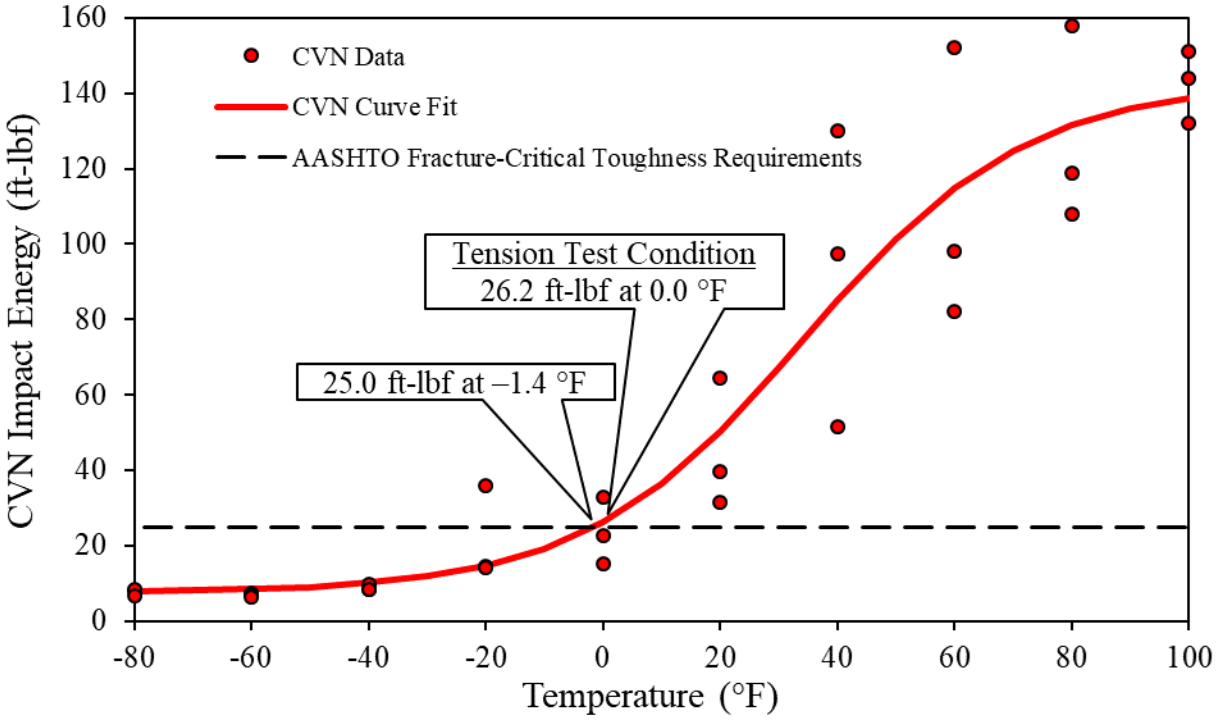

Source: FHWA.

Figure 77. Graph. CVN transition curve for series E3-50W.

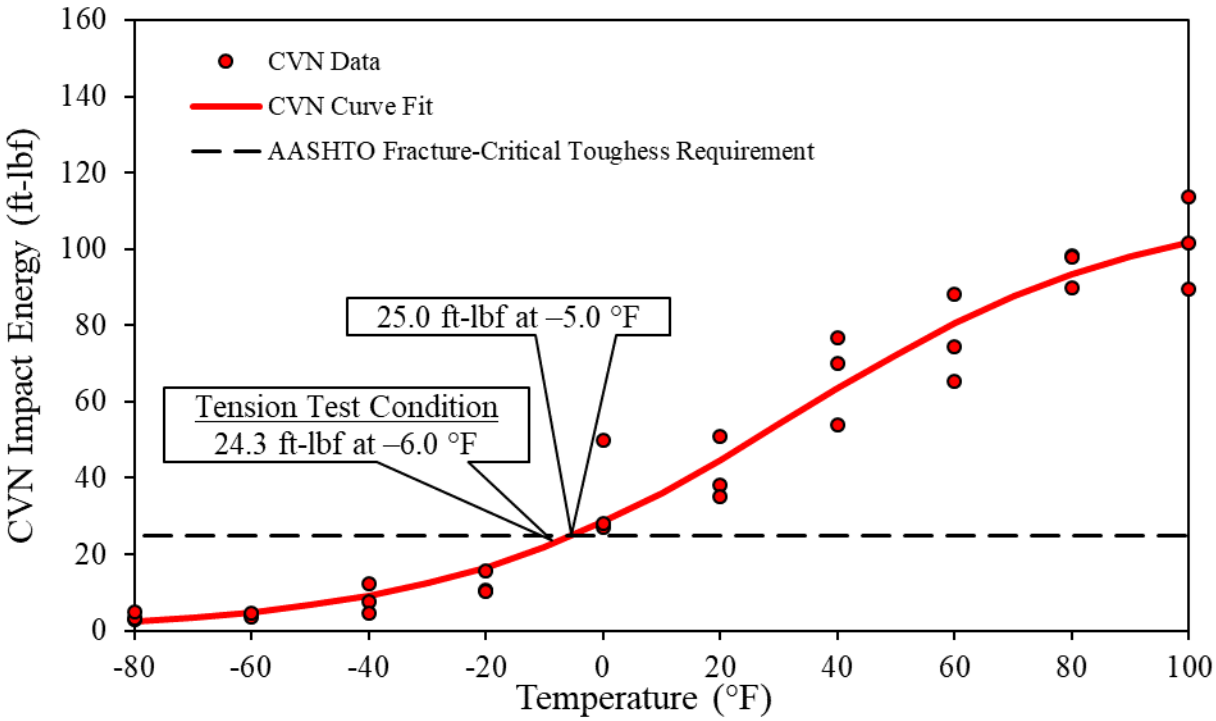

Source: FHWA.

Figure 78. Graph. CVN transition curve for series E4-50W.

APPENDIX D. POST-TEST PICTURES OF TENSILE SPECIMENS

Figure 79 through figure 93 show each of the tensile specimens from series C1-50. Figure 94 through figure 107 show each of the tensile specimens from series C1-50W. Figure 108 through figure 122 show each of the tensile specimens from series C2-36. Figure 123 through figure 146 show each of the tensile specimens from series E3-50W. Figure 147 through figure 170 show each of the tensile specimens from series E4-50W. Figure 171 through figure 186 show each of the tensile specimens from specimens with drilled holes.

SERIES C1-50

Source: FHWA.

Figure 79. Photo. C1-50-1.

Source: FHWA.

Figure 81. Photo. C1-50-5.

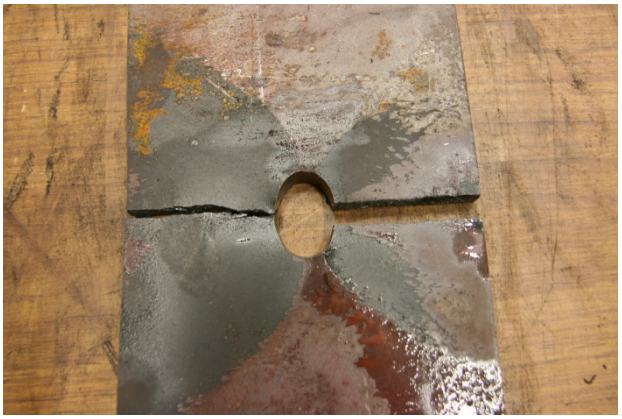

Source: FHWA.

Figure 80. Photo. C1-50-3.

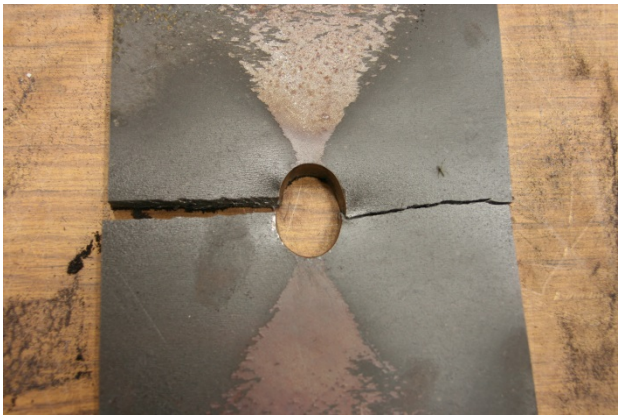

Source: FHWA.

Figure 82. Photo. C1-50-7.

Source: FHWA.

Figure 83. Photo. C1-50-9.

Source: FHWA.

Figure 86. Photo. C1-50-4.

Source: FHWA.

Figure 84. Photo. C1-50-11.

Source: FHWA.

Figure 87. Photo. C1-50-6.

Source: FHWA.

Figure 85. Photo. C1-50-2.

Source: FHWA.

Figure 88. Photo. C1-50-8.

Source: FHWA.

Figure 89. Photo. C1-50-10.

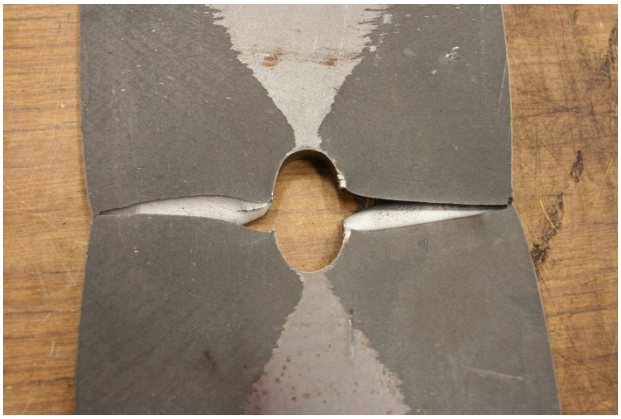

Source: FHWA.

Figure 92. Photo. C1-50-14.

Source: FHWA.

Figure 90. Photo. C1-50-12.

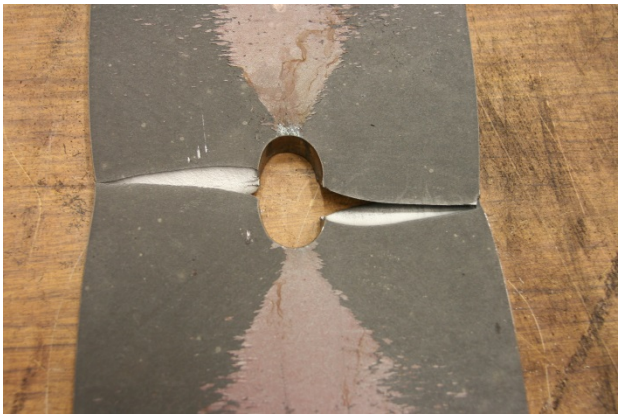

Source: FHWA.

Figure 93. Photo. C1-50-15.

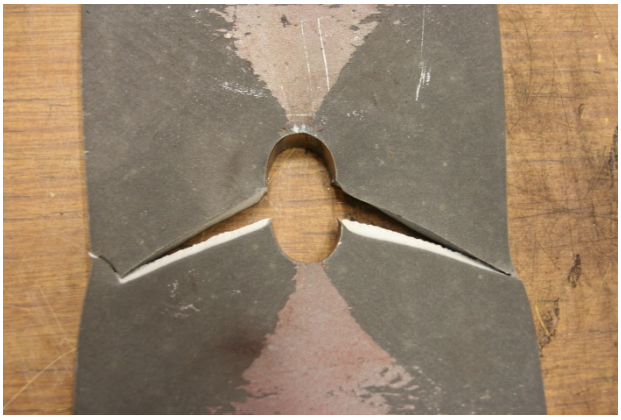

Source: FHWA.

Figure 91. Photo. C1-50-13.

SERIES C1-50W

Source: FHWA.

Figure 94. Photo. C1-50W-1.

Source: FHWA.

Figure 95. Photo. C1-50W-3.

Source: FHWA.

Figure 96. Photo. C1-50W-5.

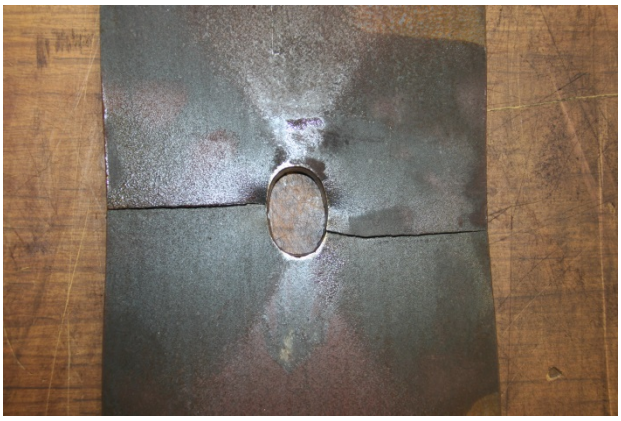

Source: FHWA.

Figure 97. Photo. C1-50W-7.

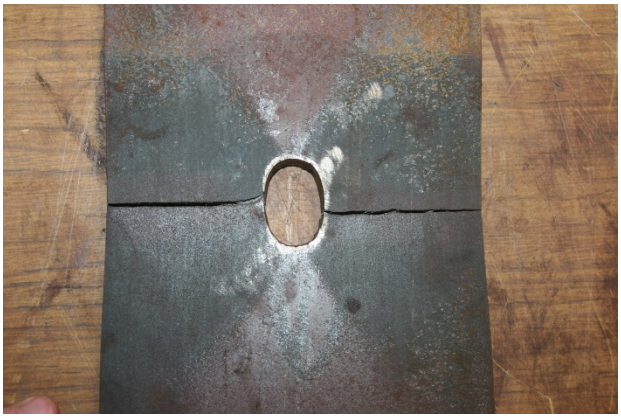

Source: FHWA.

Figure 98. Photo. C1-50W-9.

Source: FHWA.

Figure 99. Photo. C1-50W-11.

Source: FHWA.

Figure 100. Photo. C1-50W-2.

Source: FHWA.

Figure 103. Photo. C1-50W-8.

Source: FHWA.

Figure 101. Photo. C1-50W-4.

Source: FHWA.

Figure 104. Photo. C1-50W-10.

Source: FHWA.

Figure 102. Photo. C1-50W-6.

Source: FHWA.

Figure 105. Photo. C1-50W-12.

Source: FHWA.

Figure 106. Photo. C1-50W-14.

Source: FHWA.

Figure 107. Photo. C1-50W-15.

SERIES C2-36

Source: FHWA.

Figure 108. Photo. C2-36-1.

Source: FHWA.

Figure 109. Photo. C2-36-2.

Source: FHWA.

Figure 110. Photo. C2-36-3.

Source: FHWA.

Figure 111. Photo. C2-36-4.

Source: FHWA.

Figure 112. Photo. C2-36-5.

Source: FHWA.

Figure 113. Photo. C2-36-6.

Source: FHWA.

Figure 114. Photo. C2-36-7.

Source: FHWA.

Figure 115. Photo. C2-36-8.

Source: FHWA.

Figure 116. Photo. C2-36-9.

Source: FHWA.

Figure 117. Photo. C2-36-10.

Source: FHWA.

Figure 118. Photo. C2-36-11.

Source: FHWA.

Figure 121. Photo. C2-36-14.

Source: FHWA.

Figure 119. Photo. C2-36-12.

Source: FHWA.

Figure 122. Photo. C2-36-15.

Source: FHWA.

Figure 120. Photo. C2-36-13.

SERIES E3-50W

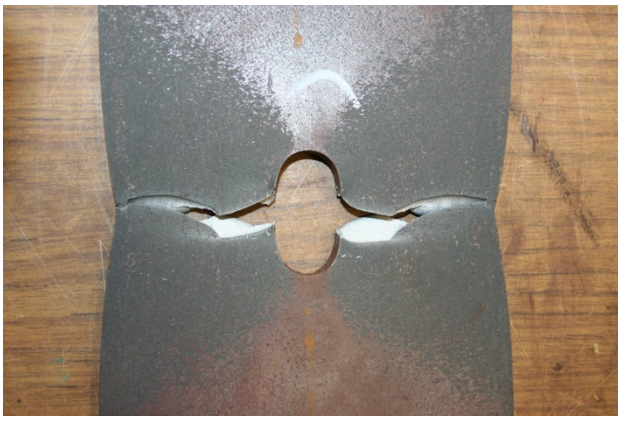

Source: FHWA.

Figure 123. Photo. E3-0-1.

Source: FHWA.

Figure 124. Photo. E3-0-2.

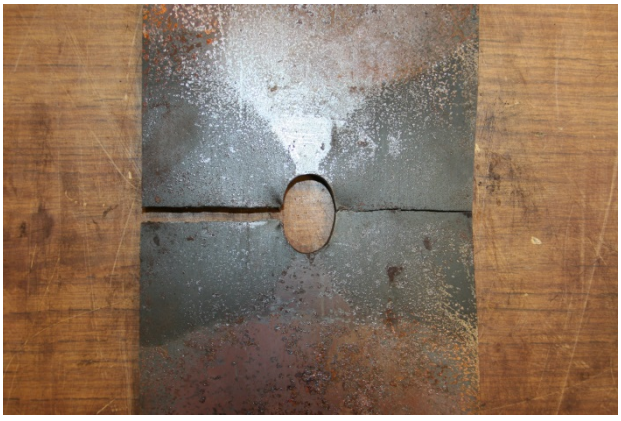

Source: FHWA.

Figure 125. Photo. E3-0-3.

Source: FHWA.

Figure 126. Photo. E3-0-4.

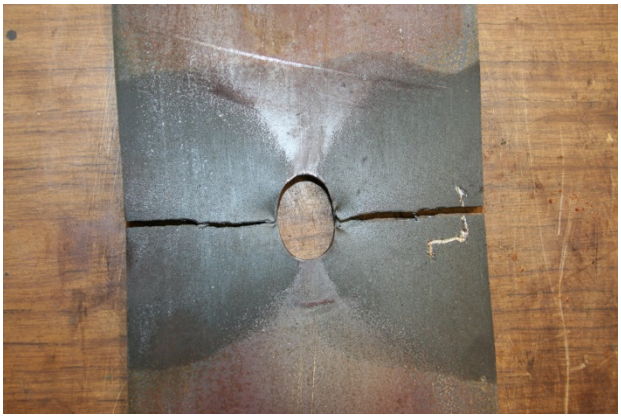

Source: FHWA.

Figure 127. Photo. E3-0-5.

Source: FHWA.

Figure 128. Photo. E3-0-6.

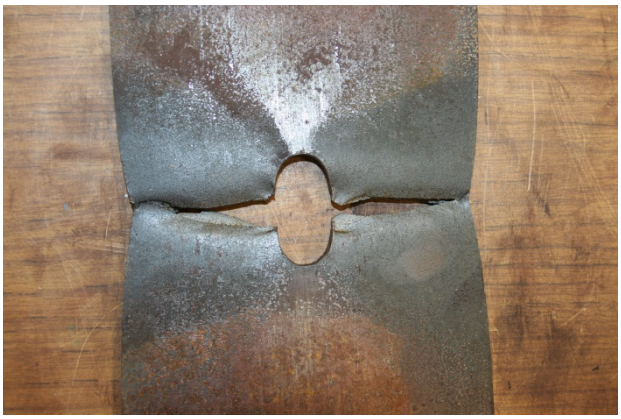

Source: FHWA.

Figure 129. Photo. E3-0-7.

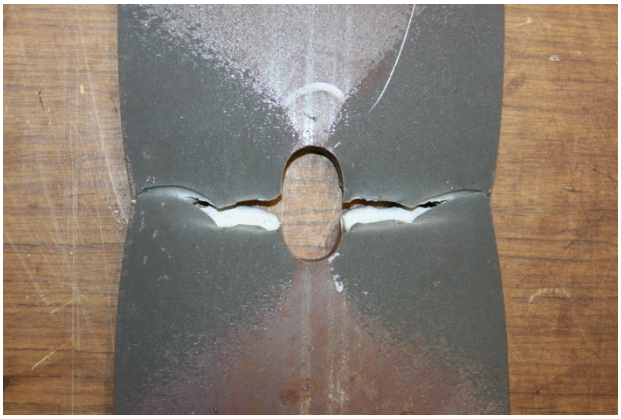

Source: FHWA.

Figure 132. Photo. E3-45-2.

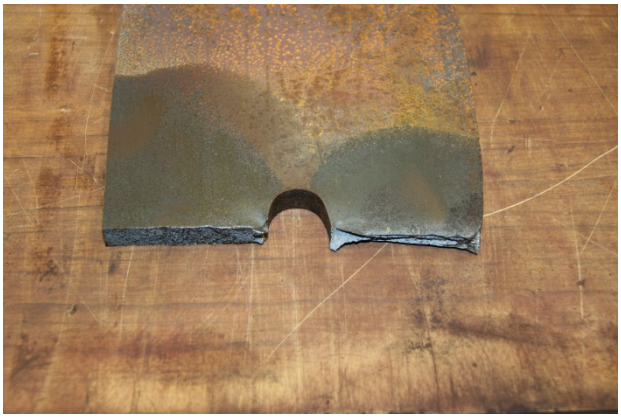

Source: FHWA.

Figure 130. Photo. E3-0-8.

Source: FHWA.

Figure 133. Photo. E3-45-3.

Source: FHWA.

Figure 131. Photo. E3-45-1.

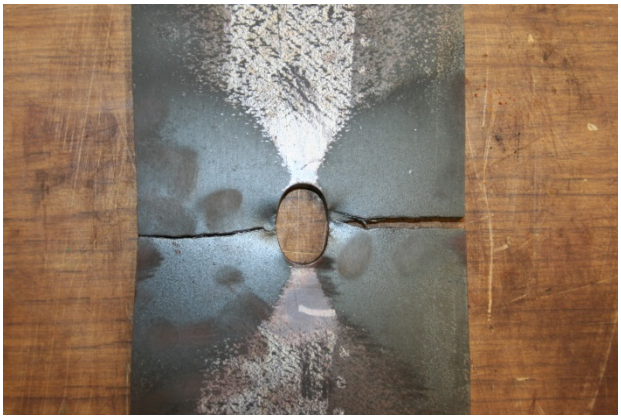

Source: FHWA.

Figure 134. Photo. E3-45-4.

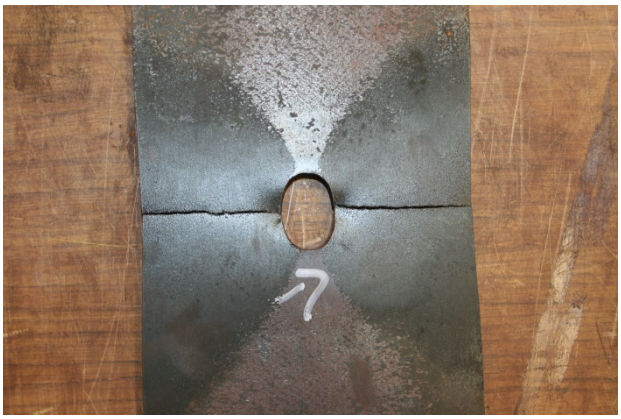

Source: FHWA.

Figure 135. Photo. E3-45-5.

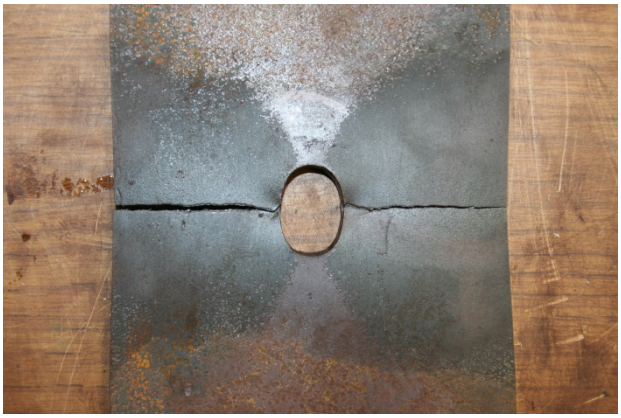

Source: FHWA.

Figure 136. Photo. E3-45-6.

Source: FHWA.

Figure 137. Photo. E3-45-7.

Source: FHWA.

Figure 138. Photo. E3-45-8.

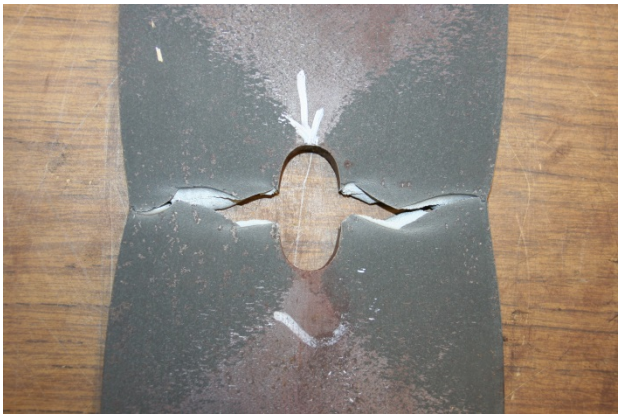

Source: FHWA.

Figure 139. Photo. E3-90-1.

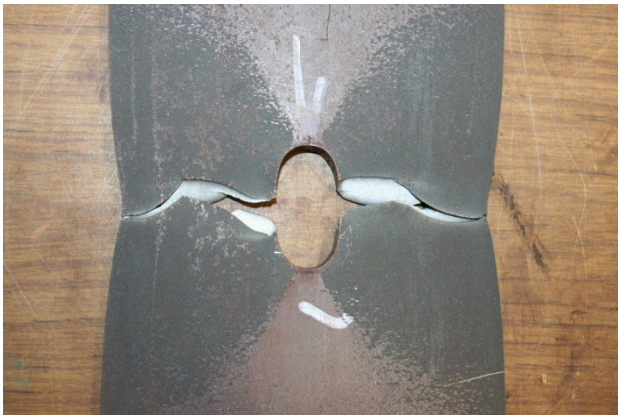

Source: FHWA.

Figure 140. Photo. E3-90-2.

Source: FHWA.

Figure 141. Photo. E3-90-3.

Source: FHWA.

Figure 144. Photo. E3-90-6.

Source: FHWA.

Figure 142. Photo. E3-90-4.

Source: FHWA.

Figure 145. Photo. E3-90-7.

Source: FHWA.

Figure 143. Photo. E3-90-5.

Source: FHWA.

Figure 146. Photo. E3-90-8.

SERIES E4-50W

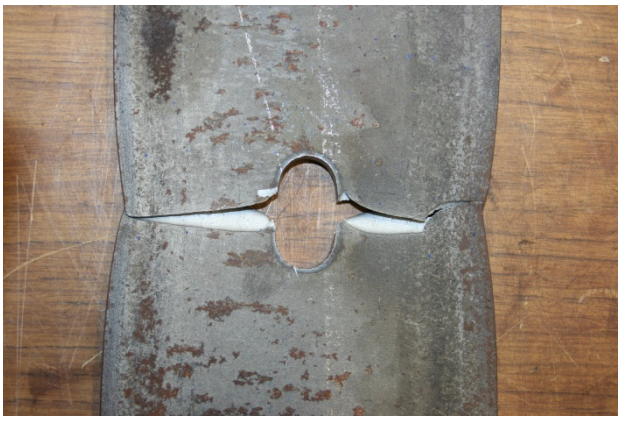

Source: FHWA.

Figure 147. Photo. E4-0-1.

Source: FHWA.

Figure 148. Photo. E4-0-2.

Source: FHWA.

Figure 149. Photo. E4-0-3.

Source: FHWA.

Figure 150. Photo. E4-0-4.

Source: FHWA.

Figure 151. Photo. E4-0-5.

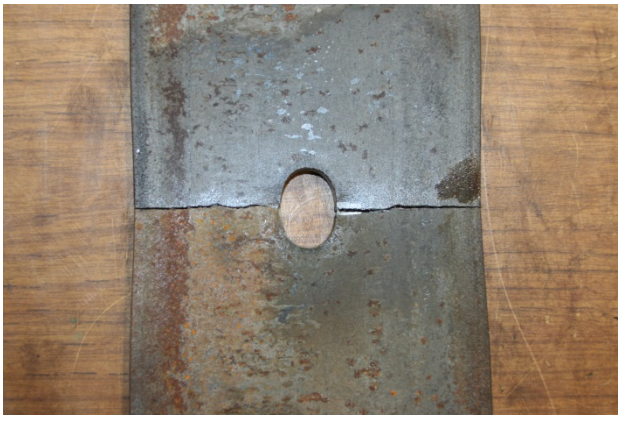

Source: FHWA.

Figure 152. Photo. E4-0-6.

Source: FHWA.

Figure 153. Photo. E4-0-7.

Source: FHWA.

Figure 156. Photo. E4-45-2.

Source: FHWA.

Figure 154. Photo. E4-0-8.

Source: FHWA.

Figure 157. Photo. E4-45-3.

Source: FHWA.

Figure 155. Photo. E4-45-1.

Source: FHWA.

Figure 158. Photo. E4-45-4.

Source: FHWA.

Figure 159. Photo. E4-45-5.

Source: FHWA.

Figure 162. Photo. E4-45-8.

Source: FHWA.

Figure 160. Photo. E4-45-6.

Source: FHWA.

Figure 163. Photo. E4-90-1.

Source: FHWA.

Figure 161. Photo. E4-45-7.

Source: FHWA.

Figure 164. Photo. E4-90-2.

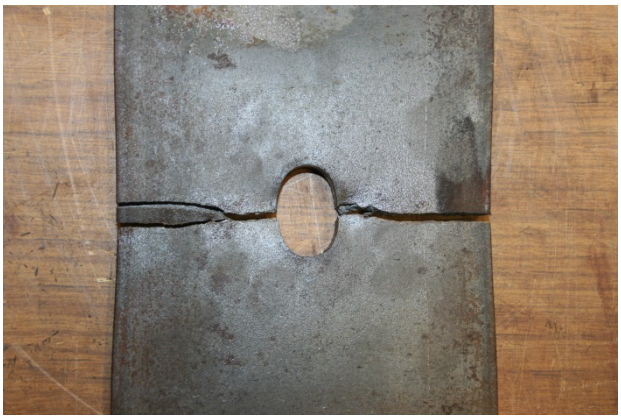

Source: FHWA.

Figure 165. Photo. E4-90-3.

Source: FHWA.

Figure 168. Photo. E4-90-6.

Source: FHWA.

Figure 166. Photo. E4-90-4.

Source: FHWA.

Figure 169. Photo. E4-90-7.

Source: FHWA.

Figure 167. Photo. E4-90-5.

Source: FHWA.

Figure 170. Photo. E4-90-8.

DRILLED SPECIMENS

Source: FHWA.

Figure 171. Photo. E3-d1.

Source: FHWA.

Figure 172. Photo. E3-d2.

Source: FHWA.

Figure 173. Photo. E3-d3.

Source: FHWA.

Figure 174. Photo. E4-d1.

Source: FHWA.

Figure 175. Photo. E4-d2.

Source: FHWA.

Figure 176. Photo. E4-d3.

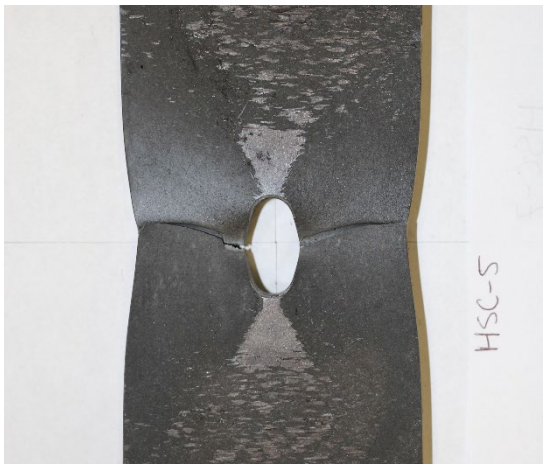

Source: FHWA.

Figure 177. Photo. C1-50-5c.

Source: FHWA.

Figure 180. Photo. C1-50-20c.

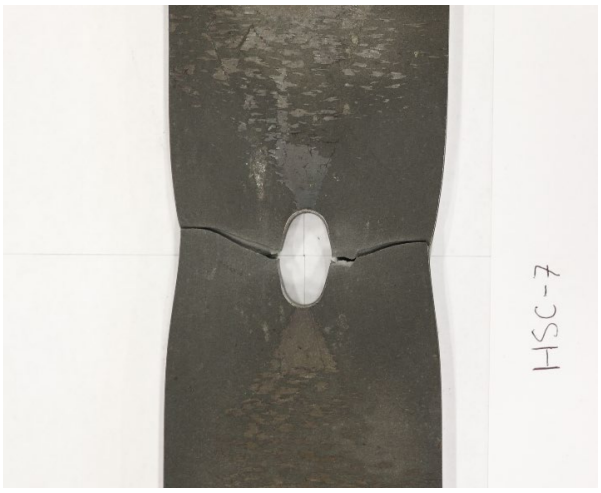

Source: FHWA.

Figure 178. Photo. C1-50-7c.

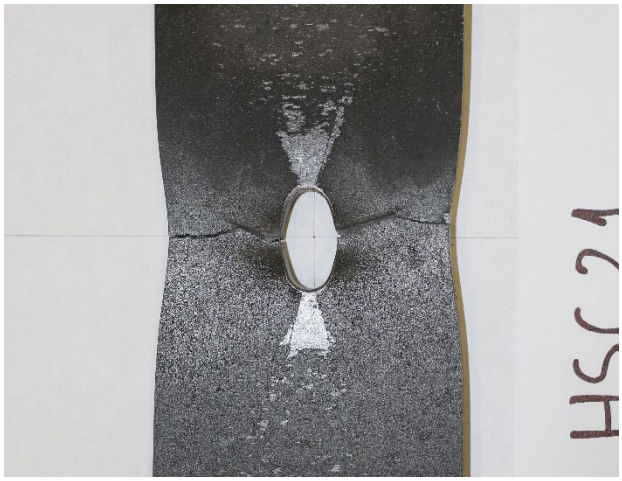

Source: FHWA.

Figure 181. Photo. C1-50-21c.

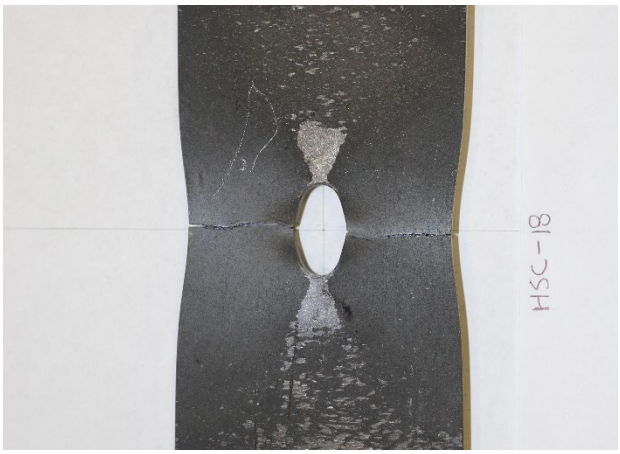

Source: FHWA.

Figure 179. Photo. C1-50-18c.

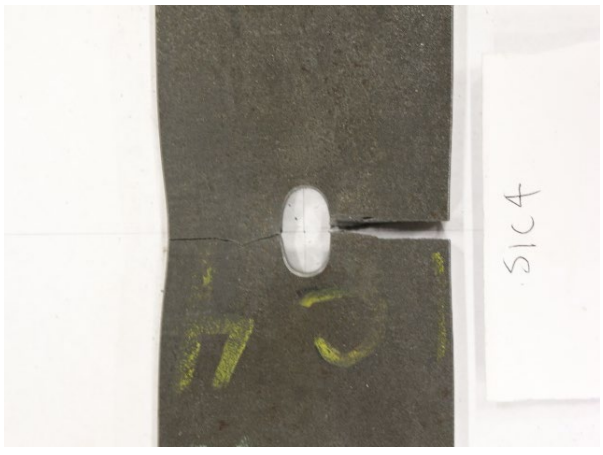

Source: FHWA.

Figure 182. Photo. C2-36-04c.

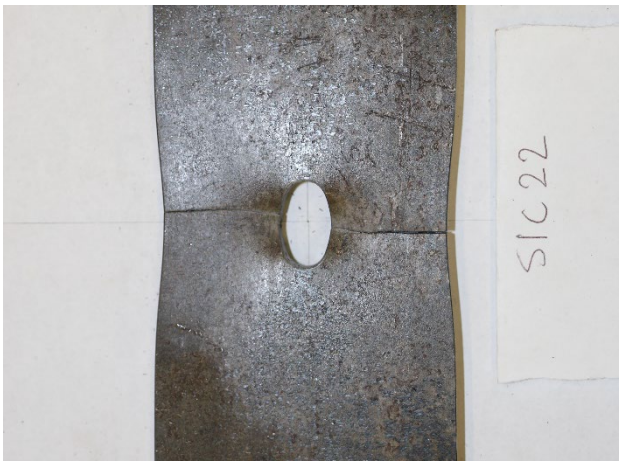

Source: FHWA.

Figure 183. Photo. C2-36-22c.

Source: FHWA.

Figure 184. Photo. C2-36-23c.

Source: FHWA.

Figure 185. Photo. C2-36-27c.

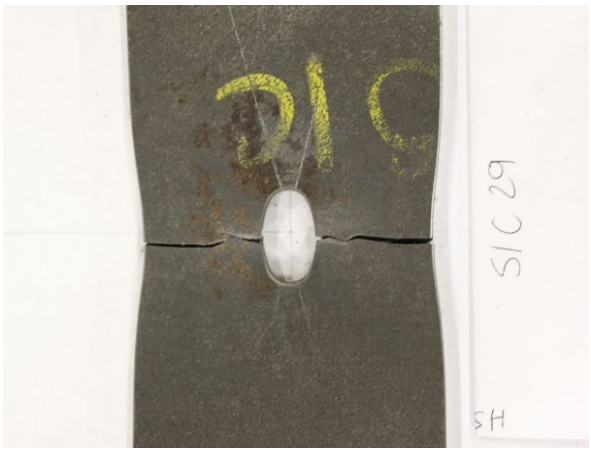

Source: FHWA.

Figure 186. Photo. C2-36-29c.

REFERENCES

1. AASHTO. (2010). *AASHTO LRFD Bridge Construction Specifications*, 3rd Edition, American Association of State Highway and Transportation Officials, Washington, DC.

2. AASHTO. (2012). *AASHTO LRFD Bridge Design Specifications,* 6th Edition, American Association of State Highway and Transportation Officials, Washington, DC.

3. Kulak, G.L., Fisher, J.W., and Struik, J.A. (2001). *Guide to Design Criteria for Bolted and Riveted Joints*, American Institute of Steel Construction, Chicago, IL.

4. Wu, Y., Hackett, C.M., and Eickhoff, S.T. (1997). "The Effects of Plasma Arc Cutting on Mild Steel." *FabTech International Technical Conference*, *2*, pp. 1103–1122, Society of Manufacturing Engineers, Dearborn, MI.

5. Colt, J. (2014). "The High-Definition Revolution in Plasma Cutting." *FAB Shop Magazine Direct*. Techgen Media, Plainsboro, NJ. Available online: https://fsmdirect.com/cutting/plasma-cutting/74-the-high-definition-revolution-in-plasma-cutting. Last accessed October, 10, 2016.

6. Colt, J. (2011). "Mechanized Plasma Cutting: Developments in High-Definition Technology Improve Versatility," *Practical Welding Today*, Available online: https://www.thefabricator.com/article/cuttingweldprep/mechanized-plasma-cutting-developments-in-high-definition-technology-improve-versatility. Last accessed October, 10, 2016.

7. Kirkpatrick, I. (1998). "High Definition Plasma – An Alternative to Laser Technology." *Aircraft Engineering and Aerospace Technology*, *70*(3), pp. 215–217. Emerald Publishing, Inc., Somerville, MA.

8. Brown, J.D., Lubitz, D.J., Cekov, Y.C., Frank, K.H., and Keating, P.B. (2007). *Evaluation of Influence of Hole Making Upon the Performance of Structural Steel Plates and Connections*, Report No. FHWA/TX-07/0-4624-1, Texas Department of Transportation, Austin, TX

9. ASTM. (2009). "ASTM A709/A709M, Standard Specification for Structural Steel for Bridges." *Book of Standards Volume 01.04*, ASTM International, West Conshohocken, PA.

10. Salonitis, K. and Vatousianos, S. (2012). "Experimental Investigation of the Plasma Arc Cutting Process." *Procedia CIRP, 45th CIRP Conference on Manufacturing Systems*, *3*, pp. 287–292, Athens, Greece. Available online: https://doi.org/10.1016/j.procir.2012.07.050. Last accessed October, 10, 2016.

11. Thomas, D.J. (2011). "Optimizing Plasma Cut-Edge Properties for Improving the Durability of Bridge Structures." *International Journal of Steel Structures*, *11*(4), pp. 481–493. Korean Society of Steel Construction, Seoul, South Korea.

12. ASTM. (2006). “ASTM E340, Standard Test Method for Macroetching Metals and Alloys.” *Book of Standards Volume 03.01*, ASTM International, West Conshohocken, PA.

13. ASTM. (2016). “ASTM E384, Standard Test Method for Microindentation Hardness of Materials.” *Book of Standards Volume 03.01*, ASTM International, West Conshohocken, PA.

14. ASTM. (2014). “ASTM A325, Standard Specification for Structural Bolts, Steel, Heat Treated, 120/105 ksi Minimum Tensile Strength.” (Withdrawn 2016). ASTM International, West Conshohocken, PA.

15. NIST. (2013). *NIST/SEMATECH e-Handbook of Statistical Methods*, National Institute of Standards and Technology, Gaithersburg, MD. Available online: http://www.itl.nist.gov/div898/handbook. Last accessed June 1, 2016.

16. Barsom, J.M. (1975). “Development of the AASHTO Fracture-Toughness Requirements for Bridge Steels.” *Engineering Fracture Mechanics*, *7*(3), pp. 605–18. Available online: https://doi.org/10.1016/0013-7944(75)90060-0.

17. ASTM. (2013). “ASTM E8/E8M, Standard Test Methods for Tension Testing of Metallic Materials.” *Book of Standards Volume 03.01*, ASTM International, West Conshohocken, PA.

18. ASTM. (2012). “ASTM E23, Standard Test Methods for Notched Bar Impact Testing of Metallic Materials.” *Book of Standards Volume 03.01*, ASTM International, West Conshohocken, PA.

Recycled
Recyclable

HRDI-40/08-20(WEB)E